Connecting sediment dynamics to coastal morphology over linked spatial and temporal scales in Myanmar and New Zealand

Hannah E. Glover

A dissertation

submitted in partial fulfillment of the

requirements for the degree of

Doctor of Philosophy

University of Washington

2022

Reading Committee:

Andrea S. Ogston, Chair

Charles A. Nittrouer

John Wesley Lauer

Program Authorized to Offer Degree:

Oceanography

University of Washington

Abstract

Connecting sediment dynamics to coastal morphology

over linked spatial and temporal scales in Myanmar and New Zealand

Hannah E. Glover

Chair of the Supervisory Committee:
Professor Andrea S. Ogston
Oceanography

Low-lying coastal environments are threatened by sea-level rise (SLR), which is often locally exacerbated by anthropogenic alterations that accelerate subsidence. Managing and protecting these valuable regions requires understanding the fundamental sedimentary processes that build coastal landforms. This thesis presents four process-based studies of the transport and fate of sediment at the river-ocean interface. The goal of this work is to 1) connect natural sediment dynamics to resulting morphology over linked spatial and temporal scales and 2) evaluate the impact of mangrove removal on these coastal processes. Three of the studies are focused on the Ayeyarwady Delta, Myanmar while the fourth examines an embayment in New Zealand.

The Ayeyarwady River currently delivers the third largest sediment load to the coastal ocean, and the tide-dominated Ayeyarwady Delta is less altered than similar megadeltas, providing

a rich opportunity to connect natural processes to morphology. The first study compares sediment dynamics and retention in the tidal-to-estuarine reach of three representative distributaries of the delta. The velocity, suspended-sediment concentrations (SSC), and bed texture were evaluated in the eastern Yangon, central Bogale, and western Pathein distributaries during the high-flow (September 2017) and low-flow (March 2018 and 2019) seasons. During high flow, the lower distributaries were freshwater tidal rivers with comparable SSCs. During low flow, there was little net discharge, however, the SSC increased to >1 g/L in the Yangon, remained constant in the Bogale, and decreased in the Pathein distributary compared to high-flow conditions. This shift in conditions was driven by offshore sediment supply; distributary SSC was strongly influenced by deposits of unconsolidated mud near the mouth of the Yangon distributary. Overall, this study demonstrates that processes observed in one distributary may not represent the entire system and that the seasonal timing of discharge will impact nearshore sediment recycling.

The second study examines sediment dynamics and morphology in Meinmahla Island, a mangrove preserve in the Bogale distributary. This type of vegetated mid-channel island plays an important though poorly understood role in modulating fluxes of sediment, carbon, and nutrients through the tidally influenced regions of deltas. Water velocity, salinity, and SSC were measured in low-connectivity (dead-end) and high-connectivity (flow-through) channels, and morphologic evolution was evaluated using sediment cores, aerial imagery, and channel-network surveys. Ebb-dominant, low-connectivity channels along the island exterior did not import enough sediment to maintain the observed ~0.8 cm/y accretion rates. Most of the sediment delivery occurred via interior channels, where water had a long residence time. An interior, high-connectivity channel has shoaled in response to a drainage-network change while the island has aggraded and prograded.

This work demonstrates that mid-channel islands are active filters for sediment and dissolved constituents at the river-ocean interface.

The third study compares sedimentary processes in the relatively undisturbed Meinmahla Island to an adjacent, un-leveed agricultural field. The Ayeyarwady Delta has been deforested for agriculture but has relatively few embanked fields, providing an opportunity to isolate the impact of land-cover change on resilience to subsidence. Sediment dynamics, accumulation rate, and elevation were compared in the field and forest. There were equivalent sediment import rates and land-surface elevations at both sites, indicating that the field is aggrading and keeping pace with SLR. This comparison highlights the relative resilience of un-leveed fields to subsidence. The future stability of the Ayeyarwady Delta depends on the continued absence of dams and levees.

The final study explores the impact of mangrove removal in a quiescent, embayment in New Zealand. In many New Zealand estuaries, expanding mangrove forests are cleared in an effort to flush out fine sediment and restore bivalve habitat. In Waikaraka Estuary, mangroves expanded from the 1940s until a clearing program in 2005. The sediment dynamics and morphology were evaluated in 2019, and a Delft3D numerical model was used to further examine the impact of varying mangrove extent. In 2019, flow in the lower estuary was ebb dominant resulting in net sediment export, while flow in the upper estuary was weakly flood dominant resulting in sediment retention. Due to these persistent hydrodynamic patterns, fine sediment is unlikely to be flushed out of the upper estuary despite mangrove removal. The hydrodynamics were not significantly altered by varying the mangrove extents and were instead controlled by abiotic tidal processes. Overall, mangrove removal is an ineffective method for flushing fine sediment out of quiescent, infilled estuaries.

TABLE OF CONTENTS

LIST OF FIGURES

LIST OF TABLES

ACKNOWLEDGEMENTS

I am eternally grateful to my advisor, Andrea, for getting me here. I would have quit long ago without you. I am also so glad to have shared my time with the members of the Sediment Dynamics Lab: Aaron Fricke, Emily Eidam, Robin McLachlan, Evan Lahr, Sarah Vollero, and Anna Boyar. Your friendship, support, and guidance kept me going. We may not be clean, but we do have fun, and I will miss the Bennett Building, our messy home. I also owe a tremendous amount to my fellow graduate students at UW; you make me happy when skies are gray.

I deeply appreciate the support of numerous international collaborators, without whom this work would not have been possible. Thank you to Dr. Day Wa Aung, Ko Kyaw Kyaw Naing, Chit Yan Toe, Thu Thu Min, Wint Wint Tun, many graduate and undergraduate students from Pathein University and from the River and Coastal Engineering program at Myanmar Maritime University. Thank you also to Nay Lin Kyaw, the FREDA House staff, residents of the town of Gwe Gone, and the crews of the Green River Princess, Zay Yar Kyaw, and other vessels for making all of the field work in Myanmar possible. Many thanks to Dean Sandwell, Annette Rodgers, and Rich Bulmer for assistance with field work and sample processing in New Zealand.

This work was funded by the Association for the Sciences of Limnology and Oceanography: Limnology and Oceanography Research Exchange (NSF award #1831075), the University of Washington Quaternary Research Center, and the Office of Naval Research (Grant Number N000141712350).

DEDICATION

This work is dedicated to my mother, who introduced me to the ocean,

and to my sister, who taught me how to swim.

“And the sunlight clasps the earth

And the moonbeams kiss the sea”

- Percy Bysshe Shelley

Chapter 1. INTRODUCTION

At least 10% of the global population lives in coastal areas <10 m above sea level, often on deltas (Neumann et al., 2015). These coastal areas are threatened by sea-level rise, and in many regions, coastal resilience has been further decreased by damming, coastal deforestation, fluid/sediment extraction, and levee construction (Syvitski et al., 2009). Preserving vulnerable coastlines requires understanding both the natural ecogeomorphic processes that build land surfaces and how human alterations impact these complex feedbacks. Interdisciplinary, source-to-sink studies have provided significant insights into coastal ecogeomorphology; however, it is still challenging to collect in-situ data over the full range of relevant temporal and spatial scales. The following four studies of sediment dynamics at the river-ocean interface in Myanmar and New Zealand focus on different spatial and temporal scales in environments with varying degrees of alteration. Taken together, these investigations provide a wholistic picture, connecting meter-scale processes to 100-kilometer-scale morphology and tidal processes to decadal change.

1.1 SEDIMENT DYNAMICS AND MORPHOLOGY IN NATURAL ENVIRONMENTS

The first two studies examine relatively natural sediment dynamics and morphology in the tide-dominated Ayeyarwady Delta, Myanmar. The Ayeyarwady and Thanlwin Rivers are the least studied of the large, Himalaya-sourced rivers, which discharged 5.1 Gt/y of sediment prior to dam construction (Milliman and Farnsworth, 2011). Myanmar was politically isolated until the early 2000s, limiting international scientific collaboration and investigation within the country, while simultaneously limiting infrastructure development. Consequently, the Ayeyarwady and Thanlwin

Rivers have no mainstem dams (Grill et al., 2019) and now carry the third largest sediment load globally (Baronas et al., 2020). Recent work has focused on the fluvial and marine regions of the Ayeyarwady system (Baronas et al., 2020; Furuichi et al., 2009; Gordon, 1885; Kuehl et al., 2019; Liu et al., 2020; Robinson et al., 2007). However there has been little *in-situ* investigation of the fluvial-to-marine transition zone within the Ayeyarwady Delta. This critical region can retain 40–70% of a river's mainstem sediment load, significantly altering fluxes to the coastal ocean (Goodbred and Kuehl, 1998; Milliman et al., 1985; Nittrouer et al., 1995).

Chapter 2 focuses on variability in sediment transport and retention over tidal and seasonal timescales within the distributaries of this 250-km-wide megadelta. The largest deltas on Earth are tide-dominated with multiple distributaries (Nienhuis et al., 2020), which can experience different forcings. Yet, most observational studies of these systems focus on a single distributary. Data was collected from the tidal-to-estuarine reaches of three representative distributaries during the high flow (September 2017) and low flow (March 2018 and 2019) monsoon seasons. The eastern Yangon distributary empties into the sheltered Gulf of Mottoma while the central Bogale and western Pathein distributaries are exposed to seasonal waves (Kuehl et al., 2019). The goal of this *in-situ* investigation is to examine the variability in sediment retention and export within a single delta. The results demonstrate that nearshore sediment residence time in monsoon-dominated systems is controlled by coastal orientation, the timing of discharge with respect to ocean conditions, and tidal amplification.

Chapter 3 evaluates sediment dynamics in the Ayeyarwady Delta over smaller spatial scales and longer timescales by examining the evolution of a mid-channel island. Vegetated mid-channel islands play an important though poorly understood role in the morphology of tide-dominated deltas (Hiatt et al., 2018; Passalacqua et al., 2013). Cross-cutting tidal channels deliver

sediment to interior island surfaces, and channel connectivity plays an important role in controlling morphologic development (McLachlan et al., 2020a). Meinmahla Island is a relatively unaltered, mid-channel, mangrove-forest preserve in the mouth of the Bogale distributary. Field measurements were collected in the island in 2017–2019 with the goal of connecting the dominant sediment transport pathways to evolving morphology. The data demonstrate that mid-channel islands efficiently import sediment via complex and evolving networks of high and low connectivity tidal channels.

1.2 SEDIMENT DYNAMICS AND MORPHOLOGIC EVOLUTION FOLLOWING MANGROVE REMOVAL

The next two studies build on these investigations of relatively natural systems by considering how sites respond to mangrove removal. Mangroves provide numerous ecosystem services, including sediment retention and coastal stabilization (Alongi, 2008; Friess et al., 2019). They can actively alter morphology or opportunistically respond abiotic morphologic evolution. Consequently, it can be challenging to predict the response of individual sites to changes in mangrove coverage (Horstman et al., 2018b).

Chapter 4 investigates the relative resilience to subsidence of an un-leveed agricultural field near Meinmahla Island. In many deltas, agricultural fields are enclosed by polders or levees that have contributed to meter-scale subsidence in recent decades (Angamuthu et al., 2018; Auerbach et al., 2014; Brown and Nicholls, 2015; Rogers and Overeem, 2017). In contrast, there are fewer embankments in Myanmar, so the impact of the change in vegetation coverage can be evaluated. The goal of this study is to compare the sediment dynamics and morphology of Meinmahla Island with an adjacent, 40-year-old, un-leveed rice field. This comparison

demonstrates the resilience to subsidence of un-leveed fields and emphasizes the importance of maintaining natural sediment transport pathways.

Chapter 5 integrates numerical modeling with punctuated observations of the evolution of Waikaraka Estuary, Aotearoa (New Zealand) as mangrove coverage changed over the last century. In New Zealand, mangrove expansion is associated with estuary infilling and bivalve-habitat degradation (Lovelock et al., 2010; Swales et al., 2007). Mangrove removal programs are often undertaken with the goal of restoring sandy conditions to coastal embayments (Bulmer et al., 2017a; Stokes and Harris, 2015; Swales et al., 2015). In Waikaraka Estuary, mangroves expanded from 1940 until a removal program began in 2005 (Stokes, 2010). This study integrates observational data from June 2019 with numerical modeling in Delft3D to explore the impact of changing mangrove extent on hydrodynamics and sediment transport. Both the *in-situ* observation and modeling underscore the lack of sediment export following removal and highlight the importance of considering site-specific parameters when planning mangrove removals.

The chapters outlined above are followed by a summary and synthesis. These four studies together provide new insights into the evolution of vulnerable coastal environments, both with and without extensive human alteration, over linked spatial and temporal scales.

Chapter 2. SEDIMENT DYNAMICS AND RETENTION IN THE TIDAL- TO ESTUARINE-REACH OF THREE ILLUSTRATIVE DISTRIBUTARIES OF THE AYEYARWADY DELTA[1]

2.1 INTRODUCTION

Predicting the future stability of vulnerable and valuable deltas requires accurate constraints on sediment retention and export at the river-ocean interface. However, sediment discharge for most rivers is measured above the influence of tides, even though the lower, tide-influenced reach of a river can retain 40–70% of the total sediment load (Goodbred and Kuehl, 1998; Milliman et al., 1985; Nittrouer et al., 1995). Previous *in-situ* studies of tidal-to-estuarine sediment dynamics have revealed multiple pathways and mechanisms for sediment retention along the tidally influenced reach of a river.

Starting in the fresh, tidal river, sediment export tends to dominate within channels, while regular overbank flows deposit sediment on floodplain surfaces (Fricke et al., 2019; Hoitink and Jay, 2016; Nowacki et al., 2019). During flood events, sediment delivery can scale non-linearly with fluvial discharge while sediment export scales linearly, leading to net sediment retention (Ralston and Geyer, 2017). At the interface between the tidal river and the estuary, sediment trapping is promoted by flux convergence and reduced bed shear stress (McLachlan et al., 2017).

Processes within the estuary also produce sediment convergence and deposition (Burchard et al., 2018). Stratification can play a significant role in determining when and where sediment is

[1] This chapter was submitted to the Journal of Geophysical Research as Glover, H.E., Ogston, A.S., Fricke, A.T., Nittrouer, C.A., Aung, C., Naing, T., Kyu Kyu, K. and Htike, H. “Connecting sediment retention to distributary-channel hydrodynamics and sediment dynamics in a tide-dominated delta: the Ayeyarwady Delta, Myanmar”, and was accepted for publication on 16 February 2021.

deposited. Typically estuarine stratification is parameterized by comparing the magnitudes of river discharge, which tends to increase stratification, and tidal mixing, which tends to break down stratification (Geyer and MacCready, 2014). Consequently, calculations of sediment flux through the lower river must account for both seasonal variation in discharge and spring-neap tidal cycles. The boundaries of the tidal river and estuary can migrate hundreds of kilometers on seasonal timescales, especially in monsoon-dominated river systems, shifting processes throughout the lower river or onto the continental shelf (Barua, 1990; Geyer et al., 2001; Ogston et al., 2017). Within this complex, tidally influenced region, the sediment flux can be decomposed into a tidally averaged term, representing fluvial advection, and one or more sub-tidal, covariance terms to elucidate the mechanisms driving sediment retention or export (Nowacki et al., 2015; Pritchard and Green, 2017; Xiao et al., 2018).

These previous studies of tidal-to-estuarine sediment dynamics have primarily focused on longitudinal changes along a single river or distributary channel of a river. However, the majority of the largest deltas globally are tide-dominated (Nienhuis et al., 2020) with multiple distributaries that can experience significantly different fluvial, wave, and tidal forcings. Differences in sediment transport pathways can impact sediment residence time, defined as the average age of sediment within the distributary littoral cell. Deltaic and nearshore sediment residence time, in turn, impacts coastal stability and distributary infilling (Burchard et al., 2018; Romans et al., 2016) and nearshore carbon cycling (Blair and Aller, 2012).

Predicting the overall stability of a delta requires understanding these fundamental drivers of sediment residence time within individual distributaries. Prior to human alteration, the seven largest rivers sourced from the Himalayan syntaxis delivered ~5.1 Gt/y of sediment to the coastal ocean (Milliman and Farnsworth, 2011), and the megadeltas formed by these rivers are densely

populated regions of vital economic and ecologic importance. Modern damming has disrupted natural morphology by altering annual hydrographs and dramatically decreasing sediment delivery to the coast. The reduction in sediment supply reduces the capacity for deltas to keep pace with local sea level rise. Moreover, eustatic sea level rise is locally compounded by natural deltaic subsidence and the impacts of deforestation, sub-surface fluid extraction, dredging, and levee construction (Syvitski et al., 2009). The Ayeyarwady and Thanlwin Rivers (also known as Irrawaddy and Salween, respectively) (Figure 2.1), which reach the ocean in Myanmar (Burma), are the only large Asian rivers with no mainstem dams (Grill et al., 2019). Though not pristine, the Ayeyarwady system is also comparatively unaltered by levee construction, water removal, and other human modification, providing a rare opportunity to examine relatively natural deltaic sediment dynamics in a megadelta.

The goal of this study is to evaluate how sediment retention and export vary across a delta by identifying the significant drivers of variability for hydrodynamics and sediment dynamics in three representative distributary channels of the tide dominated Ayeyarwady Delta. These intra-delta findings are then applied to elucidate the controls on sediment retention and coastal stability in monsoon-dominated deltas by comparing the Ayeyarwady Delta to the better-studied and commonly sourced Ganges-Brahmaputra and Mekong Deltas (e.g., Wilson and Goodbred, 2015; Ogston, et al., 2017). Comparing systems where few variables change provides insight into the fundamental connections between deltaic sediment retention and seasonally varying sediment dynamics. Furthermore, comparing modern sediment-transport processes can help elucidate the future stability of the Ayeyarwady Delta, with future human alteration and dam construction (Ketelsen et al., 2017).

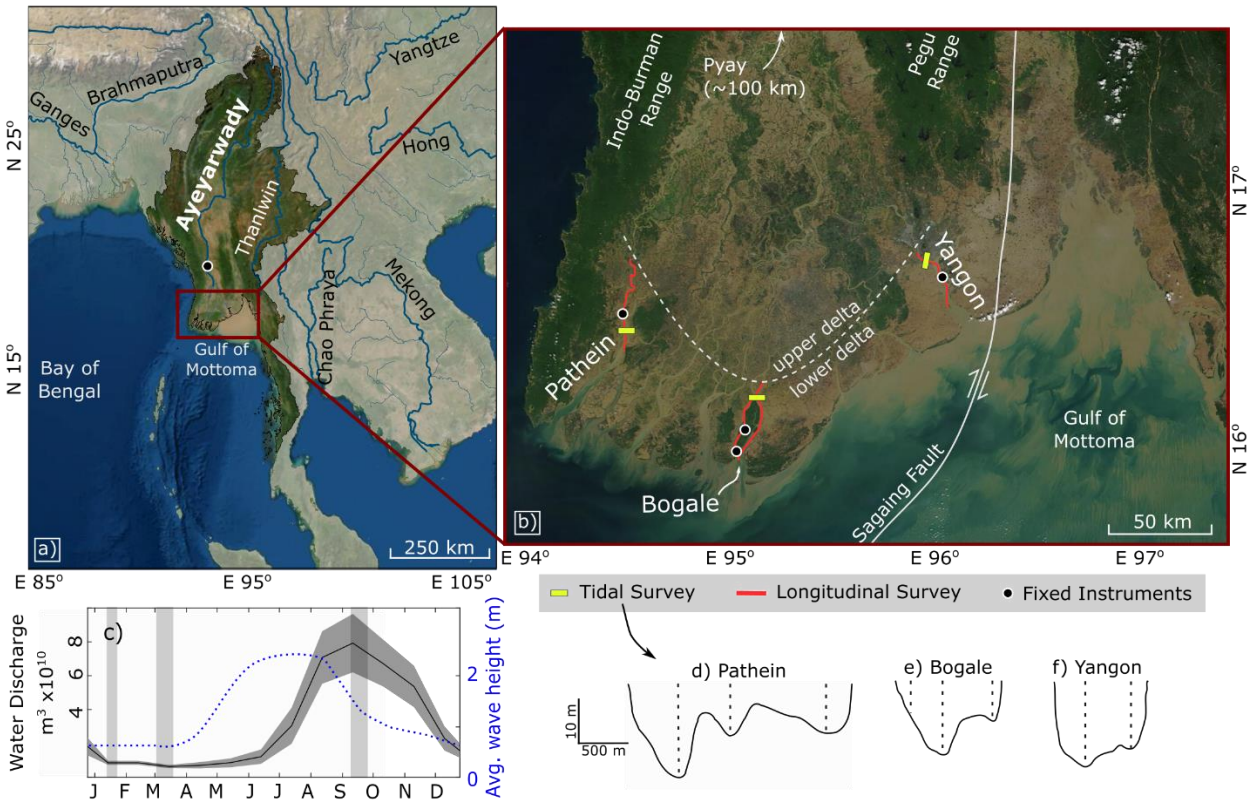

Figure 2.1. Regional map of the study site. Southern Asia (a) with major rivers labelled, the country of Myanmar highlighted, and Pyay labelled with a black circle (imagery accessed through ESRI ArcMap). MODIS imagery of the Ayeyarwady Delta (b) from 9 Dec 2020 (NE monsoon) with relevant features labelled (imagery from the Worldview Snapshots application: https://wvs.earthdata.nasa.gov, part of the Earth Observing System Data and Information System). Tidal survey locations are marked in yellow, longitudinal surveys are marked in red, and fixed instruments are marked with black circles. The mainstem mean monthly discharge (c) at Pyay from 1966–1996 with ±1 standard deviation in dark grey (data from Furuichi et al., 2009), the mean wave height in the Gulf of Mottoma in blue dashed line (data from Anthony et al., 2019), and the sampling surveys marked with light gray shading. Vertically exaggerated bathymetric cross-sections for the Pathein (d), Bogale (e), and Yangon (f) tidal transects are shown with CTD-cast locations as dashed lines.

2.2 STUDY SITE

The Ayeyarwady River (Figure 2.1) drains through the Central Myanmar Basin, between the Indo-Burman Range to the west and the Pegu Range to the east. Previous *in-situ* studies have focused on improving estimates of the fluvial and sediment discharge at the inland apex of the Delta (Baronas et al., 2020; Furuichi et al., 2009; Gordon, 1885; Robinson et al., 2007) and on the fate of sediment in the Gulf of Mottoma (Martaban) and adjacent shelf (Kuehl et al., 2019; Liu et al., 2020).

The current annual discharge at Pyay (Figure 2.1) is $379\pm9\times10^9$ m^3 of water and 326±91 Mt of sediment (Baronas et al., 2020). Agricultural irrigation and tributary damming have decreased the total discharge of the river since the first gauging in 1869–1879, when the river discharged $422\pm41\times10^9$ m^3 of water and 364±60 Mt of sediment (Furuichi et al., 2009; Robinson et al., 2007). However, Ayeyarwady River discharge has decreased significantly less than in other large river systems. The combined Ayeyarwady and Thanlwin Rivers currently carry the third largest sediment load globally, whereas the system was the seventh largest prior to modern damming of other major rivers (Chen et al., 2020; Milliman and Farnsworth, 2011).

South of Pyay, the Ayeyarwady River splits into 7–11 interconnected distributaries, which drain into the Gulf of Mottoma, in the Northern Andaman Sea (Figure 2.1b). There is limited data on the partitioning of water and sediment discharge through the Delta, and it is challenging to accurately partition discharge in tide-dominated systems without comprehensive field measurements. For example, water discharge has been accurately partitioned using a salt-intrusion model based on extensive in-situ measurements in the Mekong River (Nguyen et al., 2008), though a comparable model has not been developed for sediment. Sediment discharge can be effectively partitioned using remote sensing of morphology in fluvial-dominated systems (Dong et al., 2020),

but this method has not yet been validated for tide-dominated systems. In the Ayeyarwady Delta, previous estimates of distributary discharge have primarily relied on remote sensing and modeling (Brakenridge and Kettner, 2018) or limited surveys at bifurcations far from the coastline (Brichierei-Colombi, 1983; Kravtsova et al., 2009). This study focuses on the western Pathein, central Bogale, and eastern Yangon distributaries, which represent the full range of distributary discharge conditions. A recent review suggested that the Pathein and Yangon distributaries each carry <10% of the total Ayeyarwady River water discharge and that the Bogale carries up to 19% (Chen et al., 2020), however these values will be challenged here.

Approximately 80% of Ayeyarwady River discharge occurs during the southwest (SW) monsoon in May–October, when moist, southwest winds bring heavy rains (Figure 2.1c). In October, the winds gradually switch to the northeast (NE). Precipitation decreases and dry NE-monsoon conditions persist until May (Rodolfo, 1969). Ocean conditions in the Gulf of Mottoma are controlled by the monsoon. Prevailing currents flow clockwise around the Gulf (from west to east along the delta shoreline) during the SW monsoon, and counterclockwise during the NE monsoon. Wave energy increases during the SW monsoon, especially along the western portion of the delta (Kuehl et al., 2019). The three distributaries studied here represent this full range of seasonally varying wave conditions. For later comparison, it is important to note that the Ganges-Brahmaputra Delta experiences the same seasonal covariance of discharge and ocean energetics as the Ayeyarwady Delta (Wilson and Goodbred, 2015). In contrast, the Mekong River high-discharge season coincides with quiescent offshore conditions due to its coastal orientation (Eidam et al., 2017).

The spring tidal range in the Gulf of Mottoma increases from ~2 m at the mouth of the Pathein distributary to ~6 m at the mouth of the Yangon distributary (Kravtsova et al., 2009), so

the three studied distributaries also cover the full range of tidal conditions across the delta. The upper Bay of Bengal, where the Ganges-Brahmaputra River discharges to the ocean (Fig 1a), is similarly macrotidal as a result of tidal amplification (Wilson and Goodbred, 2015) while the Mekong is solely mesotidal.

The delta front advanced ~80 km in the past 8100 years, with average progradation rates of 7–25 m/y (Giosan et al., 2018). However, the modern coastline has been remarkably stable since the 1850s, suggesting that an equilibrium extent has been reached at the southern end of the Indo-Burman Range (Hedley et al., 2010; Kuehl et al., 2019). Sediment deposition and accumulation are variable on the continental shelf adjacent to the Ayeyarwady Delta. Sediment deposited during the SW monsoon is rapidly remobilized and carried into the upper Gulf or to deeper waters. The strong tidal currents in the upper Gulf continually rework the bed and maintain elevated suspended-sediment concentrations (Ramaswamy et al., 2004). Sediment accumulation is most rapid in the southeastern region of the Gulf, where accommodation space is generated by crustal movement associated with the Sagaing Fault (Kuehl et al., 2019). Overall, examining the western Pathein, central Bogale, and eastern Yangon distributaries provides insight into the full range of hydrodynamic and sedimentary conditions across the Ayeyarwady Delta. Here we present the first investigation of sediment dynamics within the tidal-to-estuarine reach of the Ayeyarwady Delta and use these results to improve our understanding of deltaic sediment retention and stability.

2.3 METHODS

2.3.1 *Fixed instruments*

Water-level, salinity, and turbidity sensors were installed in the Yangon, Bogale, and Pathein distributaries (Figure 2.1b) from February 2017 to September 2019 to capture seasonal variability. In the Yangon distributary, Onset HOBO® water-level and conductivity loggers were deployed

~25 km from the mouth. In the Bogale distributary, Onset HOBO water-level and conductivity loggers were deployed with an RBR Solo® optical backscatter sensor (OBS) both ~12 km and ~23 km from the mouth. In the Pathein distributary, an Onset HOBO water-level logger and an RBR Solo OBS were deployed ~85 km from the mouth; the associated salinity sensor was lost in a flood. All instruments were set to sample at 10-min intervals; gaps in the record are due to instrument damage and loss (Figure 2.2).

2.3.2 *Boat-based longitudinal surveys*

Longitudinal surveys of water properties and bed texture were conducted along all three distributaries during high flow (September 2017) and low flow (March 2018, January 2019). Surveys were conducted while transiting against the tide (e.g., upriver against the ebb) to increase the probability of accurately capturing the structure of the estuary. Water-column profiles were collected using an RBR, Ltd. Concerto® CTD with integrated optical backscatter (Campbell Scientific OBS-3+®) sampling at 6 Hz. Water samples were collected at the surface and ~1 m above bed using a Niskin sampler. Suspended-sediment concentration (SSC) was measured by filtering 0.05–0.15 L of water through a pre-weighed 0.45-μm nitrocellulose filter. The CTD-OBS and RBR Solo voltage responses were converted to SSC using concurrent surface-water samples ($r^2 = 0.86–0.91$). The CTD-OBS was unreliable at concentrations >3.6 g/L, and the RBR Solo was unreliable at concentrations >1.4 g/L. In-situ water samples provided accurate point measurements when SSC exceeded these thresholds.

Bed sediment was collected using a Van Veen grab sampler and suspended-sediment samples were collected from Niskin water samples for grain-size analysis. Both types of samples were disaggregated by sonicating in a 0.05% sodium metaphosphate solution, and grain size was measured using a Beckman-Coulter LS13-320® Particle Size Analyzer.

2.3.3 *Boat-based tidal surveys*

In the Yangon and Bogale distributaries, discharge and bed texture were monitored over a tidal cycle during high- and low-river flow at a single transect location (Figure 2.1b). Transects were occupied for a 12.5-hr period during high flow, which was sufficient to calculate residual discharge based on the symmetry of the tides (Figure 2.2). During low flow, some transects were occupied for a <12.5-hr period due to safety limitations. Flow velocity was measured with a 600-kHz Teledyne RD Instruments Acoustic Doppler Current Profiler (ADCP). The vessel traversed the transect in 15–20 min; flow velocity was measured in both transiting directions and water-column profiles or bed samples were collected at 2–3 locations in one of the directions. The sampling locations were defined based on transect bathymetry (Figure 2.1d-f).

2.3.4 *Data processing*

For the tidal surveys, spurious data points were removed from the ADCP and CTD data, and gaps in profiles were filled using linear interpolation. Missing near-bed values were extrapolated using cubic-spline interpolation and a no-slip assumption to preserve the shape of the velocity profile, while missing surface values were filled with nearest neighbors. Velocity was defined in a channel-wise coordinate system consistent with QRev (Mueller, 2016), the standard software used by the US Geological Survey; positive along-channel values are downstream and positive across-channel values are towards the right bank.

Bed shear stress was calculated indirectly from velocity profiles at three stations, following the methodology of McLachlan et al. (2017). Ultimately, the bed shear stress was calculated using the Quadratic Stress Law:

$$\tau = \rho C_d \bar{u}_z^{\,2} \tag{2.1}$$

where ρ is density calculated from the CTD profile, C_d is the drag coefficient at depth z, and $\bar{u}_z$ is the mean velocity at height z above the bed. The mean velocity was calculated at z = 2 m, the deepest ADCP bin with consistent data. A median drag coefficient was calculated at each station using selected profiles with steady flow conditions and was assumed to apply over the full transect time period. First, velocity profiles were averaged laterally over 50 m surrounding the station to reduce noise due to eddies on the order of the water depth. Then bed shear velocity was calculated by fitting a slope to the lower half of the velocity profile using the Law of the Wall:

$$\frac{\bar{u}_z}{u_*} = \frac{1}{\kappa}\ln\left(\frac{z}{z_0}\right) \tag{2.2}$$

where u_* is the bed shear velocity, z_0 is the roughness length, and κ is the von Kármán constant, 0.41. The drag coefficient was calculated by assuming:

$$C_d = \frac{\bar{u}_z{}^2}{u_*{}^2} \tag{2.3}$$

(Sternberg, 1968). Values fell within the range of 0.0032–0.007. This methodology provided full temporal coverage over tidal surveys regardless of data gaps and periods of non-steady flow, allowing for comparison between surveys and distributaries.

The residual fluxes of water and sediment were calculated for each tidal survey using a sigma coordinate system, where depth is normalized to 0 at the surface and 1 at the bed ($\sigma = \frac{z}{h}$). This methodology is commonly applied where the cross-sectional area of an estuary, A, varies significantly with the tide (Giddings et al., 2013; Nowacki et al., 2015). The cross-sectional area was divided into 20 grid cells, dA. Transects of SSC were generated by linearly interpolating between CTD profiles. The residual flux was calculated:

$$F = \langle \int u\, c\, dA \rangle \tag{2.4}$$

where $u(y,\sigma,t)$ is velocity and $c(y,\sigma,t)$ is the concentration of salt or suspended sediment, and ‹› denotes tidal averaging. The residual flux of water was calculated by setting c to unity; this calculated water discharge was consistent with the output of QRev. For the incomplete low-flow surveys, discharge was calculated using a Fourier fit to the tidal discharge curve (see Figure A.S1 for more details). Error is not typically reported in calculations of residual discharge from repeat tidal transects. Here, error was estimated by calculating the RMSE of this Fourier fit to the water discharge curve. Sediment flux was not well represented by a Fourier series, so missing data were filled for each grid cell by cubic interpolation of average velocity and SSC.

The sediment flux was analytically decomposed to investigate the physical drivers of transport. The residual flux was decomposed into a spatially and tidally averaged component, F_R, a spatially varying and tidally averaged component, F_E, and a spatially and tidally varying remainder term, F_T (Lerczak et al., 2007; MacCready and Banas, 2012; Nowacki et al., 2015):

$$F = u_0 c_0 A_0 + \int u_1 c_1 dA_0 + \left\langle \int u_2 c_2 dA \right\rangle = F_R + F_E + F_T$$

$$u_0 = \frac{\langle \int u\, dA \rangle}{A_0}; c_0 = \frac{\langle \int c\, dA \rangle}{A_0};\ u_1 = \frac{\langle u\, dA \rangle}{dA_0} - u_0;\ c_1 = \frac{\langle c\, dA \rangle}{dA_0} - c_0;$$

$$u_2 = u - u_0 - u_1;\ c_2 = c - c_0 - c_1 \quad (2.5)$$

The first term, F_R, is generally interpreted as flux associated with river advection, which incorporates Stokes Drift. The next term, F_E, is interpreted as the estuarine exchange flux, resulting from tidally averaged estuarine circulation. The residual term, F_T, incorporates other covariance between flow and concentration, such as eddies produced by bathymetry and local deposition/resuspension of sediment. However, care must be taken when interpreting these results because the terms are not derived from physical forcings.

Finally, the estuarine conditions were broadly classified using the parameterization described in Geyer and MacCready (2014). Fluvial input is represented by the freshwater Froude number (F_{Rf}) and the tidal forcing is represented by a mixing parameter (M):

$$F_{Rf} = \frac{U_R}{\sqrt{\beta g S H}} \qquad M^2 = \frac{C_D U_T^2}{\omega N_0 H^2} \tag{2.6}$$

where U_R is the river discharge velocity ($\langle \int u\, dA \rangle / A_0$), U_T is the depth-averaged tidal velocity, β is the coefficient of salinity, g is gravity, S is ocean salinity, H is the distributary depth, C_D is the drag coefficient, ω is the tidal frequency, and N_0 is the buoyancy frequency ($\sqrt{\frac{-g}{\rho_0}\frac{d\rho}{dz}}$). An estuary will plot as a region in this parameter space, based on seasonal and spring-neap tidal variability.

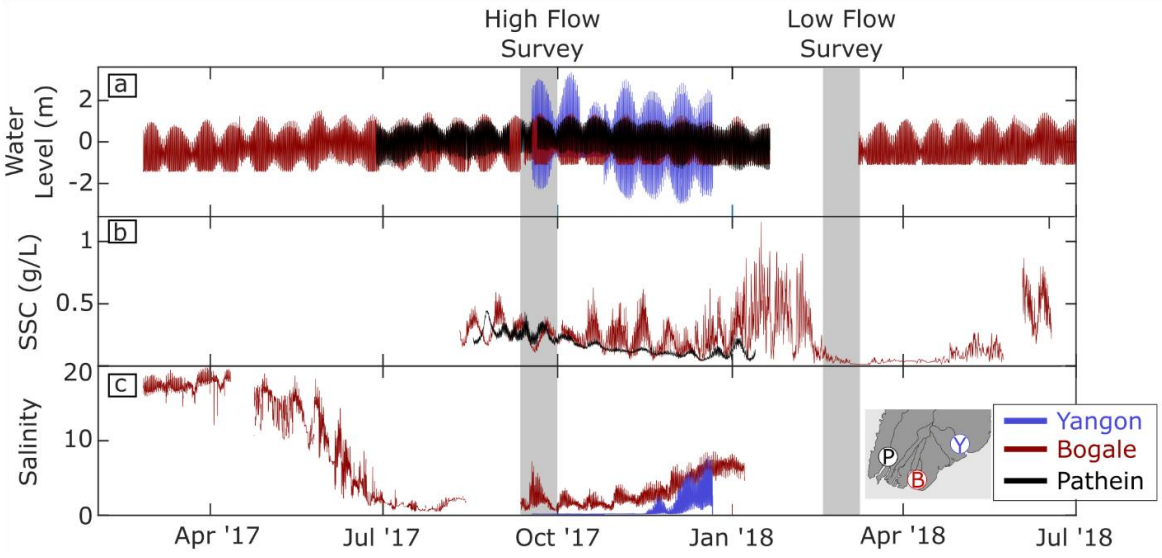

Figure 2.2. Fixed-instrument records. Fixed-instrument measurements of water level (a), SSC (b), and salinity (c) in the Yangon (blue), Bogale (red), and Pathein (black) distributaries over the study period (see Figure 2.1b for observation locations). The September 2017 and March 2018 field seasons are marked in grey. This fixed-instrument record did not cover the January 2019 field season. The inset map shows the locations of the sample sites across the delta.

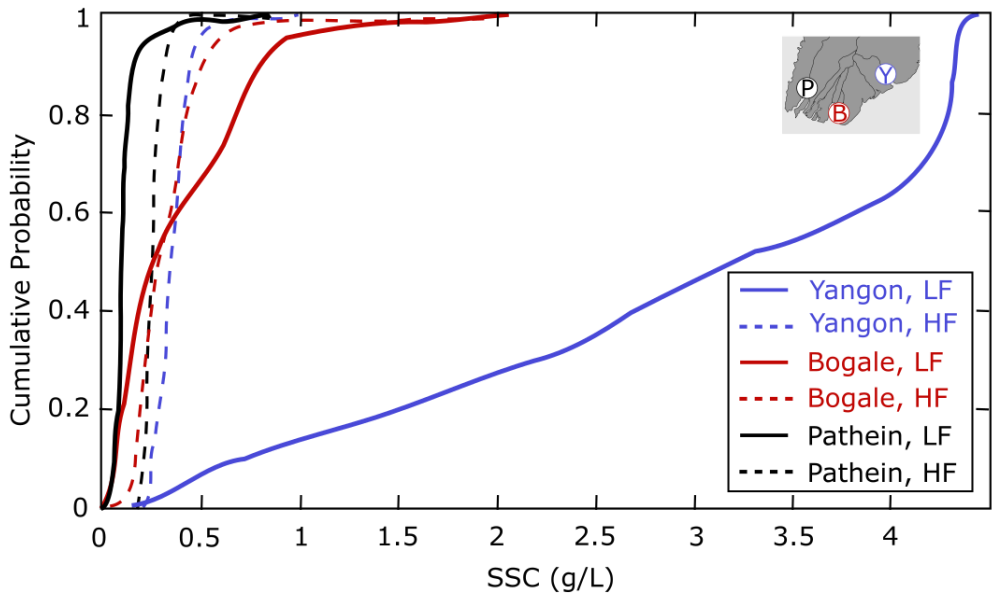

Figure 2.3. Cumulative SSC probability in the Yangon (blue), Bogale (red), and Pathein (black) distributaries during high (solid lines) and low (dashed lines) flow surveys. Values primarily represent longitudinal- and tidal-survey CTD casts; surface and near-bed water samples are also included. The inset map shows the locations of the sample sites across the delta.

2.4 RESULTS

2.4.1 *Seasonal shifts in salinity and suspended sediment*

The lower reaches of the Pathein, Bogale, and Yangon distributaries transitioned seasonally between tidal river and estuarine regimes (Figure 2.2). In the Yangon distributary, salinity first rose to measurable levels at the instrument site, ~25 km inland, in mid-November. Estuarine conditions likely persisted until mid-June, the onset of the SW monsoon. In the Bogale distributary, the lower 15 km were estuarine throughout the year, with salinity values of 1-2 from July to Oct. Salinity began increasing in October and peaked at 20 in February–March.

The seasonal shifts in SSC were different in each distributary (Figure 2.3). During high-flow, the SSC was consistently 0.1–0.4 g/L in all three distributaries. The median concentration in the Pathein distributary was 0.25 g/L, slightly less than that in the Bogale (0.28 g/L) or Yangon

(0.36 g/L) distributaries. During low flow, SSC in the Pathein decreased to a median value of 0.10 g/L. In the Bogale distributary, the median SSC remained about the same as in high flow, though the maximum SSC increased to >3 g/L. In the Yangon distributary, the median SSC dramatically increased to 3.3 g/L, with peak concentrations measured in SSC samples >10 g/L. The grain size of the sediment in suspension was consistent between distributaries. On average, the sediment was 60% clay and 40% silt during the high flow and 35% clay and 65% silt during low flow.

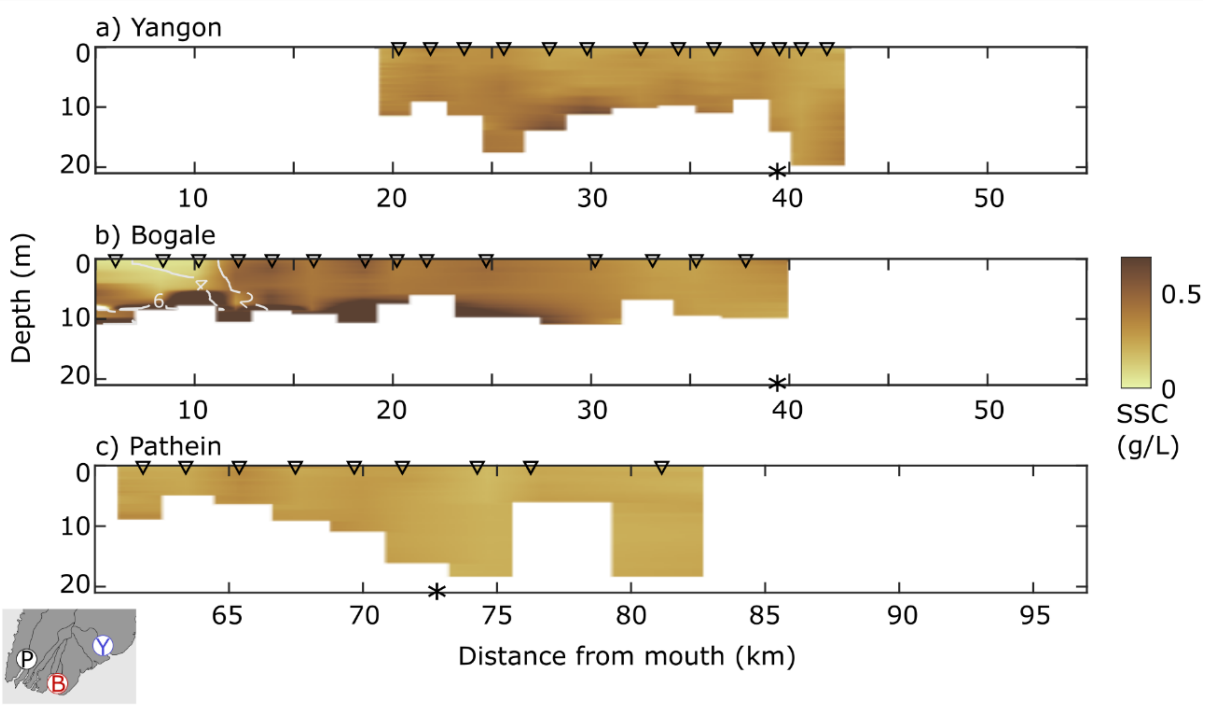

Figure 2.4. Salinity and SSC along the Yangon (a), Bogale (b), Pathein (c) distributaries during high flow. SSC is plotted in color and salinity is contoured at intervals of 2. The transect locations are marked with asterisks. Note the change in x-axis for the Pathein distributary. CTD-cast locations are marked with triangles; casts were not always collected in the thalweg. The inset map shows the locations of the sample sites across the delta.

Table 2.1. Summary of hydrodynamics and sediment dynamics in the Yangon, Bogale, and Pathein distributaries. Missing data are indicated with "nd".

		Tidal Range m	Median (Max) SSC, g/L	Salt-Intrusion Length, km	Regime at Transect	Residual Water Flux (RMSE), m^3/s		% of Total HF Disch.	Residual Sediment Flux, t/s	
						Spring	Neap		Spring	Neap
Yangon	HF	6	0.36 (0.69)	nd	Tidal River	nd	7830 (660)	30	nd	3.3
	LF		3.3 (16)	55	Partially Mixed	nd	1210 (650)		nd	2.7
Bogale	HF	3	0.28 (1.0)	15	Tidal River	1200 (340)	1960 (160)	5	0.7	0.47
	LF		0.26 (6.3)	42	Partially Mixed/ SIPS	480 (260)	-510 (400)		0.12	-0.03
Pathein	HF	2.5	0.25 (0.45)	nd	Tidal River	6400 (2000)	nd	20	1.5	nd
	LF		0.10 (0.87)	90	Partially Mixed	nd	nd		nd	nd

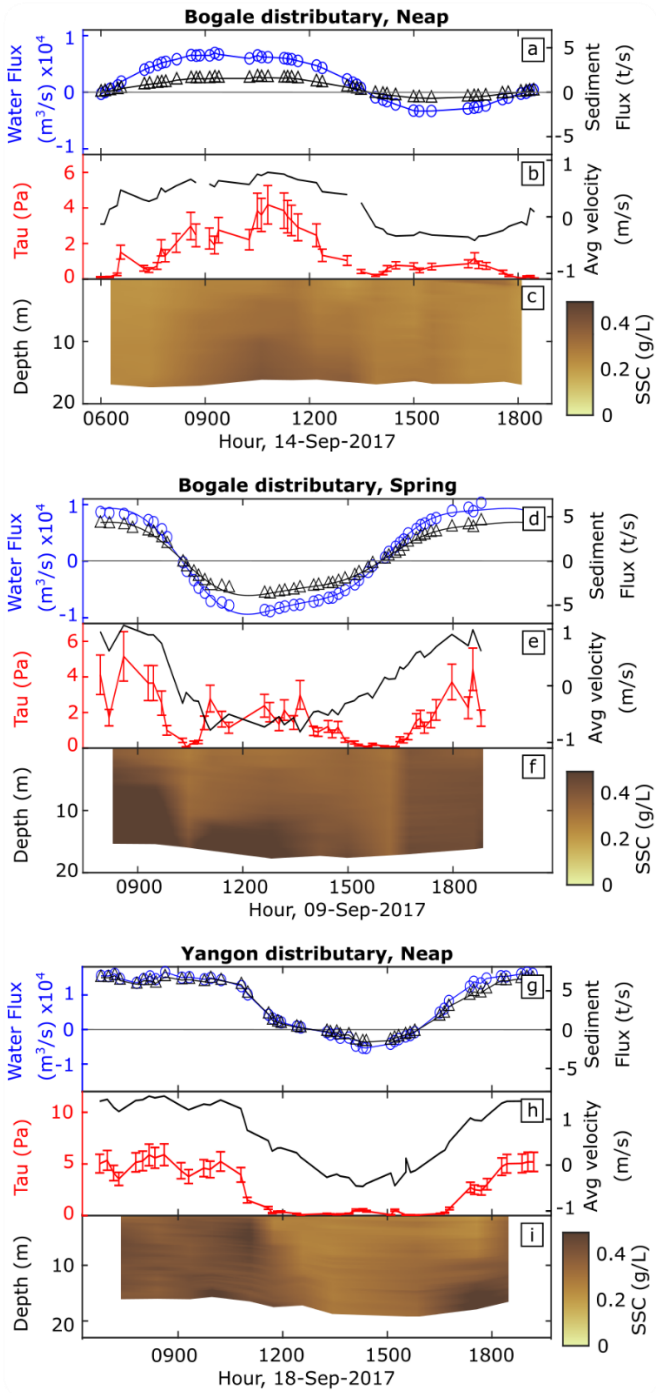

Figure 2.5. High-flow season, tidal-survey data. From the Bogale distributary for neap (a–c) and spring (d–f) tides and from the Yangon distributary for neap (g-i) tide. Panels a), d) and g) show the total instantaneous water (blue circles) and sediment (black triangles) fluxes. Panels b), e) and h) show the bed shear stress ±1 standard deviation (red) and average water velocity (black). Panels c), f) and i) show the SSC averaged over the cross sectional. Note the changes in scales for the Yangon distributary.

2.4.2 *Longitudinal and tidal surveys during the high-flow season*

During high flow, estuarine conditions were primarily seaward of the observation regions, and possibly seaward of the distributary mouths. Salt was not observed during the longitudinal surveys of the Yangon or Pathein distributaries, where the most seaward observations were at ~19 and ~60 km inland, respectively (Figure 2.4a,c). The longitudinal survey in the Bogale extended to 5 km from the river mouth, where salinity values were ~6; the salt-intrusion length was 15 km (Figure 2.4b). The greatest SSC was observed within ~1 m of the bed in all three distributaries, though these turbid regions were not uniform along-channel. Above this boundary layer, the SSC was relatively homogeneous. There was more variability within the estuarine region of the Bogale distributary, where concentrations in the upper 5 m of the water column were less than the mean and near-bed concentrations were greater than the mean (Figure 2.4b).

In the Bogale distributary, the instantaneous water discharge varied between -8890 and 10600 m^3/s during the spring survey and between -3450 and 6880 m^3/s during the neap survey (Figure 2.5a,d). The resulting residual discharge was greater for the neap survey (Table 2.1). The neap water velocity was also strongly ebb dominant; the mean water speed was twice as fast during peak ebb as during peak flood tide. The spring-survey water velocity was still ebb dominated, but the speeds were less asymmetric. Bed shear stress peaked towards the end of the ebb tide at ~4 Pa during both surveys (Figure 2.5b,e). The shear stresses consistently exceeded the 0.4 Pa threshold of erosion for coarse sand (Miller et al., 1977) except around slack high and low water (see Section 2.4.5 for a discussion of grain size). The tidally averaged bed shear stress was greater during spring tide than during neap tide due to the stronger spring flood-tide velocities.

The pattern of SSC was consistent with that of the shear stress (Figure 2.5c,f), and the residual sediment flux was greater over the spring survey despite the lesser water discharge. The

greatest SSC values were observed during peak ebb and flood currents and were relatively uniform throughout the water column. SSC decreased close to slack high and low tide, especially in the upper 10 m of the water column, indicating sediment settling. Rouse profiles fit to these transitions indicate that the median settling velocities were 0.05–0.2 cm/s, suggesting particle aggregation.

In the Yangon distributary, the survey was conducted during an apogean neap tide (Figure 2.5 g-i). Discharge, velocity, shear stress and SSC followed similar patterns to those in the Bogale distributary during the neap survey. The instantaneous water discharge varied between -5540 and 16800 m^3/s and the sediment discharge varied from -1.66 to 7.01 t/s. The residual water flux, 7830 m^3/s, and sediment flux, 3.28 t/s, were significantly greater than that in the Bogale distributary (Table 2.1). The estimated error in residual water discharge was ~8% in both the Yangon and the Bogale distributaries. The water velocity and shear stress remained weak from slack low tide through slack high tide, and the SSC decreased (Figure 2.5i). During the turn of the tide, SSC decreased from the surface downward; the median settling velocity estimated from the Rouse profiles was 0.077 cm/s. SSC was relatively uniform through the water column during the ebb tide.

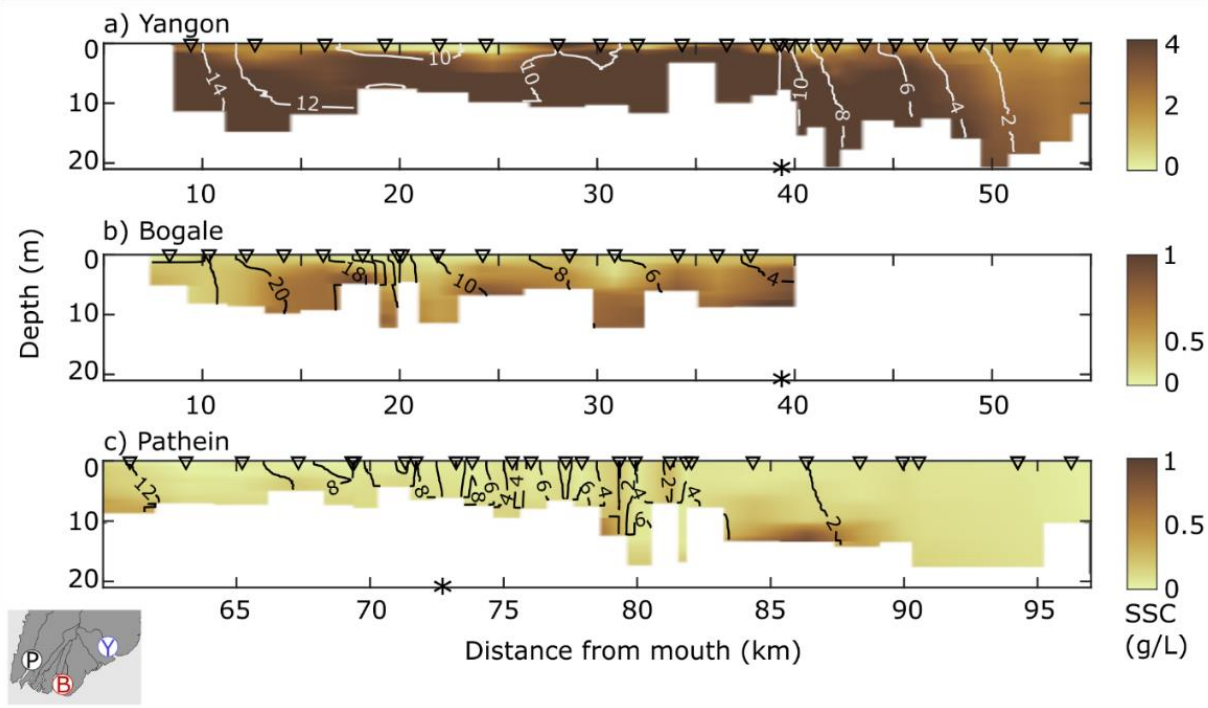

Figure 2.6. Salinity and SSC in the Yangon (a), Bogale (b), Pathein (c) distributaries during low flow. SSC is plotted in color and salinity is contoured at intervals of 2; note the change in SSC scale for the Yangon distributary. The transect locations are marked with asterisks. Note the change in x-axis for the Pathein distributary. CTD-cast locations are marked with triangles; casts were not always collected in the thalweg. The inset map shows the distributary locations across the delta.

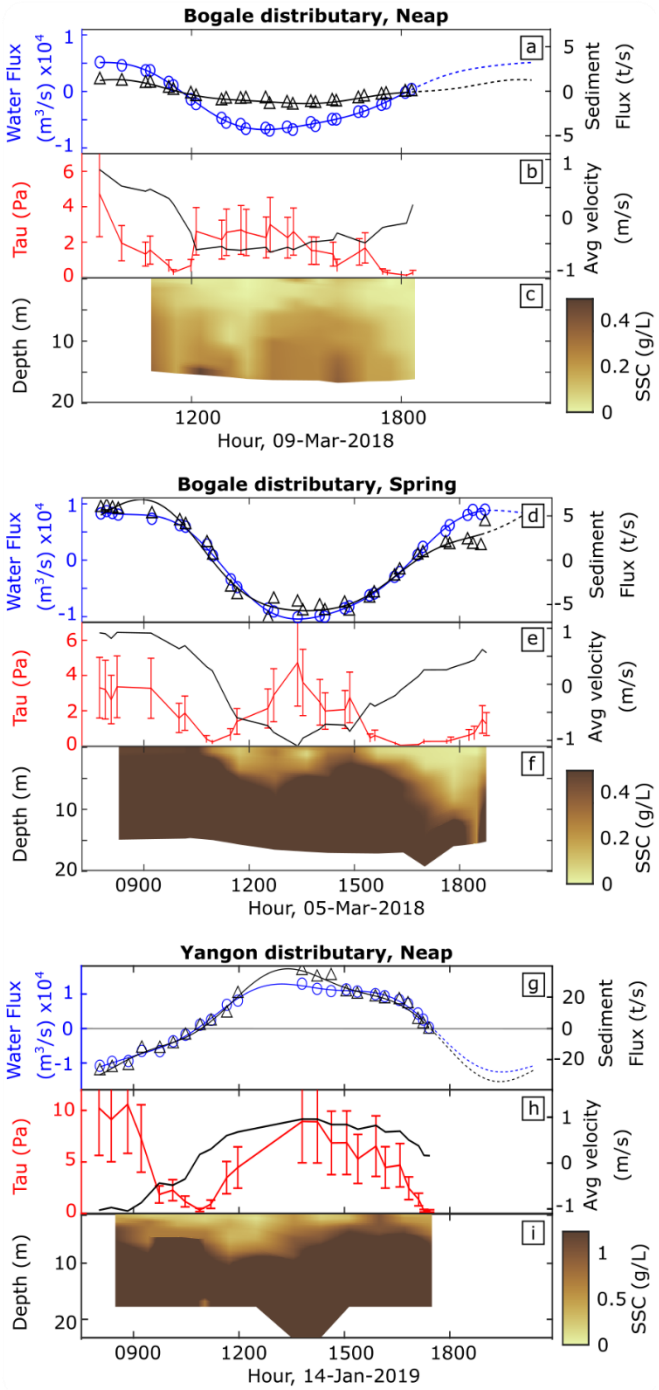

Figure 2.7. Low-flow season, tidal-survey data. From the Bogale distributary for neap (a–c) and spring (d–f) tides and from the Yangon distributary for neap (g-i) tide. Panels a), d) and g) show the total instantaneous water (blue circles) and sediment (black triangles) fluxes. Panels b), e) and h) show the bed shear stress ±1 standard deviation (red) and average water velocity (black). Panels c), f) and i) show the SSC averaged over the cross sectional. Note the changes in scales for the Yangon distributary.

2.4.3 *Longitudinal and tidal surveys during the low-flow season*

The longitudinal survey of the lower Yangon distributary was collected over two days during a spring tide. The salt-intrusion length was ~55 km (Figure 2.6a). The majority of the estuary was partially mixed, shifting towards salt-wedge stratification within 20 km of the mouth. Peak salinity values were ~15. SSC was consistently >1 g/L, except for the upper 3 m of the water column, where concentrations dropped to 0.7 g/L. The depth-averaged SSC decreased upriver.

In the Bogale distributary, the longitudinal survey was conducted during the transition from spring to neap tides. The salt-intrusion length was ~42 km, and the estuary was generally partially mixed. The maximum salinity was 22 at ~7 km (Figure 2.6b). The SSC was more variable in the Bogale than in the Yangon distributary. The peak SSC was ~1 g/L, and concentrations were generally greater near the bed, similar to the high-flow survey.

The longitudinal survey of the Pathein distributary was collected over two days during the transition from neap to spring tides. The salt-intrusion length was ~90 km, longer than that in the Yangon or Bogale distributaries (Figure 2.6c), and the estuary was partially mixed. SSC was uniformly low throughout the water column and along the estuary, except for one region of ~0.6–0.7 g/L near the bed. There was no observed estuarine turbidity maximum.

As during high flow, tidal surveys were collected in the Bogale distributary during spring and neap tides (Figure 2.7a-f). The amplitude of tidal variation in the instantaneous discharge was greater during the spring than the neap survey. The residual water discharge values were comparable to the error in fitting the tidal curve and could not be distinguished from zero. The shear stress followed the same pattern as velocity, with maxima at mid-tide. The peak ebb tide was not captured during either survey. This data gap may explain the negative residual discharge for

the neap tide. It is also possible that there is exchange with adjacent distributaries via tidal channels.

The magnitudes of SSC and sediment flux differed significantly between neap and spring surveys, though the intratidal patterns were similar (Figure 2.7 c,f). The average SSC was 0.58 g/L during the spring survey and 0.18 g/L during the neap survey. Overall SSC covaried with velocity, especially in the upper 5–10 m of the water column, as it did during the high-flow surveys. During the neap survey, there were near-bed peaks in SSC during the onset of ebb and flood tidal currents, indicative of resuspension. However, SSC in the lower water column remained >0.7 g/L throughout the tidal cycle during the spring survey.

In the Yangon distributary, a tidal survey was collected during a neap tide (Figure 2.7g-i). The instantaneous water discharge fluctuated between -13000 and 12900 m^3/s. The flood velocities were significantly greater than those observed during the high-flow survey. The Yangon, low-flow residual discharge was comparable to the high-flow discharge of the Bogale distributary (Table 2.1). Bed shear stress was strong, peaking at ~10 Pa, and relatively symmetric between ebb and flood tide. The error bounds were larger due to the greater turbidity, which reduced near-bed data quality. SSC remained >1 g/L throughout the water column and was relatively consistent over the tidal cycle, except in the upper 5 m of the water column. The resulting instantaneous sediment flux fluctuated between -34 to 38 t/s, more than an order of magnitude larger than the residual flux. The positive residual sediment flux indicates that there was no net sediment import, however, a portion of the flood tide was not recorded.

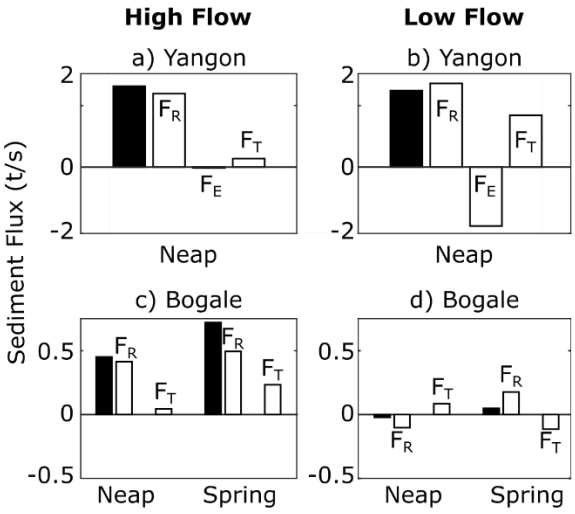

Figure 2.8. Sediment-flux decomposition for the Yangon and Bogale distributary channels during high and low flow. The black bar is the total flux, and the bars for the decomposed fluxes are labelled. Note the difference in scale between distributaries.

2.4.4 *Sediment-flux decomposition*

The three-part decomposition was applied to the Bogale and Yangon distributary tidal surveys (Figure 2.8). The flux decomposition was similar in both distributaries during high flow. Sediment export was dominated by river advection, represented in F_R. Further export was driven by tidal residual processes, F_T, which can be related to deposition and resuspension. In contrast, the sediment-flux decomposition differed between the Yangon and Bogale distributaries during low flow. In the Yangon, river advection and residual tidal processes were still driving sediment export, but there was also a significant import of sediment driven by estuarine exchange, F_E. These patterns likely hold even with the greater magnitude of error in the Yangon distributary data. In the Bogale distributary, the fluxes were small overall making it challenging to identify the important drivers of sediment transport. However, there was no strong import signal due to estuarine exchange. Instead, tidal processes balanced fluvial advection.

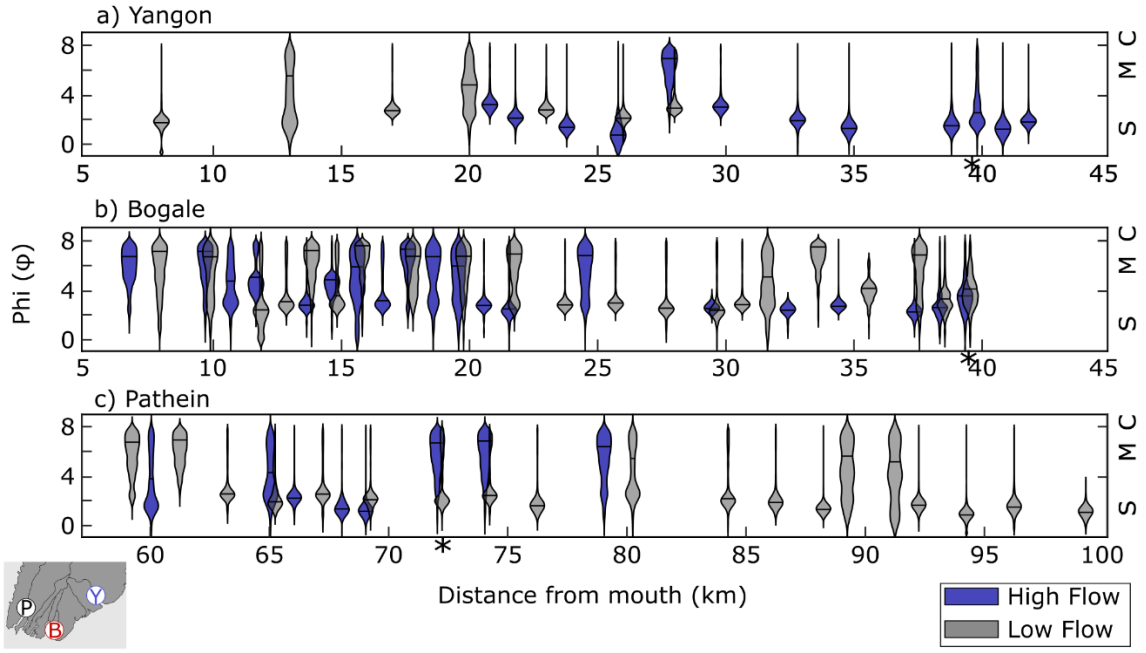

Figure 2.9. Violin plots of bed-sediment grain size from individual grab samples in the Yangon (a), Bogale (b) and Pathein (c) distributaries during high (dark blue) and low (gray) flow. Each symbol is a mirrored probability distribution function. Samples are offset by 100 m between seasons to aid in interpretation; note the change in x-axis for the Pathein distributary. The tidal transect locations are marked with asterisks. S=Sand, M=Silt, C=Clay are shown for reference on the right y-axis. The inset map shows the locations of the sample sites across the delta.

2.4.5 *Bed-sediment grain size*

The bed sediment varied seasonally and between distributaries. In the Yangon, the bed was sandy, with very coarse sand observed in the thalweg during both high and low flow (Figure 2.9a). There was a high rate of grab-sample failure, probably indicating that the bed was hard. The bed was likely altered by sand mining and dredging activities for the port; mud deposits were observed outside the thalweg, south of the city of Yangon.

In the Bogale distributary, mud was draped over sand during both high and low flow (Figure 2.9b). The sand was generally finer than that observed in the Yangon distributary. The regions of mud deposition were not obviously correlated with hydrodynamic regions such as the

salt-intrusion length during either season. However, mud content generally increased in the seaward direction. Eroded mud balls were also observed throughout the region in both seasons. Overall, bed sediment was slightly finer during low flow at the transect location: there was 75% sand on average during high flow and 65% sand during low flow. This shift was more pronounced at stations outside of the thalweg, where there was 84% sand during high flow and 64% sand during low flow. The Pathein distributary had similar trends to those observed in the Bogale distributary (Figure 2.9b,c). There were patchy mud deposits, with mud commonly draped over sand. There was a seaward-fining trend during the low-flow season. In all distributaries, across-channel variability added complexity to longitudinal trends.

2.5 DISCUSSION

2.5.1 *Comparing distributaries of the Ayeyarwady Delta*

The comparison of three representative distributaries of the Ayeyarwady Delta demonstrates the high degree of variability within a single delta system and the importance of investigating multiple distributaries, especially when assessing the overall stability of megadeltas. During the high-flow season, the Yangon, Bogale, and Pathein distributaries were largely tidal rivers exporting sediment to the Gulf of Mottoma. The residual discharge of water was ~7800 m^3/s in the Yangon, 1200–2000 m^3/s in the Bogale, and ~6400 m^3/s in the Pathein. Extrapolating these values to monthly discharge, the Yangon carried ~30%, the Bogale carried ~5%, and the Pathein carried ~25% of the total Ayeyarwady River discharge (Table 2.1).

The measured discharges of the Yangon and Pathein distributaries are significantly greater, and the Bogale is significantly lower than those reported in Brichierei-Colombi (1983) and Chen (2020). These differences may be due in part to improvements in sampling techniques and

differences between remote sensing or modeling and *in-situ* observations. These discrepancies may also indicate that the discharge partitioning at inland bifurcations does not reflect the discharge to the ocean. The distributaries are highly connected in the lower delta (Figure 2.1b), and flow may be exchanged. It is also possible that some of the discharge measured in the lower Pathein distributary is sourced from the southernmost Indo-Burman mountain range, not the mainstem of the Ayeyarwady River. The published estimates for the other Ayeyarwady distributaries should be used with caution until further field measurements can confirm the discharge partitioning.

SSC was comparable between all three distributaries during high flow, with concentrations in the range of 0.2–0.4 g/L. Over a tidal cycle, SSC varied within the water column as sediment was temporarily deposited and resuspended (Figure 2.5c,f,i). The residual sediment export scaled linearly with water discharge by distributary. Based on this relationship, sediment retention within the upper delta can be estimated based on a simple box model of the fluvial input to each distributary and the residual sediment export at the sampling transects (Table A.S2 and Figure A.S3). Here, the delta is divided into an upper and lower region based on where data have been collected (Figure 2.1b). During high flow we can assume that the sediment partitioning between distributaries is roughly equal to the water partitioning because SSC was consistent across distributaries (Table 2.1). Based on the difference between this sediment partitioning and the residual sediment export, 20–60% of the sediment is retained within the upper delta during high flow, likely via overbank flows. During low flow, floodplain deposition is likely to decrease, lowering the total for the annual percent sediment retention. This retention also results in a shift in suspended-sediment grain size. The mean D_{50} at Pyay was ~30 µm (Baronas et al., 2020) and the

mean at the transect locations was <10 μm, indicating preferential retention of coarser mud in the upper delta during high flow.

This new estimate of percent sediment retention within the Ayeyarwady Delta is comparable to estimates in other large river systems (Goodbred and Kuehl, 1998; Milliman et al., 1985; Nittrouer et al., 1995), again demonstrating that non-tidal, mainstem sediment flux may not be representative of sediment delivery to the ocean. Furthermore, floodplain deposition is critical to the capacity for natural deltas to keep pace with sea level rise. It is likely that the relatively small amount of levee construction in the Ayeyarwady Delta (i.e., compared to the Mekong Delta) contributes to this capacity to retain sediment. Future surveys in the Ayeyarwady Delta over multiple years and in different seasons will narrow the wide estimate presented here and would provide greater clarity about where and when sediment retention occurs.

Despite the sediment retention in the upper delta, these three distributaries were still exporting 0.47–3.3 t/s of sediment to the ocean during high flow (Table 2.1). Fluvial advection dominated the sediment flux export (Figure 2.8), which is consistent with other tropical, tide-dominated deltas (Goodbred and Saito, 2012). The hydrodynamic estuary was pushed to or beyond the river mouth (the seaward limit of the geomorphic estuary), as it is in the Ganges-Brahmaputra, Mekong, Fly and Amazon systems (Barua, 1990; McLachlan et al., 2017; Nittrouer and DeMaster, 1996; Nowacki et al., 2015; Ogston et al., 2008). These ‘leaky’ estuaries trap less sediment because oceanic processes advect sediment off- and/or alongshore.

The low-flow season provided insight into the combined role of estuarine processes and offshore sediment supply in defining conditions within distributaries. The dominant estuarine stratification, classified using the low-flow longitudinal and tidal survey observations (Figure A.S2), was partially mixed. This degree of stratification is common during the low-flow season in

tide-dominated systems, such as the Mekong River (Figure A.S2, McLachlan et al., 2017). The Yangon and Bogale distributaries likely exhibit partially mixed, salt-wedge conditions, and strain-induced period stratification (SIPS) over a full spring-neap tidal cycle. The Pathein distributary likely remains partially mixed due to the weaker discharge velocities, as it is the deepest and widest of the three distributary channels. Bathymetry and tidal range are also known to impact the salt intrusion length scale (MacCready & Banas, 2012). The salt-intrusion limit in the Pathein distributary was roughly double that of the Yangon and Bogale distributaries (Figure 2.6) as a result of the greater cross-sectional area and lesser tidal range.

Despite the similarity in stratification and velocity structure, there was a dramatic seasonal shift in average distributary turbidity. From values at the apex of 0.2–0.4 g/L (Baronas et al., 2020), SSC increased to >1 g/L in the Yangon distributary, remained relatively constant in the Bogale distributary, and decreased slightly in the Pathein distributary (Figure 2.3). In the Yangon distributary, sediment import was driven by estuarine exchange of turbid water from the northeastern Gulf of Mottoma (Figure 2.8). The high turbidity in this region is maintained by strong tidal currents, which are amplified in the Gulf, and the extent of elevated turbidity varies by hundreds of kilometers over spring-neap and seasonal timescales (Ramaswamy et al., 2004). In the Bogale distributary, located near the western limit of this high-turbidity region, the average SSC within the distributary varied significantly between neap and spring tides (Figure 2.7). During the neap tide, greater SSC was primarily associated with local resuspension during peak ebb and flood flows. During spring tide, SSC values were persistently greater despite comparable bed-stress values, suggesting import of turbid ocean water.

In the Pathein distributary, SSC was consistent with high-flow values due to the absence of an offshore sediment pool. The estuary length may have contributed to the relatively low

turbidity as well. While sampling was conducted in the upper estuary of all three distributaries, sediment imported from the ocean is more likely to be deposited over the longer Pathein estuary, resulting in a less-turbid upper estuary. Overall, turbidity within the lower distributaries was significantly altered by offshore sediment availability. This new insight adds further complexity to previous studies, which have emphasized the importance of upstream delivery, local resuspension, and tidal range in controlling estuarine turbidity (Uncles et al., 2002).

Despite this evidence of low-flow offshore sediment import, there was no clear evidence in the data of sediment retention and deposition within the lower distributary channels. The residual sediment fluxes were seaward (Figure 2.8), and the lower-distributaries remained ebb-dominant, both in terms of time and velocity. However, the instantaneous sediment fluxes in the Yangon distributary were an order of magnitude larger than the residual, increasing the error in calculating the residual and the flux decomposition. The overall bed texture did not shift dramatically between seasons (Figure 2.9), unlike the Mekong and Ganges-Brahmaputra Rivers (Allison et al., 2017; Wilson and Goodbred, 2015). However, mud draped over sand observed in the Bogale and Pathein distributaries indicates sediment deposition, and the presence of eroded mud balls also indicates previous compaction of fine sediment deposits. Ephemeral sediment deposition was observed during the tidal surveys, in both seasons and all three distributaries (Figure 2.5 and Figure 2.7), and the significant tidal sediment-flux terms were consistent with cycles of suspension and deposition (Figure 2.8). These observations suggest that sediment imported by tidal pumping is retained in the Yangon and Bogale distributaries.

It is possible that the transitional seasons between high and low flow are periods of increased fine-sediment retention, which could explain why bed sediment changes were not observed with this biannual sampling scheme. During the onset and end of the SW monsoon, the

estuaries would exhibit salt-wedge stratification as river discharge and freshwater Froude number increase and decrease, respectively (Figure A.S2). This increased stratification, combined with the existing estuarine convergent processes and offshore-sediment import, would increase sediment retention by decreasing ebb-tide bed stresses (Burchard et al., 2018). It is also possible that a region of fine-sediment deposition was located upriver of the study areas during low flow. The interface between the tidal river and estuary was found to be a region of increased sediment retention in the Song Hau distributary of the Mekong River (McLachlan et al., 2017). However, the net import of sediment during the low-flow season in the Mekong River was supported by salt-wedge stratification and an associated switch to flood dominance (Nowacki et al., 2015), so a direct comparison between systems is complicated.

In summary, these three distributaries of the Ayeyarwady Delta exhibit significantly different hydrodynamics and sediment dynamics, and observations in one distributary would not be representative of the delta as a whole. During the high-flow, SW monsoon, 20–60% of the sediment flux at the mainstem is retained within the upper delta, while the lower distributaries are largely tidal rivers exporting sediment. During the low-flow, NE monsoon the overall sediment flux decreases, and the lower distributaries are partially mixed estuaries where turbidity is controlled by offshore sediment supply. This marine sediment is likely deposited and resuspended on tidal timescales, but it is unclear where it is retained within the distributary channel beds, tidal flats, or mangrove forests. Further measurements along the distributaries and in different seasons will improve the estimate of total annual sediment retention within the delta.

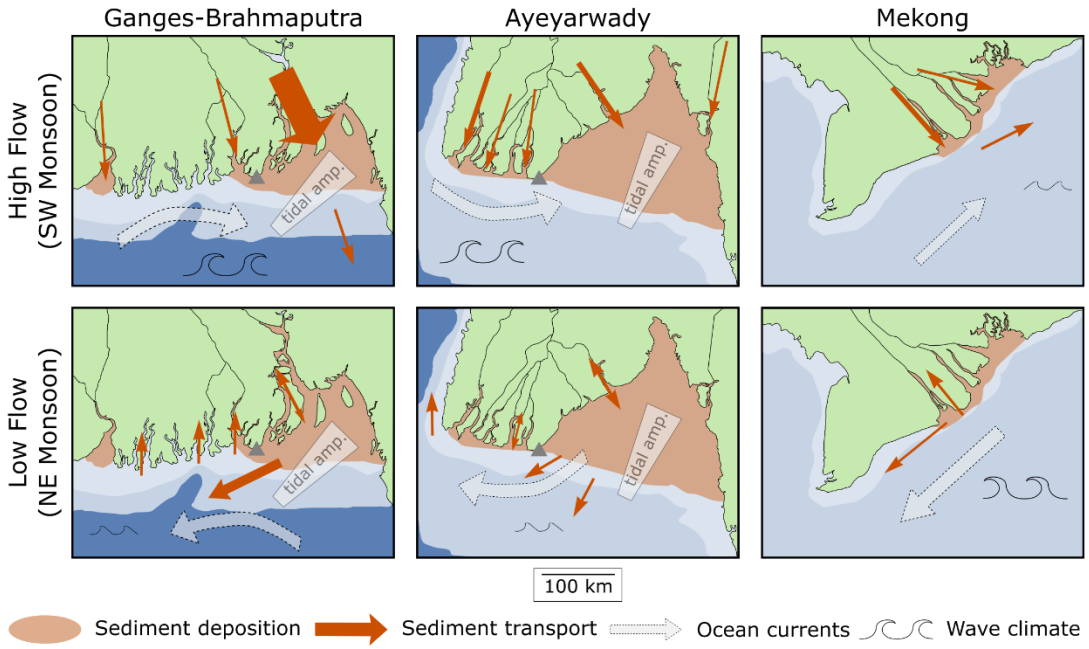

Figure 2.10. Summary of conclusions. Cartoons of ocean conditions and sediment dynamics in the Ganges-Brahmaputra (Wilson & Goodbred, 2015), Ayeyarwady (this study and Kuehl et al., 2019), and Mekong Deltas (Ogston et al., 2017) during the NE and SW monsoon seasons. Prevailing currents are indicated with white arrows and the wave climate is indicated with scaled wave symbols. The orange arrows approximately scale with the magnitude of sediment transport; regions of temporary deposition are shaded brown. The gray triangles indicate the rough delineation between eastern and western delta regions, where applicable.

2.5.2 *Controls on tide-dominated deltas in monsoon environments*

The Ayeyarwady, Ganges-Brahmaputra, and Mekong Deltas are tide-dominated, tropical systems that share similar headwaters and monsoon climates yet exhibit significantly different morphologies (Figure 2.10). Comparing these three, closely related systems eliminates many variables that can impact sediment dynamics (i.e., sediment source, climate, and vegetation), allowing us to examine the interplay between deltaic sediment retention and the orientation of the coastline with respect to the tides and monsoon winds. For this comparison it is important to divide

the Ayeyarwady Delta into eastern and western regions (Figure 2.10), which have different sediment-transport processes and morphologies, as discussed above and in previous studies (Chen et al., 2020). The eastern region includes the Yangon distributary, the western region includes the Pathein distributary, and the Bogale distributary falls near the boundary between regions. The Ganges-Brahmaputra Delta can similarly be divided into distinct eastern and western hydrodynamic regions (Figure 2.10).

During the high-flow, SW monsoon, distributaries are predominantly ebb-dominated, tidal rivers exporting sediment in all of these systems. In the Ganges-Brahmaputra, the estuary is displaced onto the shelf by the ~100,000 m^3/s fluvial discharge (Barua, 1990). In the Song Hau distributary of the Mekong, the salt-intrusion length varies from 3 to 30 km (Nowacki et al., 2015), much like the Bogale distributary. While estuarine processes are forced towards or onto the shelf, the ocean conditions are energetic seaward of the Ganges-Brahmaputra Delta and the western Ayeyarwady Delta (Figure 2.10). Sediment discharged from distributaries is rapidly advected offshore or into a sheltered gulf (Goodbred and Kuehl, 1999; Kuehl et al., 2019; Liu et al., 2020). In the Mekong Delta and the eastern Ayeyarwady Delta, wave conditions are generally quiescent during the high-flow season, and sediment is retained close to the mouths of distributaries (Eidam et al., 2017). However, tidal amplification in the Gulf of Mottoma produces strong currents that continually rework the bed (Kuehl et al., 2019).

During the low-flow, NE monsoon, the lower distributaries transition to partially mixed estuaries. Estuarine tidal pumping can import shelf sediment if it is available (Figure 2.10). In the western Ganges-Brahmaputra and eastern Ayeyarwady Deltas, offshore sediment is remobilized and pumped landward by macrotidal currents despite relatively quiescent ocean conditions. The resulting distributary turbidity varies from 0.2 to >10 g/L. In the Ganges-Brahmaputra, some of

this sediment is stored seasonally in the upper estuary (Barua, 1990) and on the western delta land surfaces (Rogers et al., 2013). Offshore sediment availability and tidal energy decrease westward across the Ayeyarwady Delta, and no estuarine import was observed in the westernmost, Pathein distributary. In contrast, offshore conditions are energetic during low-flow in the Mekong River, and remobilized sediment is transported in- and alongshore by southwestward waves and currents (Eidam et al., 2017). Some of this sediment is retained in the lower distributaries (Nowacki et al., 2015). Unlike both the Ganges-Brahmaputra and Mekong Rivers, it is unclear where the Ayeyarwady distributary channels retain sediment imported during low-flow (Figure 2.9), and this should be an area of focus for future research.

In summary, nearshore sediment transport in monsoon-influenced deltas is strongly controlled by coastal orientation, which impacts the timing of energetic, marine conditions with respect to seasonally varying discharge. Coastal morphology can also amplify tidal currents, which can resuspend and transport sediment throughout the year. Consequently, variability in sediment dynamics between distributaries of a single delta can be comparable to variability between deltas. The element of seasonal timing and coastal orientation is missing from the classic, ternary diagram of delta classification (Galloway, 1975), but should be considered in studies of delta morphology and stability. And, the impact of interannual cycles (e.g. El Niño Southern Oscillation) on these temporal relationships should be considered, as previous studies have demonstrated that significant changes in sediment retention can occur on decadal timescales (e.g., in the Fly River, Ogston et al., 2008). Similar intra- and inter-delta comparisons could provide insights into the evolution of a broad range of monsoonal to temperate, tide-dominated deltas, however, broader comparisons add complicating factors. Temperate deltas can be more strongly influenced by episodic, storm events

(Palinkas, 2009; Wheatcroft, 2000) compared to the more consistent, season-long patterns in monsoon-dominated environments.

2.5.3 *Sediment residence time and impacts of future damming*

The differences in transport pathways described above are important for nearshore sediment residence time. In the eastern region of the Ayeyarwady Delta, sediment is retained close to the distributary mouths where it can be reimported, increasing residence time. In the western portion of the Ayeyarwady Delta, much sediment is transported away from the distributary mouths, decreasing residence time. The difference in residence time is likely on the scale of decades, though a quantitative calculation would require a time series of distributary sediment fluxes (e.g. Ralston & Geyer, 2017).

With these results in mind, caution should be taken when assessing the potential impacts of future damming on the Ayeyarwady River, as there may be significant differences in distributary response. For example, the impacts of a reduction in sediment supply due to damming would likely be observed first in the western region of the delta. This region is vulnerable to erosion due to the lower sediment residence times and strong, seasonal wave action. Some erosion could be mitigated by alongshore transport of sediment from the upper Gulf of Mottoma, as has been seen in the western Ganges-Brahmaputra Delta (Allison and Kepple, 2001). However, it is likely that coastal erosion patterns would be similar to those in the southeastern, wave-exposed Mekong Delta (Anthony et al., 2015).

A reduction in peak discharge due to damming would likely reduce overbank flows, decreasing fine sediment retention in the upper delta and increasing subsidence far from the coast, as has also been observed in the Mekong Delta (Syvitski et al., 2009). In the lower delta, a decrease in peak discharge would decrease the freshwater Froude number without changing the tidal mixing

parameter, extending the seasonal period of salt-wedge stratification, and shifting the Ayeyarwady towards a regime similar to that in the Mekong River (Figure A.S2). This hydrodynamic shift could significantly increase fine-sediment retention in the Yangon distributary, which has the greatest offshore sediment source. In the short-term, this could negatively impact port operations in the city of Yangon, requiring increased dredging. However, recent work has demonstrated the inherent, long-term instability of cannibalizing offshore deposits while decreasing fluvial sediment input (Nienhuis et al., 2020). A system will shift towards erosion as the offshore supply is depleted. Overall, differences in distributary sediment dynamics will result in asymmetric damming impacts in the Ayeyarwady and other megadeltas.

2.6 CONCLUSIONS

The processes and mechanisms responsible for sediment retention within deltas are complicated by interactions between complex morphology and forcing within both tidal distributaries and adjacent coastal regions. *In-situ* measurements of sediment dynamics within tidal distributaries provide insight into these processes and provide fundamental constraints for modeling. A primary goal of this study was to compare hydrodynamics and sediment dynamics in the lower reaches of multiple distributaries in a tide-dominated megadelta. The comparison of three representative distributaries of the Ayeyarwady Delta highlighted the variability in sedimentary processes within a single delta and the importance of considering lateral differences when assessing delta stability. The *in-situ* observations indicate the following.

- The lower reaches of the distributaries transitioned from tidal rivers during high flow to partially mixed estuaries during low flow, as has been observed in many monsoon systems.

- During high flow, 20–60% of sediment carried by the mainstem is retained in the upper delta. This process also results in a fining of the sediment carried in suspension. In the lower reaches of the distributaries, turbidity was controlled by upstream delivery, sediment export scaled with discharge, and fluvial advection dominated the sediment flux.
- During low flow, distributary turbidity was controlled by offshore sediment availability, which decreases westward. The Yangon distributary imported sediment via estuarine exchange, leading to persistent SSC values >1 g/L. Though the residual sediment fluxes remained seaward, layered sand and mud deposits within the distributary channels suggest that sediment retention does occur. Future investigations should focus on the seasonal transitions between high and low flow, as these may be periods of greater sediment retention.

Comparison of these results with previous studies of similar systems offers new insights into sediment retention in tropical, monsoon-dominated systems. Overall, deltaic and nearshore sediment transport, retention, and residence time are controlled by the orientation of the coastline with respect to the seasonal monsoon winds and currents, and by tidal amplification. In systems like the western Ayeyarwady and Ganges-Brahmaputra Deltas, where high flow coincides with energetic ocean conditions, sediment is rapidly advected off- and/or alongshore. In systems like the eastern Ayeyarwady and Mekong Deltas, where high flow coincides with more quiescent ocean conditions, sediment is retained close to distributary mouths. During low flow, sediment can be reimported into distributaries and delivered to land surfaces, if it is available and remobilized by wave or tidal action. Interannual cycles that affect the timing or magnitude of any of these variables can significantly alter deltaic sediment dynamics and cause asymmetric impacts within a delta.

These comparisons also allow us to predict possible futures of the Ayeyarwady Delta. Currently, the delta is retaining fine sediment and maintaining a relatively stable land surface,

likely because there is no mainstem damming and relatively little levee construction. Future damming of the Ayeyarwady River will cause asymmetric impacts. The western delta is more susceptible to rapid erosion with a decrease in sediment supply while the eastern distributaries are more susceptible to infilling with a shift in the timing of discharge. Heavily impacted regions of the Mekong and Ganges-Brahmaputra Deltas provide hints about the grim future of this system if it is subjected to further alteration.

Chapter 3. PATHWAYS FOR SEDIMENT TRANSPORT AND RETENTION IN MEINMAHLA ISLAND, MYANMAR[2]

3.1 INTRODUCTION

Most of the largest deltas in the world are tide dominated with complex distributary networks (Nienhuis et al., 2020). Deltaic, channel-floodplain networks can retain 40–70% of the mainstem sediment load (Glover et al., 2021; Goodbred and Kuehl, 1998; Milliman et al., 1985; Nittrouer et al., 1995), significantly altering budgets of sediment, nutrients, and carbon delivered to the coastal ocean (Hiatt et al., 2018; Nowacki et al., 2019; Styles et al., 2021). Understanding the dynamics and morphology of these sediment-transport pathways is critical for predicting the future stability of densely populated, low-lying megadeltas (Syvitski et al., 2009) and related coastal infrastructure (Gao et al., 2010). Additionally, connecting modern dynamics to resulting, natural morphology is essential for interpreting the stratigraphic record (Gugliotta and Saito, 2019; Tamura et al., 2012; Walsh and Nittrouer, 2009). The Ayeyarwady Delta, Myanmar, is significantly less altered by human infrastructure than comparable, large, tide-dominated systems (e.g. the Ganges-Brahmaputra Delta, Bain et al., 2019). Here, *in-situ* sediment dynamics and morphology are examined in a mid-channel island in the lower Ayeyarwady Delta, providing insights into important sources, sinks, and flux pathways in a megadelta.

It is challenging to collect *in-situ* measurements of sediment transport and morphology over deltaic scales. Consequently, much research has focused on identifying comprehensive

[2] This chapter was submitted to Sedimentology as Glover, H.E., Ogston, A.S., Fricke, A.T., Nittrouer, C.A., Aung, C., Naing, T., Lahr, E.J.. "Pathways for sediment transport and retention in a vegetated, mid-channel island: Connecting sediment dynamics to morphology in Meinmahla Island, Ayeyarwady Delta, Myanmar" on 7 March 2022.

analytical relationships using remote sensing and numerical or analytical models. Geometric relationships have been identified in channel patterns that can help predict changes to delta-lobe stability (Tejedor et al., 2015b, 2015a, 2016), flux partitioning through channels (Meselhe et al., 2021), and stable restoration configurations for dike breaching (Hood, 2016). Other studies have focused on the geometric relationships and exchange between channels and floodplains (Fagherazzi, 2008; Hiatt and Passalacqua, 2015; Passalacqua et al., 2013). These relationships can predict erosion and deposition along channel margins (Nienhuis et al., 2018) and identify morphologically similar regions of deltas (Edmonds et al., 2011; Liang et al., 2016; Passalacqua et al., 2013). By necessity, many of these studies rely on steady-state assumptions and simplifications. *In-situ* observations of natural systems supplement these studies by providing insight into the reliability of simplifying assumptions and identifying the physical processes underlying analytical relationships. The focus of this study, Meinmahla Island, is a relatively unaltered mid-channel island where process can be connected to resulting morphology.

The terminology for channels and island-types is not well defined with respect to physical processes in tide-dominated deltas. For example, island perimeters are often defined based on the locations of channels that are detectable via remote sensing, even though this perimeter may not coincide with the morphologic unit of land that responds dynamically to river flow (Passalacqua et al., 2013). Individual islands are often crosscut by channels and are technically composed of multiple islands. For clarity, terminology is explicitly defined here (Figure 3.1). Distributaries are deltaic channels with a width on the order of the main stem of the river, while tidal channels have significantly smaller widths and connect to distributaries or the ocean. Tidal channels with one entrance (i.e. dead-end) and one tidal forcing are low-connectivity (LC), and channels with multiple entrances are high-connectivity (HC) (McLachlan et al., 2020a). Distributaries are

separated by “inter-distributary land masses”, which are technically islands, but have interior regions that do not directly respond to channel processes. In contrast, distributaries also contain mid-channel islands, which have width scales consistent with that of the distributary flow (Passalacqua et al., 2013). We will refer to the flat, intra- and supra-tidal regions of these islands as “land surfaces” because these regions have permanent dwellings and are not submerged by all high tides. This study focuses on morphology and flux through tidal channels of a relatively undisturbed, mid-channel island that is densely vegetated by mangroves.

Sediment dynamics have been well studied in a variety of mangrove-forest environments. Early studies in mangrove forests focused on low-connectivity tidal channels and the adjacent floodplains (e.g., Aucan and Ridd, 2000; Mazda *et al*., 1997; Wolanski *et al.*, 1990). Within the channel, flow is generally oriented along-channel and can be described by the balance between the tidal pressure gradient and bed friction. Once water elevation exceeds the bank height, flow on the flats tends to be oriented perpendicular to the channel, and velocity is rapidly attenuated by emergent vegetation (Horstman et al., 2013a). Sediment and flocs entrained in the turbulent in-flow settle during slack water of high tide, and form cohesive mud deposits (Furukawa et al., 1997). Flow in high-connectivity channels of mangrove forests can be more complicated; asynchronous tidal propagation can result in sediment pumping along channel in addition to sediment delivery to intertidal surfaces (McLachlan et al., 2020a). Groundwater flow can also substantially alter fluxes of water, salt, and other dissolved constituents (Alongi, 2014; Bouillon et al., 2007; Cameron et al., 2021; Susilo et al., 2005).

The goal of this investigation is to connect modern fluxes to evolving morphology in a relatively natural, mangrove system. The study is guided by two questions:

1. What are the tidal and seasonal pathways and mechanisms for sediment transport in a mangrove-forested, mid-channel island of a distributary? What are the relative roles of low-connectivity and high-connectivity tidal channels, and how is transport influenced by sub-surface flow?
2. What does this process-based investigation tell us about the geometry, evolution, and mobility of delta channel networks and mid-channel islands over decadal timescales?

Addressing these questions will provide broad insights into how tide-dominated deltas prograde and aggrade under natural conditions.

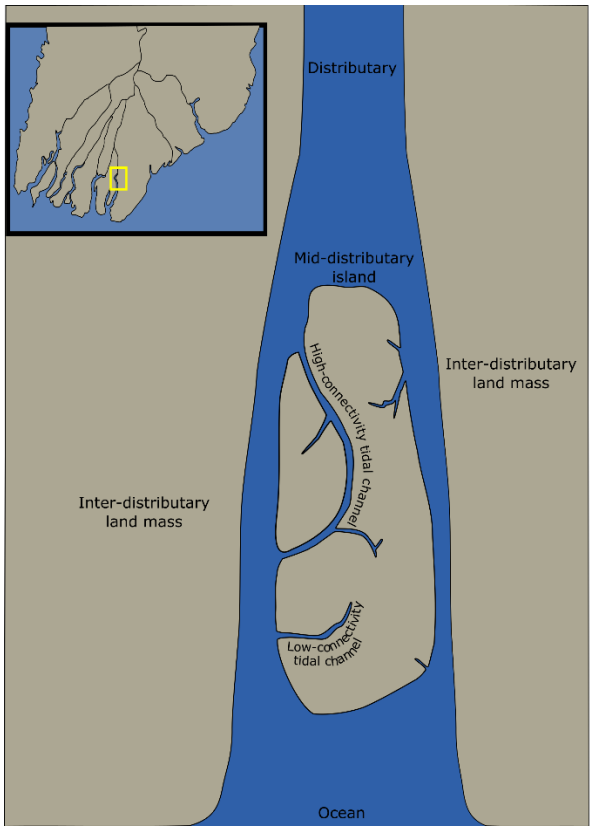

Figure 3.1. Cartoon representation of a tide-dominated delta with the relevant morphologic features labelled.

3.2 Study Site: Meinmahla Island in the Ayeyarwady Delta

The Ayeyarwady River drains from the Himalayan Syntaxis through the Central Myanmar Basin to form a ~250-km-wide delta in the Gulf of Mottoma, on the eastern side of the Bay of Bengal (Figure 3.2). The mainstem of the river is currently undammed and carries the third largest sediment load globally (Chen et al., 2020), with $379\pm9\times10^9$ m^3 of water and 326±91 Mt of sediment (Baronas et al., 2020). Within the tide-dominated delta, the river splits into multiple, interconnected distributaries.

Meinmahla Island (Kyun) is a Ramsar mangrove and crocodile preserve (Ramsar site 2280, https://www.ramsar.org/) located in the central, Bogale distributary (Figure 3.2). Meinmahla Island has remained relatively unaltered while the surrounding region has been deforested and converted to agricultural fields over the past 80 years (Webb et al., 2014). The forest on the island is composed of a dense mixture of mangroves, predominantly *Avicennia marina* and *Heritiera fomes*, and mangrove associates, such as *Nypa fruticans*, with a typical canopy height of ~4 m (Win et al., 2019). The island is fronted by a shoal, and the seaward coastline has prograded seaward by ~800 m over the past 50 years (Chen et al., 2020). A dendritic network of tidal channels cuts through the island, with channel widths ranging from <1 m to ~400 m.

Seasonal conditions in the delta are controlled by the monsoonal weather patterns (Rodolfo, 1969). From May to October the southwest (SW) monsoon brings moist winds from the southwest, delivering the majority of precipitation as well as energetic wind waves and eastward-directed currents in the Gulf of Mottoma (Kuehl et al., 2019). During the northeast (NE) monsoon, warm winds from the northeast bring dry weather and westward-directed currents in the Gulf. These seasons produce significant shifts in hydrodynamic conditions within the distributaries of the delta. During the SW monsoon (high-flow) season, the distributaries are predominantly tidal rivers

exporting sediment. In contrast, during the NE monsoon (low-flow) season the distributaries are estuarine and can reimport reworked marine sediment (Glover et al., 2021).

The modern Ayeyarwady Delta retains 20–60% of the mainstem sediment load (Glover et al., 2021). The coastline prograded rapidly to its current extent over the past ~8 kyr (Giosan et al., 2018) and has likely reached an equilibrium at the southern end of the Indo-Burman Range (Hedley et al., 2010; Kuehl et al., 2019). There are no published estimates of relative sea level change in Myanmar, but rates likely vary across the delta due to the Sagaing Fault (Vigny et al., 2003) and anthropogenic activities such as fluid extraction. Currently, the western coastline is dominated by erosion and seasonal reworking by storms, while the eastern coastline is dominated by muddy deposition and reworking by macrotidal currents (Anthony et al., 2019). Meinmahla Island is located in the transition zone between these eastern and western zones.

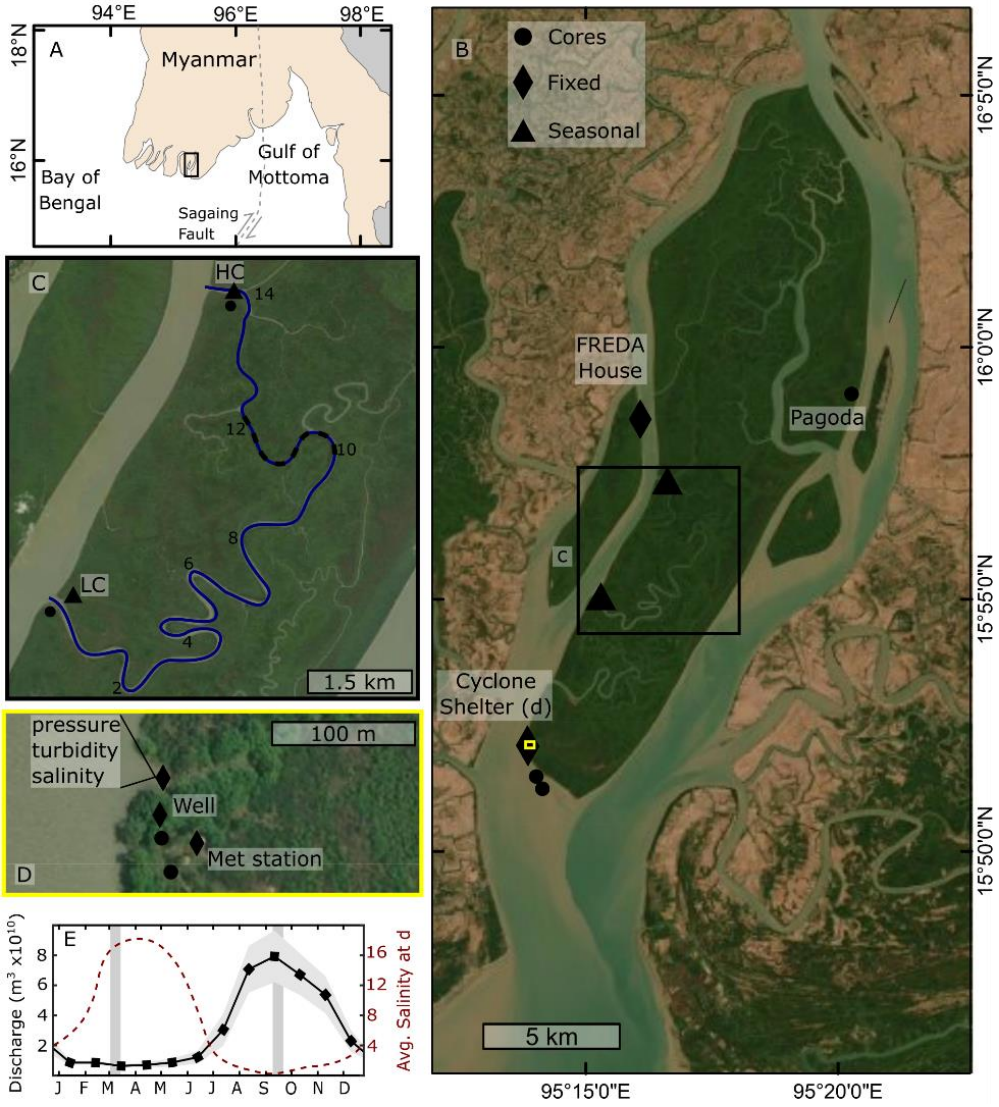

Figure 3.2. The regional map of Myanmar a) with the extent of b) outlined in black. An aerial image b) of Meinmahla Island, accessed through ESRI ArcMap. The remaining mangrove forest shows as dark green and agricultural lands show as brown. The fixed instruments are marked with black diamonds, seasonal instruments with black triangles, and sediment cores with black circles (see Table 3.1 for instrument details), and the extents of insets c) and d) are indicated with boxes. The instrument locations are provided in c) and d), and high-connectivity (HC) channel is highlighted in blue with distance from the southern entrance indicated in km. A shallow region in the channel is emphasized with a black, dashed line. The e) total discharge for the Ayeyarwady River is shown in black with a gray shadow showing +/- 1 standard deviation (Furuichi et al., 2009), the average salinity at the cyclone shelter is show in red dashed line (Glover et al., 2021), and the sampling seasons are shown with dark-gray vertical bars.

Table 3.1. Instrument location, details, deployment dates, and sampling rates from Meinmahla Island in 2017–2019 (see Figure 3.2 for map).

Location	Instrumentation and meters-above-bed (mab) elevation	Deployment Dates	Burst Interval and Duration
Cyclone Shelter: Roof	Onset Weather at 6.5 mab	2/24/2017–9/28/2019	10 min
Cyclone Shelter: Well	Onset Hobo Pressure at -0.2 mab	2/24/2017–9/11/2017	10 min
Cyclone Shelter: Dock	Onset Hobo Pressure, Onset Hobo Conductivity, and RBR Solo turbidity at 0.1 mab	2/24/2017–9/28/2019	10 min
FREDA House: Dock	Onset Hobo Pressure and RBR Solo turbidity at 0.1 mab	9/13/2017–9/27/2019	10 min
High Connectivity	Nortek Aquadopp at 0.1 mab with 0.1 m bins; OBSs at 0.15 and 0.3 mab;	9/10/2017–9/13/2017 3/6/2018–3/8/2018	1 min for 30 s at 1 Hz
	Onset Hobo Conductivity at 0.1 mab*	9/28/2019–9/30/2019	30 s
Low Connectivity	Nortek Aquadopp at 0.1 mab with 0.1 m bins; OBSs at 0.15 and 0.3 mab;	9/10/2017–9/13/2017 3/4/2018–3/8/2018	1 min for 30 s at 1 Hz
	Onset Hobo Conductivity at 0.1 mab	9/28/2019–9/30/2019	30 s

*This conductivity sensor was not deployed in September 2017.

3.3 METHODS

3.3.1 *Field data*

Seasonality was characterized by recording meteorological conditions and water properties semi-continuously from January 2017 to September 2019 on Meinmahla Island (Figure 3.2). An Onset weather station was deployed ~6.8 m above the ground, higher than the tree canopy, to measure atmospheric pressure, temperature, humidity, solar irradiance, wind speed and direction, and rainfall. Onset Hobo pressure sensors and RBR Solo turbidity sensors were deployed to measure water level and suspended-sediment concentration at two sites in the mainstem of the Bogale distributary (Figure 3.2). An Onset conductivity sensor was also deployed at the seaward site to measure salinity. The groundwater level was measured with an Onset Hobo pressure sensor suspended in a 40-cm-deep, open-ended and perforated PVC pipe set into the ground (Figure 3.2).

During field campaigns in the low-flow (March 2018) and high-flow (September 2017 and 2019) seasons, the turbidity, salinity, and water velocity (Table 3.1) were measured in a high-connectivity and low-connectivity tidal channel of the island (Figure 3.2). The instruments were deployed within the same drainage network, at sites that were accessible via canoe. At each location, an upward-facing Aquadopp current profiler was deployed with two integrated optical backscatter sensors (OBS) to measure turbidity for 3–4 tidal cycles during the transition between spring and neap tides. CTD profiles were collected every 2 km along the length of the high-connectivity channel during each field season using an RBR Concerto with integrated OBS, sampling at 6 Hz. A bed-sediment sample was collected at each CTD site using a Van Veen grab sampler. These surveys took ~2 hours to complete and were conducted while the Aquadopps were deployed. The water velocity was also recorded during the March 2018 campaign using a vessel-mounted 600-kHz Acoustic Doppler Current Profiler.

Sediment cores were collected throughout Meinmahla Island with a 3-cm-diameter, 1.5-m-long auger for grain size and geochronology. Coring sites were primarily located along the shoals or within 5 m of the forest edge due to the impenetrability of the dense mangrove forest. A shore-perpendicular transect of cores was gathered along the 800-m-long trail to Myauk Tayar Pagoda; these coring sites were as far from the path as possible to avoid anthropogenic disturbance. All cores were subsampled in the field at 2–5 cm increments.

During the September 2019 campaign, the locations and approximate sizes of secondary channels were estimated along the exterior shoreline of Meinmahla Island and along the length of the high-connectivity channel. The frequency distribution of secondary channels was assessed as a way to evaluate morphologic age and degree of development (Van Maanen et al., 2015; McLachlan et al., 2020b).

3.3.2 *Laboratory analyses*

All of the OBS and RBR Solo turbidity responses were converted to suspended-sediment concentration (SSC) with a laboratory calibration using known concentrations of sediment collected at the deployment sites (r^2= 0.80–0.91). The SSC was calculated by filtering ~0.1 L of water through pre-weighed, 0.45-µm nitrocellulose membrane filters. Grain size of core and grab samples was measured using a LS13- 320 Particle Size Analyzer. Samples were disaggregated by sonicating in a 0.05% sodium metaphosphate solution prior to being run through the analyzer.

The sediment accumulation rates were calculated using ^{210}Pb geochronology on the subsampled, 1-m cores. The naturally occurring ^{210}Pb isotope can be used to calculate century-scale accumulation rates owing to its 22.3-y half-life (Nittrouer et al., 1979). The excess ^{210}Pb activity of each sample was determined with alpha spectroscopy by measuring the activity of the granddaughter ^{210}Po relative to a known ^{209}Po spike. Samples were digested in acid and isotopes plated onto silver planchets for analysis. The total activity was normalized by mud fraction (<64 µm) to account for variability due to grain size. The supported activity was determined to be 0.7 dpm/g based on the average activity of the deepest samples, and this value was subtracted from all samples to obtain the excess activity. For cores exhibiting an interval of log-linear decay with depth (log-layer), the accumulation rate, *S*, in cm/y was determined from:

$$S = \lambda \Delta z \Big/ \ln\left(\frac{A_0}{A_z}\right) \tag{3.1}$$

where A_0 is the activity at the top of the log-layer and A_z is the activity at the bottom of the log layer, z is depth in core, Δz is the depth between A_0 and A_z, and λ is the decay constant of ^{210}Pb, 0.0311 y^{-1}. The accumulation rate was only calculated when the log-linear R^2 fit was >0.65.

3.3.3 *Data processing*

The Aquadopp water-velocity data were cleaned to remove periods of bad data due to low water, instrument movement, or instrument tilt. Unfortunately, the instruments were often moved by the strongest water velocities, limiting data quality during these time periods. The velocity was rotated to a channel-oriented reference frame: positive velocities are landward/inward and negative velocities are seaward/outward. The instantaneous and net sediment fluxes were calculated per 1-m unit width from the velocity profiles and the depth-averaged SSC.

The underway water velocities and CTD data were cleaned following the method in Chapter 2. Missing surface values were filled with nearest neighbors, and the shape of the near-bed velocity profile was preserved by extrapolating missing values using cubic-spline interpolation and a no-slip assumption. The water density was calculated from the temperature, salinity, and depth measurements using Gibbs Seawater (GSW) Oceanographic Toolbox in Matlab (McDougall and Barker, 2011). The stability of the water column was assessed using the gradient Richardson number:

$$Ri = N^2 / \left(\frac{dU}{dz}\right)^2 \qquad N^2 = -\frac{g}{\rho_0}\frac{d\sigma}{dz} \tag{3.2}$$

where g is the gravitational constant (9.8 m/s^2), $\sigma = \rho - 1000$ kg/m^3, ρ_0 is the background density (1010 kg/m^3), U is the water speed, and z is depth in the water. A value greater than ¼ indicates that the water column is stable while a value less than ¼ indicates that overturning and mixing is possible. The Richardson number was not calculated for the interpolated velocity bins near the bed and surface.

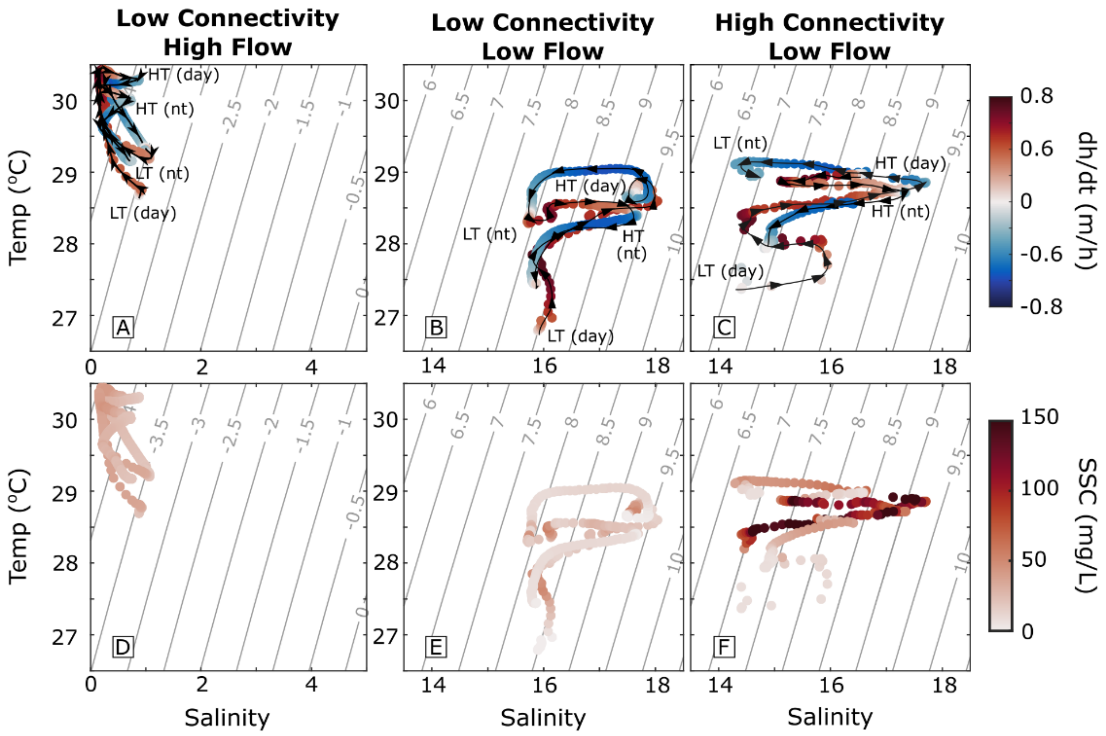

Figure 3.3. Temperature-salinity-density diagrams for the fixed-instruments in the low-connectivity (a,b,d,e) and high-connectivity (c,f) channels during high-flow (a,d) and low-flow (b,c,e,f). Data points are colored by tidal stage in the top row and by SSC in the bottom row. The progression of the tide is shown in the top row, and the high tide (HT) and low tide (LT) for night (nt) and day (day) are labelled. Note the change of salinity scale between seasons.

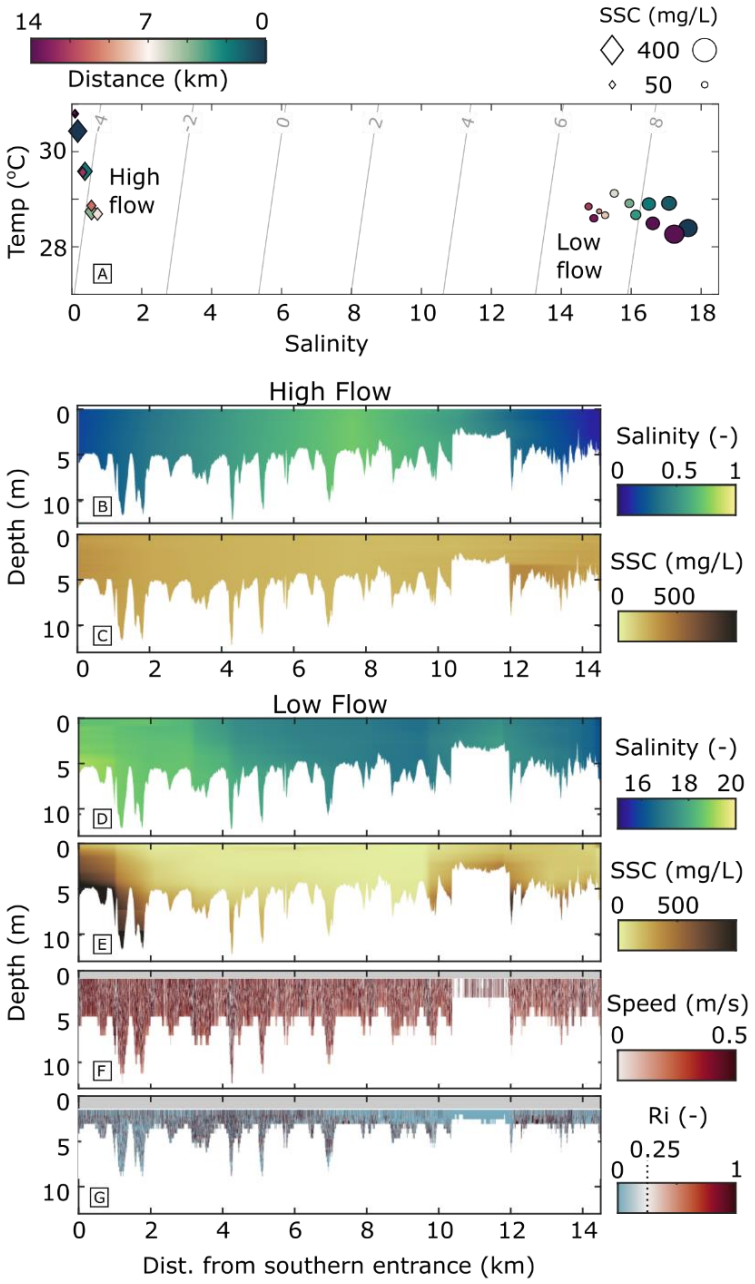

Figure 3.4. Hydrodynamic conditions in the HC channel during high and low flow. Temperature-salinity-density diagram a) from the average CTD profiles colored by distance along the HC channel during high flow (diamonds) and low flow (circles) and scaled by the average SSC. Transects of salinity (b,d), SSC (c,e), water speed (f), and Richardson number (g) along the HC channel during high flow (a,b) and low flow (c-f). All transects were conducted during a flooding tide. The x-axis shows distance along the channel from the southern entrance (see Figure 3.2 for route). Areas with missing data and regions where the Richardson number was not calculated are shaded gray. Note the change in salinity scale between seasons.

3.4 RESULTS

3.4.1 *Hydrodynamics of the high- and low-connectivity channels*

The hydrodynamics of the HC and LC channels were evaluated by comparing the characteristics of the water masses over each tidal cycle at the Aquadopp deployment sites (Figure 3.3). In both locations during low flow the salinity was greater on the flood (~18) than the ebb (~15) and changed abruptly at the transition to low or high tide. There was also a daily temperature signal, with cooler water during the mornings and warmer water in the afternoons and evenings. Consequently, there were unique water-mass characteristics for each tidal stage over the course of a day, with density varying from 1006.5–1009.5 kg/m^3. Overall, the LC channel was consistently colder and saltier while the HC channel had a wider range of values.

During high flow, only the temperature-salinity (TS) diagram for the LC channel is displayed (Figure 3.3) as the HC channel was continuously fresh. The salinity range was 0–1 in the LC channel. The water was colder and saltier during low tide and transitioned linearly to warmer, fresh conditions during high tide. The water was warmer overall during high flow, and the density varied over a smaller range from 995.5–996.5 kg/m^3.

The turbidity trends in the LC channel were similar between seasons despite the differences in water characteristics. The SSC increased with the flooding tide and was consistently low during the ebbing tide (Figure 3.3). In the HC channel, the SSC was more variable from tide to tide, though it was generally greater during the high tide than the low tide.

The characteristics of the water masses along the HC channel were evaluated using the depth-averaged CTD profile data from the high- and low-flow longitudinal surveys (Figure 3.4). These measurements were not synoptic, though both surveys were completed during a flooding tide. The water masses observed along the channel had the same range of temperature and salinity

values as those observed at the Aquadopp site. However, the along-channel trends were not monotonic during either season. Instead, there was a distinct water mass in the island interior (~7 km from either mouth). During low flow, the water in the island center was warmer, fresher, and less turbid and gradually mixed with the colder, saltier, more turbid river water at each entrance. During high flow the water in the island center was colder and somewhat saltier and gradually mixed with the warmer, fresher river water. The turbidity decreased from south to north.

These longitudinal trends in temperature, salinity, and turbidity were further evaluated by examining vertical variability in the HC channel during a flood tide (Figure 3.4). During high flow, the water was mostly fresh and well-mixed through the water column. The salinity increased into the island interior, reaching the maximum value of ~1 around 7 km. The SSC was mostly vertically uniform and decreased slightly in the island interior. There was a region of greater turbidity near the bed at the northern entrance.

During low flow, the water velocity was measured, and the gradient Richardson number was calculated. The velocity was relatively uniform vertically and decreased from ~0.7 to ~0.3 m/s from south to north. At each entrance there was an estuarine structure, with greater near-bed salinity concentrations and partial stratification from 3–5 km and 11–13 km. These stratified regions were predominantly stable with gradient Richardson numbers >0.25. The middle reach was relatively well mixed, with lower salinity (~16) and the Richardson number was high enough to indicate that mixing across the water column was not inhibited by stratification. The SSC followed the same pattern as the salinity, with maximum values near the bed at the southern entrance and well-mixed lesser values in the middle reach. In the shallow reach from 10.5 to 12 km, there was also greater SSC near the bed.

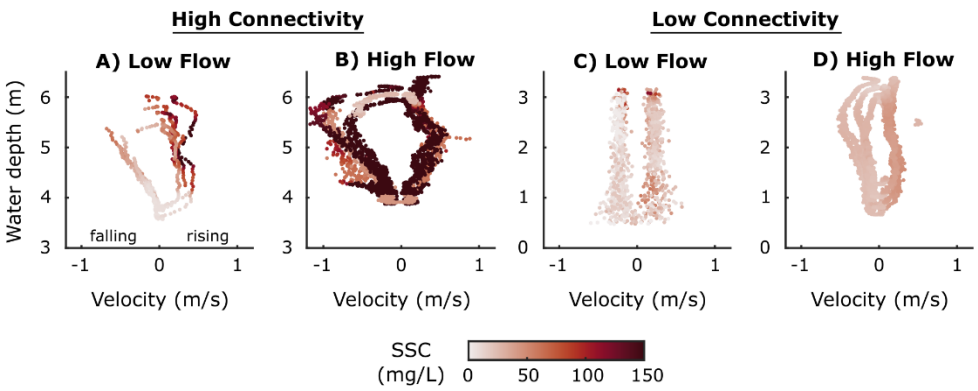

Figure 3.5. Velocity-stage-SSC diagrams for the high-connectivity (a-b) and low-connectivity (c-d) channels during high-flow (a,c) and low-flow (b,d). Negative velocity indicates riverward (ebbing) flow and positive velocity indicates island-ward (flooding) flow.

Table 3.2. Summary of water and sediment fluxes in the HC and LC channels (see Figure 3.2 for locations). The September deployments are during high flow and the March deployments are during low flow. The standard deviation is provided in parentheses. Published values for the mainstem of the Bogale distributary are provided as a reference for flux magnitude (Glover et al., 2021). The percent flux values for water and sediment in the LC channel are scaled to represent all exterior, LC channels in Meinmahla Island.

		Water					Sediment				
Deployment		BR Net Water Flux in Sept or Mar (m^3/s)	Ebb flux (m3/s/m)	Flood flux (m3/s/m)	Ebb as % of BR Net Flux (total HC or all ext. LC)	Flood as % of BR Net Flux (total HC or all ext. LC)	Bogale Net Sediment Flux in Sept or Mar (kg/s)	Ebb flux (kg/m/s)	Flood flux (kg/m/s)	Residual (kg/m/s)	Residual as % of BR Net Flux (total HC or all ext. LC)
HC	Sep 2017	1960	1.3 (0.47)	1.1 (0.10)	3.6	2.8	700	0.22 (0.1)	0.20 (0.07)	-0.02 (0.1)	0.14
	Mar 2018	410	0.60 (0.13)	0.57 (0.17)	7.3	7.0	120	0.02 (0.01)	0.06 (0.03)	0.03 (0.01)	1.4
	Sep 2019	1960	1.1 (0.13)	1.2 (0.21)	2.6	3.1	700	0.11 (0.05)	0.15 (0.05)	0.04 (0.08)	0.3
LC	Sep 2017	1960	0.24 (0.07)	0.21 (0.04)	8.2	7.1	700	0.006 (0.001)	0.007 (0.001)	0.001 (0.0004)	0.14
	Mar 2018	410	0.26 (0.02)	0.26 (0.04)	42.0	42.0	120	0.004 (0.0002)	0.007 (0.001)	0.003 (0.001)	1.5
	Sep 2019	1960	0.14 (0.008)	0.15 (0.03)	4.8	5.1	700	0.043 (0.003)	0.05 (0.001)	0.004 (0.0009)	0.42

3.4.2 *Velocity-stage-SSC and net flux in high- and low-connectivity channels*

Velocity-stage-SSC diagrams provide insight into the relationships between sediment fluxes and tides. The tidal range during all of the measurements was ~2.2 m, as the instruments were always deployed during the transition from spring to neap tides. In the HC channel the tidal velocity pattern was similar during high and low flow (Figure 3.5). The water velocity was greater during ebb than flood tide. During high flow, the maximum water velocity, ~1.2 m/s, occurred during the onset of the falling tide (Figure 3.5). Unfortunately, this tidal stage is missing from the low-flow deployment because the instrument moved. The SSC changed seasonally and did not follow the same patterns as velocity. During low flow, the SSC was greater during the flooding tide, but during high flow, there were periods of increased turbidity throughout the tidal cycle. The LC channel velocity was more symmetric during rising and falling tides, with slight maxima of 0.35 m/s during the onset of each tidal change (Figure 3.5). The greatest velocity occurred during a high-flow ebb tide, likely due to the greater floodplain inundation depth and subsequent water flux during the wet season. However, the SSC was greater on the flooding tide during both seasons, resulting in consistent landward sediment flux (Table 3.2).

The water and sediment fluxes were calculated per meter width for the HC and LC channels. In the HC channel, the average flood and ebb water fluxes were similar, at ~1.1 m^3/s/m during high flow and ~0.6 m^3/s/m during low flow. The residual sediment flux in the HC channel was on the order of 0.02 kg/m/s and switched sign (direction) between deployments. The LC channel individually carried an order of magnitude less water and sediment than the HC channel. However, the LC channels consistently imported sediment at a rate of 0.001–0.004 kg/m/s, and there was no significant difference in sediment flux seasonally.

3.4.3 *Groundwater in Meinmahla Island*

The groundwater flow was assessed by comparing the depth and temperature (Figure 3.6) in the well record to the values measured at the adjacent dock (see Figure 3.2 for instrument locations). The elevation of the water table changed seasonally, over spring-neap cycles and over individual tides. During low-flow spring tides, the flats were inundated by high tides, and the well filled with water so that the water level matched that in the river (Figure 3.6). During spring low tides, the water level only dropped to ~0.4 m indicating that the soil remained saturated. However, during neap tides the land surface was not inundated and the water table gradually dropped below the level of the instrument. This groundwater was recharged during the onset of the next spring tide until it was ≥0.4 m again. During high flow, the water level in the river was higher on average. The land surface was inundated over every tide, and the water level in the well never dropped below 0.4 m (Figure 3.6). The bed sediment around the well was predominantly muddy; grain size is discussed in greater detail in Section 4.4.

The temperature in the well did not vary significantly over seasonal or tidal timescales, remaining ~27° C. In the distributary, the water temperature did vary significantly. The average temperature in the river during low flow, 31° C, was greater than that during high flow, 27° C, and the temperature varied more during low flow than during high flow.

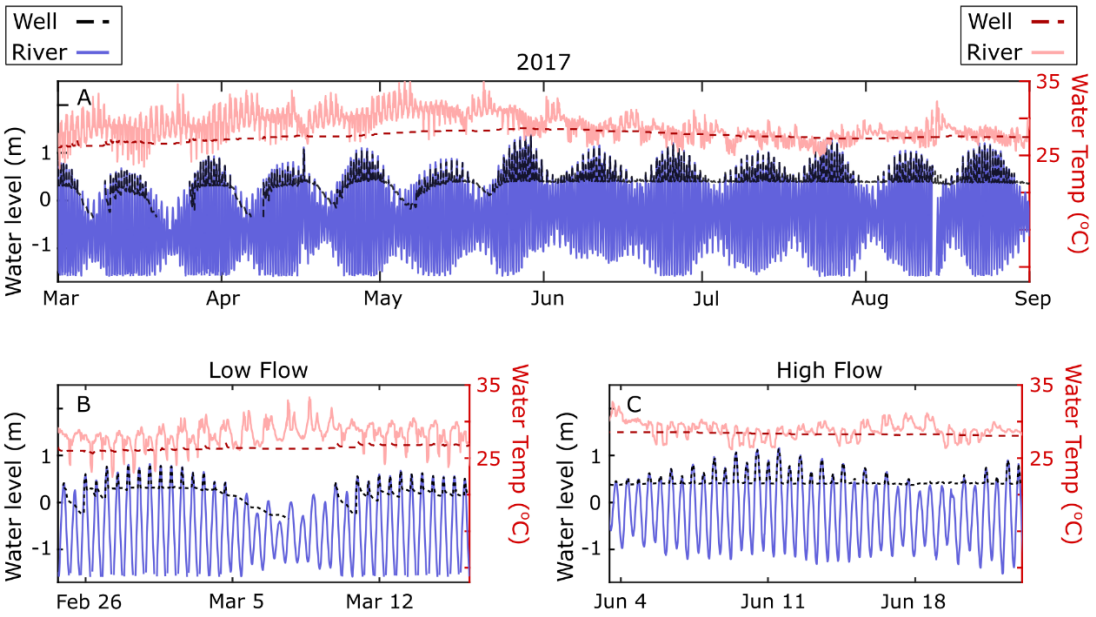

Figure 3.6. Water depth and temperature during 2017 in the well (dashed lines) and the Bogale distributary (solid lines). See Figure 3.2 for the instrument locations. The full record is shown in a) with three-week periods from low and high flow shown in b) and c), respectively. The temperature sensor in the well may have been affected by biofouling, limiting the sensitivity of the signal.

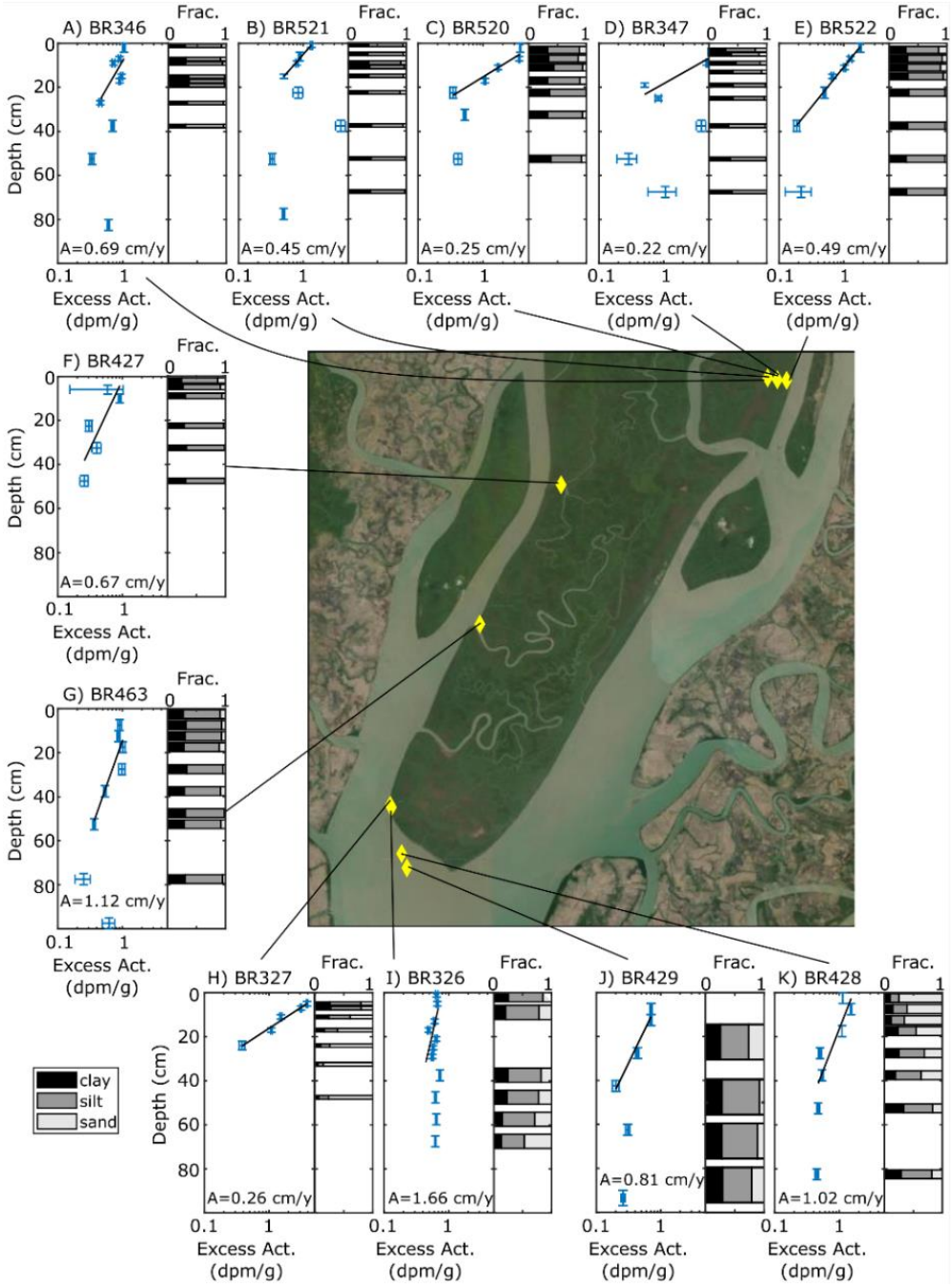

Figure 3.7. Excess ^{210}Pb activity and clay/silt/sand fraction for depth intervals in cores collected throughout Meinmahla Island. The core locations are labelled on the map. The calculated accumulation rate is included on each plot.

3.4.4 *Island morphology from sediment cores, channel surveys, and aerial imagery*

Cores were collected on the prograding shoal at the seaward end of the island, at the mouths of channels along the west side of the island, and along a shore-perpendicular transect on the east side of the island (Figure 3.7) to examine sediment accumulation in a variety of environments. The cores on the prograding shoal had the greatest accumulation rates, at 0.79–1.64 cm/y over the upper 50 cm (Figure 3.7). These shoal cores were the least bioturbated, and mm-to-cm-scale laminations were observed in x-radiograph negatives of cores.

All of the cores collected from the island had excess ^{210}Pb at 80–100 cm depth. The cores collected on the western side of the island were extensively bioturbated. Data from many cores did not exhibit the clear zone of log-linear ^{210}Pb decay that would indicate steady-state accumulation, and these cores were not used to calculate accumulation rates. The apparent accumulation rates in cores with a log-linear region were 0.85–3.1 cm/y. The cores collected along the eastern, shore-perpendicular transect were more consistent, with distinct log-linear layers and accumulation rates of 0.25–0.58 cm/y. There was also a distinct maximum in ^{210}Pb activity at ~40 cm in 3 of the 5 cores along the transect. The grain size of sediment in all the cores was consistently 30–40% clay and 40–70% silt (Figure 3.7). Many cores had a 10–20% sand fraction in the upper 10 cm. There were no clear spatial trends in grain size.

The size and spacing of LC channels were recorded along the shoreline from the cyclone-shelter dock to the southern entrance of the HC channel (Figure 3.2). There were ~6 channels per km that were 2–5 m wide, and there was no significant pattern to the channel distribution (data not included in Figure 3.8). However, the channel survey along the length of the HC channel revealed variation in the island interior (Figure 3.8). There was a distinct cluster of small (<5 m wide), secondary channels from 9 to 12 km along the HC channel (highlighted in Figure 3.2), and the

largest channels were generally close to the mouths. The bed of the HC channel was mostly soft, brown mud (D_{50}=5–10 µm, 30% clay, 55% silt) during both high and low flow. However, the bed from 9 to 12 km was ~90% fine sand.

The planform evolution of the HC channel was evaluated using aerial imagery collected starting in the 1960s (Figure 3.9). The southern portion of the channel remained remarkably stable and sinuous over the entire record, with persistent, tight bends. However, the channel only connected to the modern, northern mouth in the 1960s. The initially narrow connection gradually widened to its present size by the 1980s. Over the same time period, the reach from 9 to 12 km became narrower and the new banks were rapidly colonized by mangrove vegetation. Additionally, many of the dendritic channel networks draining into this channel reach disappeared, either due to infilling with sediment or coverage by vegetation.

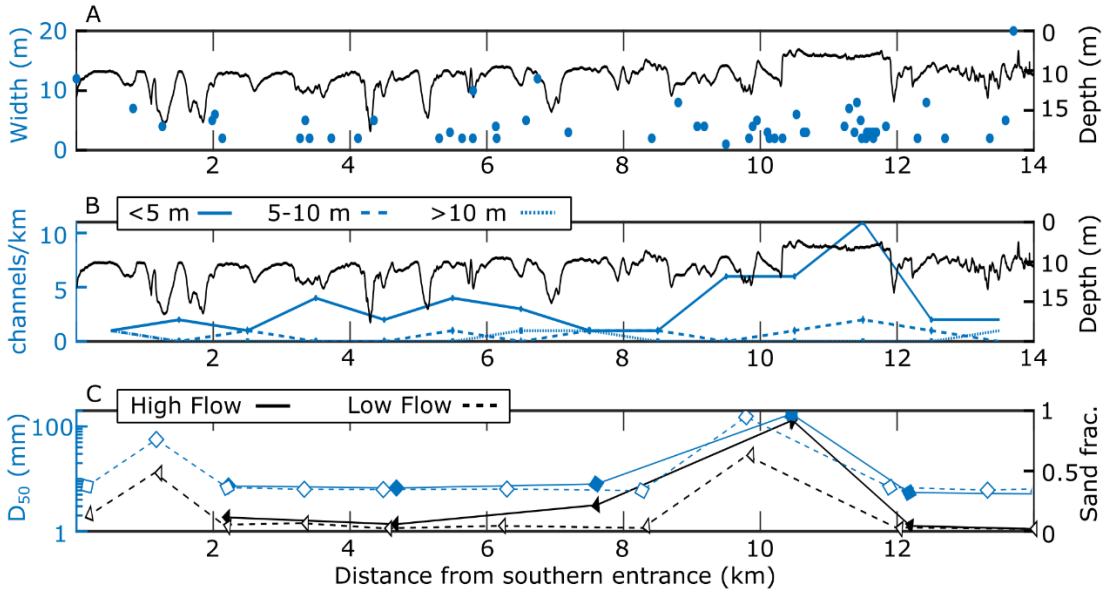

Figure 3.8. Survey of secondary channel widths with main-channel depth (a,b) and bed grain size (c) along the HC channel (see Figure 3.2 for route). Both the a) raw channel sizes and locations and the b) channel density for each size class is shown in blue. The measured depth may not always

capture the true thalweg. The c) median grain size (blue) and sand fraction (black) are shown for high flow (solid lines) and low flow (dashed lines).

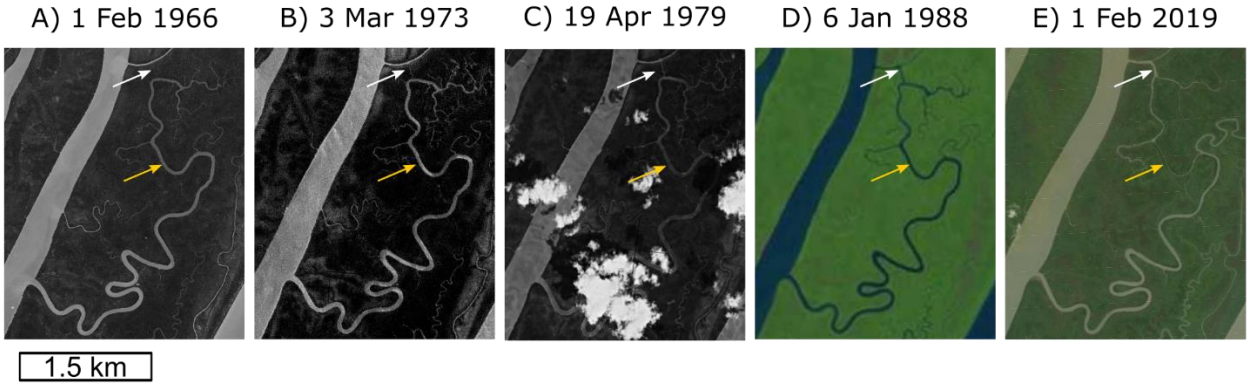

Figure 3.9. Aerial images of the HC channel in Meinmahla Island from 1966–2019 (accessed through USGS Earth Explorer, August 2021). The region that is widening is highlighted with a white arrow and the region that is narrowing is highlighted with a yellow arrow.

3.5 DISCUSSION

The goal for this investigation of Meinmahla Island is to identify the physical processes controlling water and sediment fluxes through a mid-channel island of a distributary and relate these processes to morphology. Sediment dynamics in and around Meinmahla Island is influenced by the encompassing dynamics of the Bogale distributary and its interactions with the Gulf of Mottoma, which vary tidally and seasonally. During high flow, the lower Bogale distributary is predominantly a fresh, tidal river with uniform SSC (~0.25 g/L), and during low flow, the seaward reach of the distributary is a partially mixed estuary with turbid water (>1 g/L) imported from the Gulf of Mottoma by spring tides (Glover et al., 2021). The *in-situ* data presented here reinforce that mid-channel islands are traps for suspended material with multiple, distinct and dynamically adjusting transport pathways. The following discussion examines transport via low- and high-connectivity channels, considers the role of groundwater flow, and connects sediment dynamics

to deposition and accumulation. These observed processes are then related to broader delta channel-network metrics and predictions of deltaic stability.

3.5.1 *Hydrodynamics and sediment transport in low-connectivity tidal channels*

Exterior, low-connectivity tidal channels provide a direct route for persistent, tidal exchange of distributary water and sediment with island surfaces. The instrumented LC channel fluxed 2.6–7.3% of the Bogale water discharge during each flood or ebb tide (Table 3.2). During high flow, colder, marine-influenced water was imported, and warmer, fresher water was exported (Figure 3.3). During low flow, the water temperature followed the same pattern of daily warming, and there were abrupt shifts in salinity and density, indicative of minimal mixing during flood and ebb tide. Overall, the water density and turbidity were strongly controlled by residence times on the flats where the water was warmed while sediment settled. Meinmahla Island, with its extensive flats, appears to be a source of heat to the lower Bogale distributary. Meinmahla Island, with its extensive flats, appears to be a source of heat to the lower Bogale distributary, which could impact sediment transport. In purely freshwater Amazonian tidal channels, thermal gradients have been shown to advect sediment (Nowacki et al., 2019), and barrier islands have been shown to impact estuarine circulation and transport (Deignan-Schmidt et al., 2021; Guo et al., 2020). However, it is unclear from the present dataset whether heat exchange in these estuarine tidal channels influences density enough to impact sediment transport.

While the island is a source of heat it is also a sink for sediment. During both seasons, the greater flood-tide SSC resulted in a net import of sediment (Table 3.2), despite ebb-dominant duration and velocity (Figure 3.5, Table B.S1). This sediment import is consistent with many studies of low-connectivity channels in mangrove forests (Furukawa and Wolanski, 1996;

Horstman et al., 2013a; Mazda et al., 1995; McLachlan et al., 2020a; Santen et al., 2007; Wolanski et al., 1980). Sediment retention is promoted by the high-friction vegetation and cohesive deposits.

Though this net sediment influx was constant between seasons, the sediment sources likely change through the year. During high flow, sediment is primarily sourced from upriver. The average SSC was consequently lower, however, there was greater potential for sediment deposition due to overall higher water levels and greater inundated area and duration (Figure 3.5). In contrast, during low flow, the average SSC was greater due to the import of high-turbidity water from offshore (Glover et al., 2021), enabling greater deposition despite the lesser inundation area and duration. This reimported sediment likely has a different composition, age, and isotopic signal from the fluvial material, based on recent studies of the clinoform in the Gulf of Mottoma (Kuehl et al., 2019). Yet, even without the confirmation of detailed chemical analysis, this seasonal shift in LC-channel turbidity coupled with the seasonally consistent import suggest that sediment from offshore can be retained and deposited on land surfaces. Coastal sediment recycling has been observed in other well studied deltas such as the Mekong (Fricke et al., 2017), Ganges-Brahmaputra (Hale et al., 2019; Rogers et al., 2013), and Wax Lake (Styles et al., 2021). This recycling increases the stability and resilience of deltaic environments to changes in upstream fluvial delivery (e.g., due to damming), at least until the offshore sediment pool is depleted (Nienhuis et al., 2020).

The single LC channel studied here had a low rate of sediment input in comparison to the total load of the Bogale distributary (Table 3.2). However, based on the visual channel survey, there are ~200 comparable channels with mouth widths of 1–10 m along the entire island exterior. All together, these LC channels can import and export 5–8% of the Bogale distributary flow each tidal cycle, which is a significant mechanism by which Meinmahla Island influences the flux of

sediment, dissolved constituents, and heat. Similar exchange ratios were observed in the lower Amazon River (Nowacki et al., 2019), which carries orders of magnitude more water and sediment than the Bogale distributary, suggesting that LC channels provide a comparable proportion of channel-floodplain exchange regardless of distributary or river size. In Meinmahla Island, these exterior LC channels collectively import a total of 0.14–1.5% of the instantaneous Bogale sediment flux, delivering enough sediment to maintain an accumulation rate of 0.02-0.1 cm/y over the entire island. Some models used to assess delta resilience deemphasize these LC channels (e.g., Tejedor *et al.*, 2015a), yet these data show that LC channels are an important and non-negligible pathway for maintaining land-surfaces. Furthermore, LC channels may become linked during higher water levels, creating new HC transport pathways as has been observed in salt marshes (Ortals et al., 2021; Torres and Styles, 2007).

3.5.2 *Hydrodynamics and sediment transport in the island interior*

In intertidal environments, higher-order channels play a dominant role in controlling particle transport, dispersal, and residence time (Sullivan et al., 2019), and the largest channels in Meinmahla Island are high-connectivity. The single HC channel studied here transports 3–7% of the total Bogale distributary flow during each tide (Table 3.2), providing significant opportunities for sediment and associated nutrient and carbon exchange. Enough sediment is fluxed into the island interior by this single channel alone that 0.14–0.18 cm/y of sediment could be deposited over the whole island. However, it is difficult to identify net sediment flux directions and zones of convergence for interior HC channels, due to the complex interactions between multiple tidal and fluvial signals as well as groundwater exchange.

Sediment was fluxed into the island interior at both the southern and northern entrances of the instrumented, HC channel (Figs. 4 and 5). The zone where these fluxes converge is

consequently defined by the balance between the constant, net-seaward fluvial discharge and the two tidal forcings. The fluvial signal resulted in longer duration ebb tides and stronger ebb than flood velocities (Table B.S1) at the northern entrance. Theoretically, this fluvial flux would drive the zone of convergence closer to the southern entrance of the HC channel. However, asynchronous tidal-wave arrival times create pressure differentials, which have been observed to generate net sediment flux and morphologic evolution in a variety of back-barrier environments (Gomes et al., 2020; McLachlan et al., 2020a; Orescanin et al., 2016; Pacheco et al., 2010). In this HC channel there is a delay of 20–30 min in the arrival of the tide between the southern and northern mouths. At a tidal-propagation speed of 7–10 m/s in the ~5-m-deep channel, the tidal waves would create a zone of convergence around 10–12 km. This zone is shoaling and narrowing (Figure 3.8), and the SSC was observed to decrease in this zone (Figure 3.4), suggesting that the zone of deposition is closer to the northern entrance. It appears that the tidal forcing dominates over the fluvial forcing in this channel, demonstrating one challenge for defining the direction of downstream impact in geometric models of channel networks. Channels may have more than one direction of net flux, depending on tidal and seasonal conditions (Table 3.2). This temporal variability is difficult to represent in simplified models, however recent applications of mathematical network analysis (graph theory) have successfully captured similar channel dynamics (Hiatt et al., 2021).

Another important result of these interacting tidal signals is a long residence time for water within the island interior. The interior HC-channel water masses were distinct from the water in the Bogale distributary and there was non-conservative mixing (Figure 3.4). During high flow, the channel water was almost entirely fresh except in the central reach (5–10 km), where there was a region of colder, saline water. During low flow, the salinity reached a minimum in this same central

reach. These deviations in salinity were either driven by salt exchange with groundwater or long residence times of previously imported water from the river, as they would not be produced by the seasonal rainfall patterns. Similarly, in the microtidal Wax Lake Delta, intra-island residence times for water were significantly greater than those in adjacent channels (Hiatt et al., 2018; Hiatt and Passalacqua, 2015), and substantially altered deltaic fluxes of nutrients (Styles et al., 2021). These observations in Meinmahla Island demonstrate that there are comparably long intra-island residence times in HC channels of a macrotidal environment.

The presence of these distinct interior-island water masses also influenced sediment transport by generating baroclinic circulation at the mouths of the channels. During low flow at the southern entrance there was a peak in near-bed SSC, coincident with the region of greatest stratification, indicative of estuarine sediment transport (Figure 3.4). This estuarine circulation plays a critical role in determining sediment sources for the island interior. During low flow, landward, near-bed flow can import dense, marine water containing offshore sediment. This sediment can then be delivered to land surfaces in the well-mixed inner regions of the island, providing a route for recycling of coastal sediment into the delta. HC channels are also a source of sediment to the dendritic LC channels branching farther into the island interior (Ortals et al., 2021), which can efficiently retain sediment. Sediment recycling into mangrove forests is critical for delta-lobe stability, as has been observed in the Sundarbans of the Ganges-Brahmaputra Delta (Wilson and Goodbred, 2015). These observations in Meinmahla Island provide insight into a specific mechanism for sediment delivery.

The interior-channel water masses also interact with hyporheic water in the island. The tidal and seasonal changes in the water table suggest that there is exchange between surface and groundwater (Figure 3.6). During high tides when the land surface is inundated, water and nutrients

can be directly exchanged in the flooded area via diffusion or advection. Direct rainfall on the flats may also provide a freshwater signal. In Meinmahla Island, this vertical exchange is likely dominant during the high-flow season, when the flats are regularly inundated and there is frequent rainfall. In the low-flow season, there is significant, subsurface horizontal exchange. The water table drops during neap tides (Figure 3.6), indicating that water is flowing out of the ground into the tidal channels, and the water table is gradually recharged during the onset of the following spring tides. This cycle suggests that hyporheic water is refreshed on monthly timescales, allowing significant exchange of dissolved constituents, especially carbon (Alongi, 2014; Bouillon et al., 2007). Considering the significant clay content of the sediment (Figure 3.7), it is likely that the majority of this flow occurs along burrows or root pathways (Gleeson et al., 2013; Susilo et al., 2005).

This exchange between surface and subsurface water likely impacts the biogeochemistry of the distributary flow. Groundwater can act as either a source or a sink for salt in mangrove forests (Capo et al., 2006; Ridd and Sam, 1996; Susilo et al., 2005; Wolanski et al., 1980), and it was also observed to impact the water temperature (Figure 3.6). Consequently, this exchange pathway can alter water density, circulation, floc size, and sediment transport in the HC channels, impacting the sediment retention and morphologic evolution of the island. It is also well established that subsurface flow in mangrove forests can significantly alter fluxes of carbon, nutrients, salt, and pollutants through the coastal environment (see review in Alongi, 2014). Previous work in Meinmahla Island demonstrated that groundwater flow impacts rates of greenhouse-gas efflux (i.e., CO_2 and CH_4) (Cameron et al., 2021), so future changes to inundation period could have a significant impact on blue carbon storage.

3.5.3 *Island morphology and decadal-scale evolution*

The multiple flux pathways examined here provide substantial sediment for land development, and Meinmahla Island is both aggrading and prograding despite being located in a zone dominated by coastal erosion (Chen et al., 2020). Sediment cores collected laterally and longitudinally across the island showed similar accumulation rates of 0.26–1.78 cm/y. These relatively high rates are consistent with muddy, mangrove-forested environments, which tend to trap significant volumes of sediment (Alongi, 2014; Gomes et al., 2020; Rogers et al., 2013; Swales et al., 2016). However, individual accumulation rates calculated from these cores should be evaluated with caution due to the possible influence of bioturbation and subsurface water flow, which can alter the ^{210}Pb decay profile (Arias-Ortiz et al., 2018). The presence of excess ^{210}Pb to a depth of 1 m in all cores could reflect these secondary processes. Even with these sources of uncertainty, the observed rates are consistent with the progradation and suggest that Meinmahla Island is keeping pace with subsidence and sea level rise, as previous work has indicated (Chen et al., 2020; Hedley et al., 2010). The overall consistency in accumulation rates and grain size, especially in the shore-perpendicular cores (Fig 7a-e), is likely due to persistent tidal processes. These uniform rates contrast with wave-dominated mangrove forests, where seasonal trends in wave climate can create distinct zones of deposition or erosion (Brunier et al., 2019; Fricke et al., 2017).

Despite the dominant tidal signal, there were indications of storm activity, and a Category 4 cyclone has hit Meinmahla Island roughly once a decade over the past century (Knapp et al., 2018). Cores collected from the western side of the island in the mangrove fringe were more disturbed and less likely to undergo steady-state sediment accumulation (Figure 3.7). The Category 4 cyclones generally bring winds from the west (Knapp et al., 2018), so these cores could reflect regular storm reworking. However, an event layer coinciding with the devastating 2008 Cyclone

Nargis (Aung et al., 2011, 2013; Estoque et al., 2018) was not clearly identifiable in the upper 10 cm. The absence of an event layer could reflect the intensity of bioturbation in mangrove forests and/or the dominant depositional signal from tidal processes.

Overall, the signals preserved in these cores can reasonably be attributed to multiple factors and demonstrate the challenges of connecting modern events to the stratigraphic record. Nonetheless, the regular delivery of sediment during storm surges and floods is an important component of land-surface maintenance that can be inhibited or entirely blocked by anthropogenic levee construction (Gerwing et al., 2020; Rogers and Overeem, 2017; Syvitski et al., 2009). The current resilience of Meinmahla Island is likely directly related to its natural status as a mangrove forest preserve without artificial embankments.

The spatially consistent accumulation rates and relative stability of the channel morphology suggests that the Meinmahla Island tidal channels have reached a dynamic equilibrium or stable network morphology. Tidal-channel networks tend to self-organize into a stable state, controlled by sediment delivery to interior land surfaces (Fagherazzi, 2008; Hiatt et al., 2021; Hood, 2007). The location, sinuosity, and width of the large, HC channels have not changed since the 1960s even as the island has prograded seaward, and the present spacing likely represents an equilibrium configuration. This permanence may be partly maintained by the mangrove vegetation, which both stabilizes the sediment and routes water into existing channels (Van Maanen et al., 2015). The large, HC channel mouths increase the roughness of the island shoreline, which has been quantitatively related to deltaic evolution (Passalacqua et al., 2013). In the western lobe of the Ganges-Brahmaputra Delta, the shape-factor, or perimeter roughness, of islands is greater than in other regions. This western lobe is not directly fed by the mainstem of the river and is primarily maintained by estuarine processes that import sediment from offshore. Since HC channels are an

integral part of estuarine sediment import (Figure 3.4), it seems reasonable that these islands would have more rugose shorelines, punctuated by the mouths of HC channels.

Despite this overall stability, the interior channels of Meinmahla Island are not immobile. The interior channels have responded to changes in connectivity (Figure 3.9), indicating that there are multiple stable states for the channel networks. The opening and widening of a new connection resulted in narrowing and infilling of dendritic channels that previously accommodated the tidal prism. The narrowing zone coincides with a high density of small, secondary channels (Figure 3.8), a pattern which has previously been observed in models of tidal-channel evolutions (Van Maanen et al., 2015) and an infilling back-barrier environment (McLachlan et al., 2020b). The same pattern in Meinmahla Island suggests that this pattern of secondary channels may be a more universal trend in tidal-channel network development and one that could be identified in the stratigraphic record. In some strongly depositional environments this type of channel narrowing eventually leads to channel closure (Hood, 2006; McLachlan et al., 2020b). It is not clear whether this HC channel is progressing towards closure or has reached an equilibrium cross-sectional area. Regardless, the reworking of interior, secondary channels demonstrates that sediment in Meinmahla Island can be recycled both within the island and through the lower delta, increasing sediment residence time. Overall, Meinmahla Island is a component of an active delta system, where sediment can be recycled from local, coastal, and offshore deposits.

These complex flows through LC and HC channels of Meinmahla Island emphasize the capacity for a mid-channel island to influence water-mass characteristics and sediment transport at the river-ocean interface. Yet, the morphology also demonstrates that the island responds to distributary conditions. In fluvial geomorphology, a bar is usually defined as an unvegetated and relatively ephemeral feature that is regularly submerged while an island is vegetated and emergent

(Wohl, 2020). Both features are essentially responding rapidly to the flow, unlike an inter-distributary land mass or a bedrock island in an estuary (Deignan-Schmidt et al., 2021; Guo et al., 2020). In contrast, mid-channel, deltaic islands are regularly submerged, vegetated, and morphologically dynamic over decadal timescales while also influencing the flow. The capacity for these resilient landscape features to influence flow while responding to flow suggests that a sub-category of island should be specified in the literature. These features occupy a distinct and liminal space as part of the land, river, and ocean in the delta connectome (Passalacqua, 2017).

Mid-channel islands are not well accounted for in analytical models of delta development. Nienhuis et al. (2018) identified a geometric relationship of delta-channel widening based on the ratio of tidal to river dominance that provides insight into the evolution of deltas. The formula, which assumes that the channel widens to accommodate the tidal prism, accurately predicts the channel width for three well-studied distributaries in the Ayeyarwady Delta: the Bogale, Pathein, and Yangon (Table B.S2, Glover *et al.*, 2021). However, the width prediction does not consider the presence of Meinmahla Island, which occupies the majority of the volume in the widening Bogale distributary mouth. Consequently, the island must play a role in accommodating the tidal prism without forcing the distributary to widen further. This relationship is not well captured by current models and may make it more challenging to predict the morphologic response of deltas to changes in fluvial or tidal dominance.

3.6 CONCLUSION

This investigation of Meinmahla Island has revealed the processes leading to aggradation and progradation in a relatively natural megadelta. Mid-channel islands in deltas are resilient and active landscape features with multiple pathways to accommodate fluxes of sediment and dissolved

constituents. Exterior, LC channels provide an efficient pathway for sediment retention. However, these channels do not provide enough sediment to maintain land surfaces, and interior networks of dendritic, HC channels are an integral part of island maintenance. The long residence time of water in interior channels creates estuarine conditions at channel mouths, further promoting sediment import. Over each tidal cycle, 1.5% of the Bogale distributary sediment can be carried through a single HC channel. The biogeochemistry of the distributary water is likely altered by this exchange and interactions with groundwater, impacting the flux of nutrients to the coastal ocean.

These multiple pathways make mid-channel islands enduring landscape features, and Meinmahla Island is aggrading relatively uniformly while prograding seaward. Sediment imported to land surfaces is sourced from both upriver and recycling of local and offshore deposits, making the island more resilient to the loss of any single source. The complex channel networks increase the rugosity of the island perimeter while delivering sediment to the island interior. Finally, interior channel networks respond to perturbations over decadal timescales, arriving at new equilibrium configurations.

This *in-situ* investigation of Meinmahla Island provides insights into the processes that create natural delta morphology. Overall, mid-channel islands are not passive obstacles to flow and sediment transport, and these landscape features efficiently trap and recycle sediment. However, this work also identifies new issues for predicting delta stability based on planform geomorphic features. Tidal channels may not behave uniformly over tidal and seasonal timescales, and low-connectivity channels cannot be ignored as sediment transport routes. Furthermore, there are multiple routes for coastal sediment recycling that may increase delta resilience. These natural processes are foundational for building and maintaining land surfaces at the river-ocean interface.

Chapter 4. ASSESSING THE RESILIENCE OF UN-LEVEED AGRICULTURAL FIELDS IN THE AYEYARWADY DELTA

4.1 INTRODUCTION

Many tropical and sub-tropical deltas are densely populated centers of agriculture that are threatened by sea-level rise (SLR). Local SLR can be amplified by anthropogenic activities that enhance subsidence, such as damming, fluid extraction, coastal deforestation, and levee or polder construction (Syvitski et al., 2009). Often, these alterations to the landscape are driven by the need to expand agriculture and aquaculture, and local stakeholders must balance economic stability against future declines in coastal resilience (Chapman et al., 2016). Economically viable policies to promote delta stability require a fundamental understanding of the individual impacts of anthropogenic activities on sediment dynamics, yet it is often challenging to isolate the impact of a specific intervention in heavily altered regions.

Mangrove removal has accelerated in many deltaic regions with the expansion of agriculture and aquaculture (Duke et al., 2007; Giri et al., 2011). However, this agricultural expansion is frequently accompanied by the construction of levees or polders for flow regulation, making it difficult to isolate the impact of the change in land cover. Levees allow a second or third round of crops to be grown in monsoonal deltas during the dry season when river or distributary water is saline (Chapman et al., 2016). Unfortunately, levees also isolate the floodplain, significantly decreasing the potential for sediment deposition. In regions such as the Ganges-Brahmaputra and Mekong Deltas, embanked regions are experiencing rapid subsidence (Angamuthu et al., 2018; Auerbach et al., 2014; Brown and Nicholls, 2015; Rogers and Overeem,

2017) and tidal-channel infilling (Bain et al., 2019). Consequently, it is vitally important for policy makers to understand the relative stability and economic value of natural intertidal environments (e.g., mangrove forests, marshes), deforested fields that have no levees (supporting one annual crop or "single-cropping"), and fields with levees (supporting multiple annual crops) over decadal to century timescales.

In the absence of levees, intertidal vegetation promotes positive, ecogeomorphologic feedbacks that retain sediment to fill accommodation space (Coco et al., 2013; Friess et al., 2019). Sediment deposition and accumulation rates depend on vegetation characteristics, from the individual plant scale (e.g., height, diameter, density, rigidity) to ecosystem scale (e.g., flow routing, species zonation, tidal-channel density) (Chen et al., 2018; Vandenbruwaene et al., 2013). Little is published about the sediment trapping capacity of crops such as rice, *Oryza sativa*. In Southeast Asia, rice is optimally planted at 200–500 stalks/m^2, resulting in up to 2 kg/m^2 of above-ground biomass (Zheng et al., 2019), which is comparable to that of a typical saltmarsh (Fagherazzi et al., 2013). This comparably dense vegetation suggests that sediment retention could be similar.

The Ayeyarwady Delta, Myanmar (Figure 4.1) provides a rare opportunity to directly measure sediment dynamics and land-surface stability in un-leveed rice fields. Through the mid-1900s, mangrove forests covered the majority of the delta. Between 1978 and 2011, ~64% of mangrove forests were cleared in the delta, and ~88% of that cleared land was converted to rice fields (Leimgruber et al., 2005; Webb et al., 2014). However, there has been little levee construction in the lower delta, since many farmers grow one crop annually during the wet season when the distributary water is fresh (Sakai et al., 2021). Furthermore, there are no mainstem dams on the Ayeyarwady River (Grill et al., 2019) and sediment supply has not declined as much as in other major river systems (Chen et al., 2020). Consequently, the impact of the change in land cover

can be evaluated by comparing the sediment dynamics and morphology of remaining mangrove forests and un-leveed fields. Here, we use *in-situ* observations from a mangrove forest preserve and an adjacent, un-leveed agricultural field to address the following questions:

1. How do sediment transport, retention, and elevation compare in an un-leveed agricultural field and in a natural mangrove forest?
2. Are un-leveed agricultural fields stable with respect to local SLR over decadal timescales?

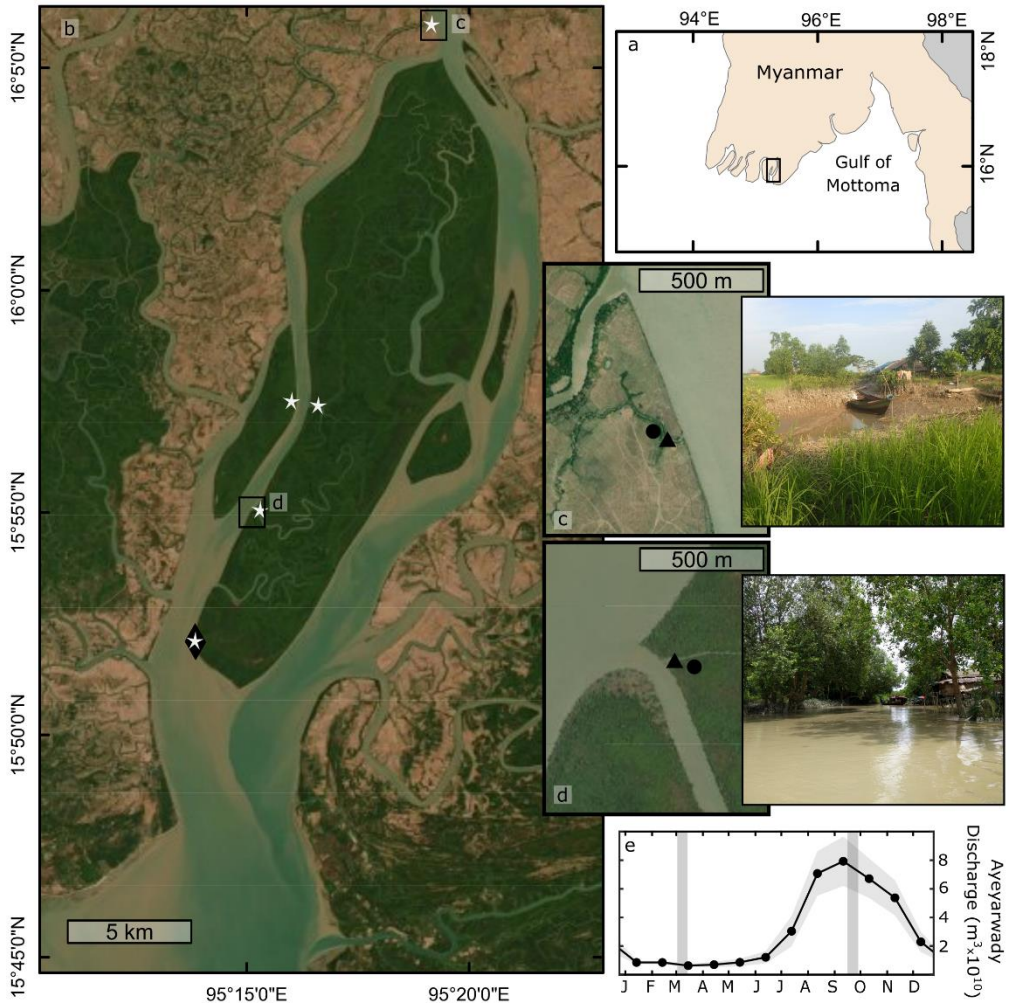

Figure 4.1. Regional maps and images of the study site. (a) Myanmar and the Gulf of Mottoma, and (b) Meinmahla Island. The aerial imagery is from Maxar WorldView, collected in November 2019. The 2019 GPS-RSK survey locations are marked with white stars, the fixed-instrument sites

are marked with black diamonds, and the Aquadopp deployment sites are highlighted with black boxes. (c) The inset of the agricultural field and (d) forest dead-end channels show the Aquadopp sites in black triangles and the core locations in black circles. A photo of each tidal channel during the wet season is provided for visual reference (photo credits: H. Glover). (e) The average annual discharge ±1 standard deviation of the mainstem Ayeyarwady River at Pyay is shown (Furuichi et al., 2009), with the sampling seasons marked with grey bars.

4.2 STUDY SITE AND METHODS

4.2.1 *Study site*

The Ayeyarwady River drains through Myanmar to the Gulf of Mottoma. The river carries $379\pm9\times10^9$ m^3 of water and 326±91 Mt of sediment annually (Baronas et al., 2020), making it the third largest river globally, by sediment load. In the ~250-km-wide Ayeyarwady Delta, the river splits into multiple rejoining distributaries. The majority of discharge occurs during the southwest, wet monsoon (June–October), when the distributaries are primarily fresh, tidal rivers. Sediment can be reimported from the shelf to the delta during the northeast, dry monsoon, when the distributaries become estuarine (Glover et al., 2021). The western coastline of the delta is dominated by erosion and seasonal reworking by storms, while the eastern coastline is dominated by muddy deposition and reworking by macrotidal currents (Chen et al., 2020).

Two adjacent sites, one in a mangrove forest preserve and one in an agricultural field, were selected for investigation. The sites are located along the Bogale distributary (Figure 4.1), at the approximate boundary between the eastern and western zones and within the study region of a 2017–2019 investigation of the Ayeyarwady Delta (Glover et al., 2021). The forest site was located in Meinmahla Kyun (Island), a Ramsar mangrove preserve (Ramsar site 2280, https://www.ramsar.org/). This island is in a dominantly agricultural region that was progressively

deforested over the past 80 years (Webb et al., 2014). The forest on the island is composed of a dense mixture of mangroves, predominantly *Avicennia marina* and *Heritiera fomes*, and mangrove associates, such as *Nypa fruticans*, with a typical canopy height of ~4 m (Win et al., 2019). The agricultural study site was in a ~45-year-old field (Figure 4.1) that is used to grow one annual crop of a local variety of rice during the wet monsoon (Thant et al., 2020).

4.2.2 *Field measurements*

Seasonal conditions were recorded by measuring the water level, turbidity, salinity and atmospheric pressure semi-continuously at the southern end of Meinmahla Island. During the low-flow (March 2018) and high-flow (September 2019) seasons, the water velocity, turbidity, and salinity were measured in a 7-m-wide dead-end tidal channel in the mangrove forest and agricultural field. The Bogale distributary turbidity is comparable at the two channel entrances (Glover et al., 2021), so the study sites represent comparable systems despite the distance between locations (Figure 4.1). In each dead-end channel, an upward-facing Nortek Aquadopp current profiler was deployed over 3–4 tidal cycles during the transition between spring and neap tides. Each instrument was equipped with two integrated Optical Backscatter Sensors (OBSs) at 0.15 and 0.3 m to measure turbidity. The instruments sampled for 30s every minute at 1 Hz.

The absolute elevations of the mangrove forest and agricultural field were measured in September 2019 using a Septentrio GPS-RTK. The vertical accuracy varied from mm- to cm-scale depending on tree-canopy coverage. The elevation was corrected to a local reference datum, i.e., the chosen elevation of 0.0 m, based on the mean sea level at the seaward end of Meinmahla Island during the high-flow season (SI Figure). There is no universally acknowledged datum for elevation in a tidal river (Hoitink and Jay, 2016), so this value was selected as a locally useful reference. The datum is 46.4 m below WGS 1984 UTM Zone 46N.

Cores were collected with a 1-m-long auger on the land surface in Meinmahla Island and the agricultural field. Both cores were collected ~10 m from the channel edge, in locally representative environments. At the agricultural site, the core was collected within the rice field, as far from buildings as possible. On Meinmahla Island, the core was collected within the mangrove forest. Cores were subsampled in the field at 2–5 cm intervals.

4.2.3 *Lab work and data processing*

The OBS voltage responses were converted to a calibrated suspended-sediment concentration (SSC) using known concentrations of sediment from the deployment sites (n=10, r^2= 0.8–0.91). SSC was calculated by filtering ~0.1 L of water through pre-weighed and desiccated 0.45 µm nitrocellulose membrane filters. The Aquadopp data were cleaned to remove periods when the instruments were out of water or shifted. Water velocity was rotated to a channel-oriented reference frame, where landward values are positive and seaward/riverward values are negative. The instantaneous sediment flux was calculated from the depth-averaged velocity and the average SSC recorded by the two OBSs.

The subsampled sediment cores were processed for grain size and geochronology. Samples were disaggregated by sonicating in a 0.05% sodium metaphosphate solution and were analyzed in a Beckman-Coulter LS13- 320® Particle Size Analyzer. The sediment-accumulation rate was calculated using down-core measurements of ^{210}Pb. The ^{210}Pb isotope has a 22.3-y half-life and is commonly used to calculate century-scale accumulation rates in muddy environments with steady-state accumulation (Nittrouer et al., 1979). The total ^{210}Pb activity was calculated by measuring the activity of the granddaughter ^{210}Po in relation to a known ^{209}Po spike. Activity was normalized by mud fraction and the supported activity, 0.7 dpm/g, was calculated from the average of the

deepest samples (Chapter 3). Excess activity was calculated by subtracting supported activity from the total activity, and the accumulation rate, S, in cm/y was determined from:

$$S = {\lambda \Delta z}\Big/{\ln\left(\frac{A_0}{A_z}\right)} \quad (4.1)$$

where λ is the decay constant of ^{210}Pb, 0.0311 y^{-1}, A_0 is the excess activity at the top of the log-layer, A_z is the activity at depth z, and Δz is the depth difference between the points. The accumulation rate was also estimated in the agricultural field using ^{137}Cs, measured by gamma spectroscopy (Text C.S1).

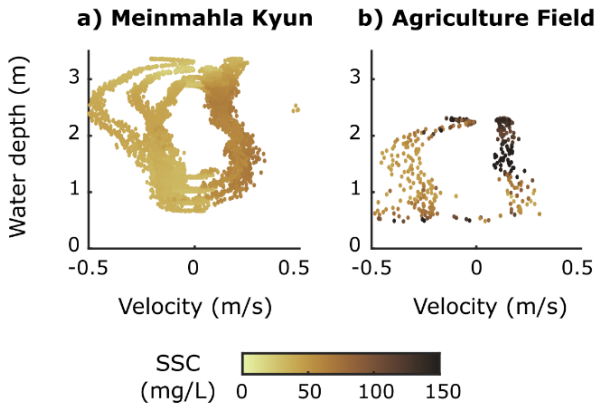

Figure 4.2. Velocity-stage-SSC diagrams from a dead-end tidal channel of a) Meinmahla Island and b) the agricultural field (see Figure 4.1 for locations).

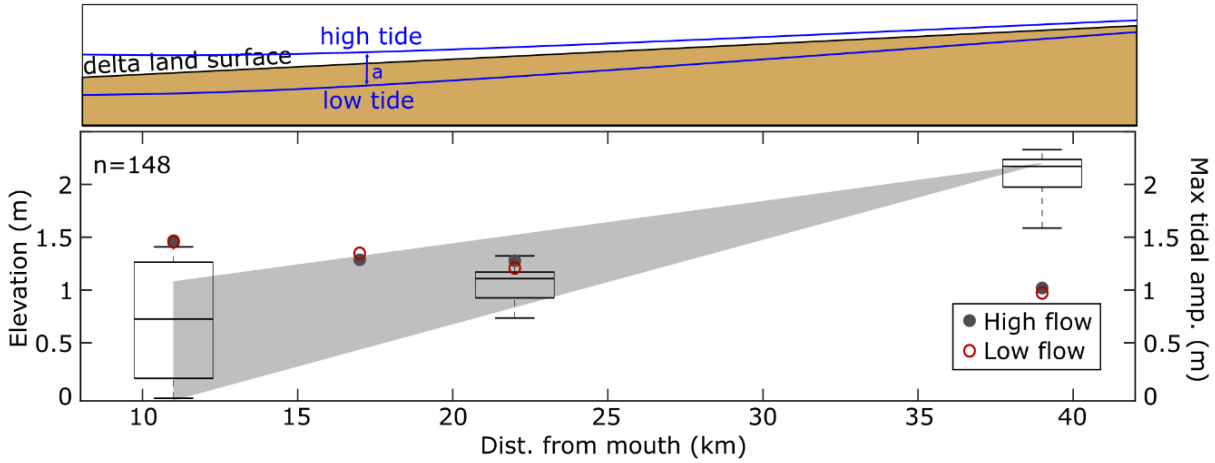

Figure 4.3. Boxplots of elevation and tidal amplitude. The elevation is referenced to the mean high-flow tidal elevation at the seaward end of the island, collected in Meinmahla Island (10–23 km from the river mouth) and the agricultural field (~39 km from the river mouth) with the maximum observed tidal amplitude (*a*) during the Aquadopp deployments shown as circles. The grey shaded area shows the envelope of land surface elevations based on published estimates of the delta slope (Nienhuis et al., 2018; Syvitski and Saito, 2007). A cartoon of the land surface and tidal range is included at the top for reference.

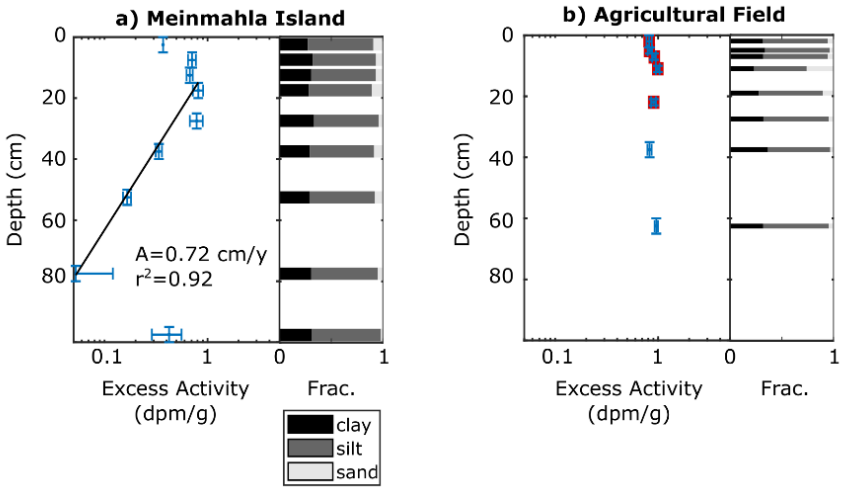

Figure 4.4. Profiles of excess ^{210}Pb and grain size from a core collected in a) Meinmahla Island and b) the agricultural field. The best-fit line, accumulation rate, and r^2 value are shown for the Meinmahla Island core.

4.3 RESULTS

The hydrodynamics in both dead-end channels were remarkably similar. The tidal range was comparable during the high- and low-flow seasons and captures the transitional period between spring and neap tides. The dead-end channel in the mangrove forest, 17 km from the river mouth, had a 2.7 m range and the dead-end channel in the field, 39 km from the river mouth, had a 2 m range (Figure 4.2). Unfortunately, most of the velocity data from the low-flow deployment in the forest and the high-flow deployment in the field was corrupted due to instrument disturbance (e.g., movement by either farmers or crocodiles). The remaining data suggests similar seasonal patterns, which are consistent with previous studies of the area (Chapter 3), so only one deployment is shown for each site. Water velocities in both locations were generally <0.5 m/s. There was an ebb pulse at both sites, and the maximum ebb velocity, ~0.5 m/s, was higher than the maximum flood velocity, ~0.3 m/s (Figure 4.2). However, the SSC was consistently greater during the flooding tide, and there was a net landward sediment flux of 0.001–0.004 kg/m/s in the forest channel and 0.002–0.004 kg/m/s in the field channel.

The land-surface elevation (Figure 4.3) was measured along shore-perpendicular transects at multiple locations (Figure 4.1). The maximum elevation was +1.4 m in the forest and was +2.4 m in the field. These values are comparable when accounting for the along-delta distance between the sites and published estimates for the delta slope, 4–8 cm/km (Nienhuis et al., 2018; Syvitski and Saito, 2007). The elevation and tidal range were used to calculate the maximum inundation depth and the average inundation duration of the land-surface adjacent to the forest and field channels. The maximum inundation depth was 0.25 m in the forest and 0.31 m in the field. The average inundation duration per tide was 108 min in the forest and 170 min in the field.

The sediment cores also reveal similarities between the two sites. The core collected in the mangrove forest was consistently ~60% silt and ~30% clay, with an average D_{50} of 10 μm (Figure 4.4). The upper 0.1 m of the core had significant organic content, and the excess ^{210}Pb was relatively uniform in the upper 0.4 m of the core. The apparent accumulation rate calculated from ^{210}Pb was 0.71 cm/y ($r^2 = 0.91$). The grain size and accumulation rate were consistent with previous cores collected throughout the island (Chapter 3). The core collected in the agricultural field had similar grain sizes with ~60% silt, ~30% clay, and an average D_{50} of 9 μm. The activity of excess ^{210}Pb was constant down core, including below the depth of plowing, suggesting deposition of sediment within the past century. ^{137}Cs was observed intermittently down to 60–65 cm, suggesting an accumulation rate of ~0.7 cm/y (Figure C.S1). However, it is likely that this rate is an overestimate due to downward diffusion (Alexander et al., 1991).

4.4 DISCUSSION

The lower Ayeyarwady Delta is a tide-dominated environment at sea level, where floodplains are regularly inundated. In this type of environment, accommodation space is continually generated by subsidence, and sediment must be retained for land surfaces to keep pace with local SLR. The goal of this study was to evaluate the relative resilience to subsidence of an un-leveed agricultural field with respect to an adjacent mangrove forest in the Ayeyarwady Delta. The data presented here demonstrate that both a field and forest environment have been keeping pace with historical rates of SLR by retaining sediment.

The relative resilience of the field can first be demonstrated by examining the land-surface elevation. The measurement sites were spread over a ~40 km stretch of the Bogale distributary so the slope of the delta must be accounted for when comparing between the field and forest. The

slope of the delta is 4–8 cm/km (Nienhuis et al., 2018; Syvitski and Saito, 2007), and the measured elevations fell within this range of slope estimates (Figure 4.3). Considering that the field is 40–50 years old, this elevation data alone suggests that the field is significantly more resilient than equivalent leveed environments of other deltas, many of which have experienced meter-scale subsidence over the same time period (Auerbach et al., 2014; Koppenaal et al., 2021; Rogers and Overeem, 2017).

In intertidal environments, it is also important to consider the relative elevation of the land surface with respect to the tidal frame (Fagherazzi et al., 2013). Sediment can be deposited when the flats are inundated, and inundation duration can directly correlate to sediment retention (Horstman et al., 2013a). The field and forest sites had comparable inundation depths during spring tides, and the inundation duration was slightly longer in the agricultural field. These two floodplain environments would be capable of retaining comparable amounts of sediment, further supporting the similarity of the two sites.

The instrument records indicate that sediment is retained in both environments, likely due to the dense vegetation of the rice field and mangrove forest. The patterns of water velocity in the dead-end channels (Figure 4.2) are consistent with that in many channels bisecting vegetated environments (Furukawa and Wolanski, 1996; Horstman et al., 2013a; Mazda et al., 1995; McLachlan et al., 2020a; Santen et al., 2007; Wolanski et al., 1980). The velocity peaked during ebb and flood as the channel-water level approached the elevation of the flats, and the ebb velocity was greater due to the delay in draining caused by the high-friction vegetation. Despite this ebb-dominant water velocity, the turbidity was consistently greater during flood tides and there was net landward sediment flux. It is well documented that vegetation enhances sediment retention through the reduction of flow energy (Mullarney et al., 2017; Norris et al., 2017), direct trapping

on above-ground biomass (Fagherazzi et al., 2013), and the formation of cohesive biofilms (Woodroffe et al., 2016). In fact, subtropical saltmarshes have been shown to trap more sediment than mangroves by directly retaining sediment on vegetation (Chen et al., 2018). The data presented here suggests that rice crops also have the capacity to trap sediment, likely through these same mechanisms.

It is challenging to prove whether the observed rates of sediment retention are sufficient to keep pace with local SLR. There are no published rates of SLR for the Ayeyarwady Delta, and local SLR may diverge significantly from eustatic SLR due to tectonic movement associated with the Sagaing Fault (Kuehl et al., 2019; Vigny et al., 2003). The accumulation rate adjacent to a dead-end channel in Meinmahla Island, 0.72 cm/y, was consistent with other cores collected from the island (Chapter 3). A comparably robust accumulation rate could not be calculated for the agricultural field. The upper 15–20 cm of the field are regularly reworked by plowing (Goodbred and Kuehl, 1998; Hayashi et al., 2006), making it especially difficult to estimate accumulation rates in the period since mangrove removal. However, Meinmahla Island is currently prograding seaward at ~20 m/y (Chen et al., 2020). Since the Island and field occupy similar regions of the tidal frame, it seems that historical aggradation has been sufficient to keep pace with SLR at both sites. Overall, both the mangrove forest and rice field regularly import sediment and are stable with respect to SLR. However, the accumulation rates may not be sufficient if local SLR accelerates due to tectonic movement, eustatic SLR, or further anthropogenic alterations.

4.4.1 *Management considerations and caveats*

This study demonstrates that coastal resilience in leveed and un-leveed agricultural fields should be evaluated differently. This study demonstrates that coastal resilience in leveed and un-leveed agricultural fields should be evaluated differently. Despite deforestation, it appears that this

agricultural region in the Ayeyarwady Delta is retaining sediment and aggrading. This stability emphasizes the long-term economic and ecologic importance of avoiding levee construction. Constructing levees may provide farmers with greater short-term income from multiple annual crops, but the inevitable subsidence of lands will rapidly decrease the economic viability of leveed areas (Chapman and Darby, 2016). In contrast, un-leveed fields may provide a lower but more consistent income. The lack of levees could contribute to the future resilience of the Ayeyarwady Delta. It is also important to note that the agricultural field is only able to aggrade because the sediment supply of the Bogale distributary has not been significantly reduced by damming (Baronas et al., 2020). The stability of deltas fundamentally depends on the fluvial sediment flux, and levee removal alone may not result in greater sediment retention in heavily dammed systems such as the Mekong River (Syvitski et al., 2009).

There are also broader considerations when assessing the ecosystem services provided by natural mangrove forests. Mangrove forests store carbon, cycle nutrients, provide habitat, and reduce pollution (Alongi, 2014). Furthermore, mangroves provide protection for both people and land-surfaces during storm events (Alongi, 2008; Blankespoor et al., 2017). In 2008, Cyclone Nargis made landfall in Ayeyarwady Delta causing the worst natural disaster in the history of Myanmar (Fritz et al., 2009). The Category 4 cyclone caused flooding up to 50 km inland, killing at least 138,000 people and destroying 90–95% of the buildings in the delta. The storm passed directly over Meinmahla Island, where the storm damage and mortality were locally reduced by the protection of the forest (Aung et al., 2011, 2013; Estoque et al., 2018). In contrast, agricultural areas throughout the delta were severely damaged (Omori et al., 2020). These types of large, damaging storms may be more common in the future (Hirano, 2021), providing a clear motivation

for maintaining existing mangrove forests. Even if agricultural fields can accrete at the same pace as mangrove forests, they do not offer the same degree of storm protection.

Additionally, estimates of the century-scale aggradation of these fields must consider ecogeomorphic feedbacks. Sediment is delivered to distal regions by networks of tidal channels, which are a fundamental component of the delta (Ortals et al., 2021; Passalacqua, 2017). Consequently, the condition of these channels will directly impact the resilience of the fields. Rice may not provide the same bank stabilization as mangrove roots and biofilms (Roskoden et al., 2020; Woodroffe et al., 2016). This reduction in sediment stability may result in channel infilling and reduced floodplain sediment delivery. Furthermore, a review of satellite imagery showed a noticeable reduction in channel-network density in fields (Fricke et al., 2020), possibly due to manual infilling by farmers. Loss of interior channels may result in non-linear changes to topography, as there is often three-dimensional circulation of flow through channels and over intertidal flats (Torres and Styles, 2007). Consequently, the sedimentation rates reported here, adjacent to channels, may not be representative of future rates in distal delta regions.

4.5 CONCLUSIONS

In the Ayeyarwady Delta, an un-leveed rice field was capable of retaining sediment over tidal and decadal timescales to keep pace with local SLR. This study demonstrated that agricultural fields without levees were significantly less susceptible to subsidence than leveed fields, and single-cropping may be a useful strategy for maintaining vulnerable deltas. However, the decision to replace mangrove forests with agricultural fields should weigh the short and long-term benefits provided by each environment. Agricultural fields do not provide the same ecosystem services as healthy mangrove forests.

Chapter 5. DECADAL-SCALE IMPACTS OF MANGROVE REMOVAL IN WAIKARAKA ESTUARY, NEW ZEALAND: SEDIMENT DYNAMICS AND MORPHOLOGICAL EVOLUTION[3]

5.1 INTRODUCTION

Mangroves are the only woody plants that grow in the intertidal zone, providing numerous ecosystem services including coastal protection and stabilization, carbon sequestration, and habitat creation (see review in Friess et al., 2019). Unfortunately, mangrove forest loss is occurring throughout the world, often in regions that are also impacted by local sea level rise (Duke et al., 2007). Predicting the impacts of removal requires understanding the fundamental relationships between mangroves and coastal morphology. Isolating the impact of mangroves can be challenging because sediment dynamics are controlled by complex interactions between flow, morphology, and vegetation over a wide range of spatial and temporal scales. Research in the 1990s indicated that mangroves were integral engineers, claiming new intertidal habitat for themselves by damping shear stress and retaining fine sediment (Augustinus, 1995; Mazda et al., 1997; Woodroffe, 1992; Young and Harvey, 1996). However, recent work has established that mangroves can act as opportunistic colonizers, occupying intertidal area after increased sedimentation has elevated bed levels to create suitable habitat (Swales et al., 2015). While the rate of both sedimentation and mangrove forest evolution are site-specific, a fundamental understanding of the feedbacks between

[3] This chapter was submitted to Earth Surface Processes and Landforms as Glover, H.E., Stokes, D.J., Ogston, A.S., Bryan, K.R., Pilditch, C.A.. "Decadal-scale impacts of changing mangrove extent on hydrodynamics and sediment transport in a quiescent, mesotidal estuary", and was accepted for publication on 21 December 2021.

biotic and abiotic processes can be gained by integrating field observations with modeling of hydrodynamics and sediment transport.

Aotearoa New Zealand (A-NZ) is one of the few regions worldwide where mangroves are currently expanding. This expansion is primarily attributed to estuarine infilling due to land-use changes (Lovelock et al., 2010; Swales et al., 2007). Land-surface erosion and coastal turbidity first increased with the arrival of Māori ~1000 years ago and accelerated in the 1800s with European deforestation and farming. The expansion of *Avicennia marina* subsp. *australasica*, the only mangrove species found in A-NZ, is typically associated with fine sediment retention, declining bivalve populations and community perceptions of negative recreational and aesthetic impacts (Dencer-Brown et al., 2018). Consequently, many sanctioned and unsanctioned mangrove removal projects have taken place, motivated by the expectation of a rapid return to sandy estuary-bed conditions. Unfortunately, most removals do not result in rapid restoration (Bulmer et al., 2017a; Stokes and Harris, 2015; Swales et al., 2015), demonstrating the need for a clear understanding of the context-specific role of mangroves in estuarine sediment dynamics.

In this study, we explore how changing mangrove coverage influences estuarine hydro- and sediment dynamics using field observations and numerical modeling. Waikaraka Estuary in Tauranga Harbor, A-NZ (Figure 5.1) provides an opportunity to identify the drivers of estuary evolution over decadal timescales as mangrove extent changes. Here, data collected in Waikaraka Estuary in 2019, more than a decade after a mangrove removal project, is used to identify the *in-situ* impacts of removal. Numerical modeling is then used to examine the historical hydrodynamic regime in the estuary and the impact of varying mangrove extent. This combined approach aims to address the following two research questions.

1. How does a quiescent embayment evolve over decadal timescales following mangrove removal?
2. How does mangrove expansion impact hydrodynamics? Are mangroves engineering new habitat or opportunistically colonizing and altering pre-formed intertidal areas?

Addressing these questions can provide new clarity on where mangrove removal will have the largest impact on estuarine sediment dynamics.

5.2 Background: Intertidal sediment dynamics

Fundamentally, estuarine morphology changes due to net sediment deposition or erosion. Flow, sediment, bathymetry, and vegetation interact, producing Eulerian and/or Lagrangian asymmetries in sediment transport and morphologic change. This complex topic is well-explored in the literature (e.g. Friedrichs, 2011), and just a brief description of the relevant processes is provided here for context.

Tides are a dominant control on coastal morphology, and several types of tidal asymmetry are typically considered when evaluating geomorphic evolution such as duration asymmetry, slack-water asymmetry, and peak-velocity asymmetry (Guo et al., 2019). These asymmetries are produced by the distortion of the tidal wave in shallow water (Dronkers, 1986). On shoaling flats, the flood tide is shortened, producing faster flood velocities, flood-dominated transport, and net landward sediment transport. Slack-water asymmetry similarly results from deformation of the tidal wave, resulting in unequal durations of high-slack and low-slack water and net landward sediment transport (Postma, 1967). For example, grains (or flocs) can travel farther shoreward during a high tide-slack than during the following shorter low-tide slack, ultimately creating gradients in grain size or deposition (Horstman et al., 2013a).

Peak-velocity asymmetry results from differences in the magnitude of the velocity during ebb or flood tide, which may be associated with duration asymmetry. For example, an “ebb pulse”, a peak in ebb-velocity due to slow draining of extensive, high-friction flats into a smaller channel, was identified early in the study of tidal systems (e.g. Bayliss-Smith et al., 1979; Mazda et al., 1995; Pethick, 1980) and has since been replicated in numerical modeling (e.g. Temmerman et al., 2005). Residual circulation caused by other factors, such as complex bathymetry (Dronkers, 1986), river discharge (Nidzieko and Ralston, 2012) or channel connectivity (McLachlan et al., 2020a) maybe superimposed on tidal asymmetry. Cohesive bed-sediment can add further complexity, as net deposition can occur despite symmetric peak ebb and flood velocities. For example, fines entrained by turbulent flood flows can settle out at slack high-tide, creating cohesive mud deposits that cannot be eroded by equivalent ebb flows (Furukawa et al., 1997).

Coarse-sediment transport is generally dominated by bed transport and scales with peak velocities. In contrast, fine-sediment transport in shallow environments is strongly influenced by flocculation and the resulting settling velocity, slack-water duration, spatial variation in tidal characteristics, and bed cohesion. The direction and magnitude of the tidal asymmetries that control coarse and fine sediment transport can be quantified using harmonic analysis of tidal constituents only if a sufficiently long record of water level exists (Guo et al., 2019). For shorter records that may not accurately capture all tidal constituents, asymmetry can be calculated from the skewness of the water level, velocity, and acceleration (Guo et al., 2019; Nidzieko and Ralston, 2012).

Waves also play a significant role in intertidal sediment transport and morphology. Short-period waves can rework the bed, promoting erosion. These waves tend to produce a concave-up estuarine profile, where sediment is eroded from energetic mid-depths and transported to more

quiescent inland zones (Friedrichs, 2011). On shallow tidal flats even small-amplitude waves can increase sediment transport (Hunt et al., 2015). Annual and seasonal wave climates can also interact with tidal transport to produce unique morphology. In these environments it can be informative to examine the total, wave-current bed-shear stress (Hunt et al., 2016).

Intertidal vegetation, such as mangrove forests, adds an additional layer of complexity to the interactions between tides, waves, and pre-existing morphology. Isolating the role of mangroves in geomorphic change is challenging because mangrove forests develop over similar timescales to those of broad geomorphic evolution. Moreover, the characteristics of the mangrove forest are species and site specific. For example, prop roots of *Rhizophora* spp. and pneumatophores of *Avicenna* spp. directly influence flow, increasing friction and turbulence (Krauss et al., 2003; Mazda et al., 1997; Mullarney et al., 2017). Once established, dense networks of mangrove roots act to stabilize sediment (Roskoden et al., 2020), while associated surface algae (biofilms) can also increase bed erosion thresholds (Horstman et al., 2018b; Woodroffe et al., 2016). Furthermore, mangroves attenuate energy (Massel et al., 1999; Mazda et al., 2006; Montgomery et al., 2019; Mullarney et al., 2017), which can lead to unintuitive sediment accumulation patterns on wave-dominated mangrove coasts (Fricke et al., 2017). Conversely, wave climate can also limit the expansion of mangroves by controlling seedling dispersal and survival (Swales et al., 2015).

Dynamic equilibrium, as defined by Friedrichs (2011), is achieved when the shape of the intertidal area does not change significantly, and net sediment transport is negligible, over a relevant timescale (e.g., tidal, spring-neap, annual, or storm-recovery cycle). The sediment accumulation rate is ultimately regulated by sediment supply and accommodation space, which is controlled by local relative sea level rise (rSLR) and wave climate (Posamentier et al., 1988;

Schlager, 1993). Systems at dynamic equilibrium can subsequently become unstable if a parameter shifts (e.g., a change in wave climate, rSLR, sediment supply, or vegetation extent). One way shifting equilibrium may manifest is through changes to tidal-channel morphology. For example, tidal-channel sinuosity may increase or decrease due to feedbacks between channel slope, sediment supply, channel depth and velocity, margin deposition, and vegetation coverage (Larsen, 2019).

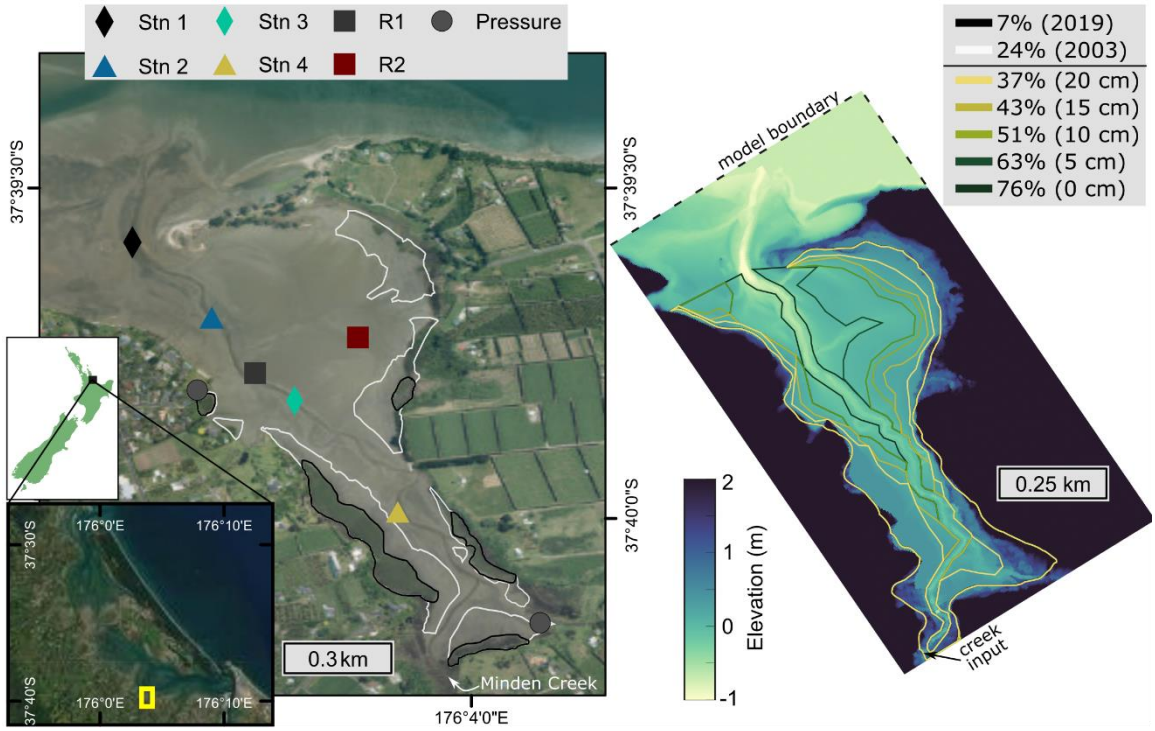

Figure 5.1. Map of Waikaraka Estuary, located in Tauranga Harbor on the North Island of Aotearoa New Zealand (insets). The instrument deployment locations are marked with filled symbols; see Table 5.1 for instrument details. The mangrove extent is outlined for 2003 (white) and 2019 (black). The model domain and 2019 bathymetry are shown on the right. The experimental mangrove extents are indicated in solid lines (see Table 5.2 for details). The legend displays the percent of estuary covered and the elevation of the lower limit of mangrove extent, relative to mean sea level, for each model run. Aerial imagery was accessed through ESRI ArcMap.

5.3 Study area, Observational Methods, and Numerical Modeling

5.3.1 *Study area*

Waikaraka Estuary is one of many intertidal embayments in Tauranga Harbor, a meso-tidal barrier-enclosed lagoon on the North Island of A-NZ (Figure 5.1). A small amount of fresh water is supplied to the estuary by a ~10 km^2 catchment, which primarily drains via Minden Creek with an average discharge of ~90 L/s (Hope, 2002). This creek connects to the central channel running through broad tidal flats with fringing mangroves, similar to many embayments in A-NZ. The estuary is well-mixed due to the shallow bathymetry and minimal freshwater input (Tay et al., 2013). The estuary axis is oriented northwestward and lies ~10 km from the southern mouth of Tauranga Harbor. The prevailing wind direction is from the southwest with typical wind speeds <3 m/s (de Ruiter et al., 2019). In Tauranga Harbor, wind waves are limited by short fetch, and ocean swell propagation is limited by the barrier island and tombolos at each entrance. Wave propagation from the Harbor into Waikaraka Estuary is further attenuated by a mouth bar.

Waikaraka Estuary has been impacted directly and indirectly by anthropogenic activities. The catchment has a mix of agricultural and residential usage, including farmland directly abutting the estuary. Over the past ~200 years, the estuary has been subjected to increased sedimentation like many estuaries (Swales et al., 2007). Pre-European accumulation rates, calculated from carbon dates, were ~0.1 mm/y. Accumulation dramatically increased to 10–36 mm/y from 1920 to 1950 before stabilizing at 2.3 mm/y, which is comparable to local rSLR (Stokes, 2010). *Avicennia marina* began colonizing Waikaraka Estuary in the 1940s, expanding to cover 23% of the estuary by 2003 (Stokes et al., 2009). Mangrove removal projects were undertaken between 2005 and 2009 in an effort to restore a sandy bed, and mangrove extent is now maintained at 7% coverage (Figure 5.1). At this extent, mangroves are inundated only at high tide.

Physical and biological changes to the estuary were monitored during and after the initial clearing in 2003 (Stokes, 2010; Stokes et al., 2009). Prior to removal, bed sediment in the mangroves was finer, and sediment deposition rates were higher, than on adjacent unvegetated tidal flats. Immediately after clearing, fine sediment was redistributed across adjacent intertidal surfaces. However, after 18 months, the surface sediment in the estuary was still predominantly muddy. In 2019 the lower estuary was found to be sand dominated, with mud still evident in existing mangroves (Glover et al., 2020). Mud was also present in cleared areas, and particularly deep, soft mud was found in the upper estuary, which was completely cleared of mangroves in 2008.

5.3.2 *Field observations and data processing*

Instruments were deployed for two weeks in June 2019, during austral winter, to examine modern sediment transport in the estuary (Table 5.1, see Figure 5.1 for deployment locations). Two upward-facing Nortek Aquadopp current profilers and two Nortek Vector current meters were deployed in the channel, each with 1–2 integrated Optical Backscatter sensors (OBSs) to measure turbidity. The instrument record at Station 1 was truncated due to instrument failure after a week. Both Aquadopp instrument frames were also equipped with Onset Hobo conductivity sensors to measure salinity along the channel. Wave characteristics on the tidal flats were recorded with two RBR Duos, measuring waves and turbidity, along a transect perpendicular to the channel. Finally, a Solinst water level logger was deployed in the upper estuary to provide additional data for model calibration, and a Solinst atmospheric pressure logger was deployed on land to measure and later correct for the atmospheric pressure.

The OBS voltage responses were converted to suspended sediment concentration (SSC) with a laboratory calibration using 12 known concentrations of sediment collected at the

deployment sites (mean r^2=0.93). Water samples were also collected adjacent to the instruments to directly validate the instrument calibration (r^2=0.90). The SSC was calculated by filtering 0.1–0.5 L of water through pre-weighed, 0.45 µm nitrocellulose membrane filters.

The bed shear stress, sediment flux, and tidal asymmetry were calculated from this instrument data. Bed shear stress was calculated using the Quadratic Stress Law:

$$\tau = \rho C_d \bar{u}_z{}^2 \quad (5.1)$$

where ρ was set to 1024 kg/m^3, C_d is the drag coefficient, and $\bar{u}_z$ is the mean velocity at height z above the bed. Along-channel velocity was defined as negative when it was directed out of the estuary. A median drag coefficient was calculated at each station and was assumed to apply over the full deployment. For both instrument-types, drag coefficients were only calculated using the following methodology during periods without wave activity. Median values for the drag coefficient at all stations fell within an accepted range of 0.0022–0.0037 and were consistent between instruments. This methodology of evaluating a drag coefficient during calm, steady conditions and applying it throughout the record ensured full temporal coverage, direct comparisons between stations, and tidal averaging.

For the Aquadopps, the drag coefficient was calculated using selected velocity profiles with steady flow conditions. The bed shear velocity was calculated by fitting a slope to the boundary-layer velocity profile using the Law of the Wall:

$$\frac{\bar{u}_z}{u_*} = \frac{1}{\kappa} \ln\left(\frac{z}{z_0}\right) \quad (5.2)$$

where u_* is the bed shear velocity, z_0 is the roughness length, and κ is the von Kármán constant, 0.41. The drag coefficient was calculated by assuming:

$$C_d = \frac{\bar{u}_z{}^2}{u_*{}^2} \quad (5.3)$$

(Sternberg, 1968). For the Vectors, which recorded within-burst velocity, the drag coefficient was calculated from the Reynolds Stress:

$$C_d = \frac{\overline{u'w'}}{\bar{u}_z^{\,2}} \tag{5.4}$$

where *u'* is the horizontal turbulent velocity and *w'* is the vertical turbulent velocity.

The critical shear stress for sediment resuspension was determined from previous studies in the estuary and nearby estuaries. The minimum estimate was 0.3 Pa (Harris et al., 2016), and the maximum estimate was 0.7 Pa (Stokes and Harris, 2015); the calculated bed shear stresses are compared to both thresholds. The slack, high-water duration was calculated as the time that T<0.3 Pa around high tide.

The instantaneous sediment flux was calculated per unit width as the SSC multiplied by the depth multiplied by the depth-averaged velocity. This method, which assumes that the SSC recorded at a single depth is representative of the depth-averaged SSC, has been effectively used in well-mixed, tidal-flat systems (Nowacki and Ogston, 2013). The depth-averaged velocity was determined for the Vectors by averaging the velocity profile calculated from the Law of the Wall. Cumulative sediment fluxes were computed by numerically integrating the instantaneous fluxes over time.

Drivers of sediment flux were examined by calculating the tidal asymmetry (γ) using the normalized sample skewness of property, *n* (Nidzieko and Ralston, 2012):

$$\gamma = \frac{\mu_3}{\mu_2^{\,3/2}} = \frac{1}{N-1}\sum_{i=1}^{N}(n_i)^3 \Big/ \left(\frac{1}{N-1}\sum_{i=1}^{N}(n_i)^2\right)^{3/2} \tag{5.5}$$

where μ_3 is the third moment about zero, μ_2 is the second moment about zero, and *N* is the total number of observations. The duration asymmetry (γ_d) was calculated from the water level ($n = \frac{dh}{dt}$ in Eqn. 5.5), and the velocity skew (γ_u) was calculated from the depth-averaged velocity ($n = u$

in Eqn. 5.5). A positive (negative) asymmetry indicates a stronger flood (ebb) tide and flood (ebb) dominance. When the duration asymmetry is directly correlated to velocity skew (γ_d-γ_u=0) the velocity skew is purely driven by the tidal-phase duration asymmetry. This will happen if tides are in quadrature, when the phase between water level and velocity is 90°. The slack-water asymmetry was not calculated because the majority of the estuary is dry at low tide. Instead, just the high-tide, slack-water duration was calculated.

Table 5.1. Locations and sampling schemes for instruments deployed in Waikaraka Estuary from 10–23 June 2019 (see Figure 5.1 for station locations).

Station	**Instrumentation and meters-above-bed (mab) elevation**	**Burst Interval (min)**	**Sampling Frequency (Hz)**	**Burst Duration (s)**
1 & 3	Nortek Aquadopp at 0.1 mab with 0.1 m bins; OBSs at 0.15 and 0.3 mab	2	1	60
	Onset Hobo Conductivity at 0.1 mab	5	-	-
2 & 4	Nortek Vector at 0.15 mab; OBS at 0.15 mab	8	8	128
Pressure	Solinst Levelogger at 0.1 mab and 2 mab (atmos.)	1	-	-
R1, R2	RBR Duo (wave and turbidity) at 0.15 mab	20	6	600

5.3.3 *Mapping mangrove coverage and estuarine morphology*

Instruments were deployed for two weeks in June 2019, during austral winter, to examine modern sediment transport in the estuary (Table 5.1, see Figure 5.1 for deployment locations). The mangrove extents and associated changes to channel morphology were mapped from historical aerial imagery collected between 1943 and 2016 (sourced from http://retrolens.nz and licensed by LINZ CC-BY 3.0). The images were georectified in ArcMap 10.0, and the channel was hand-

traced to calculate the sinuosity, i.e., the ratio of the total length of the channel over the straight-line distance from start to end (1.0 would be a straight channel).

In June 2019, substrate elevations along the tidal channel and at instrument stations were mapped with a GPS-RTK with centimeter-scale vertical accuracy. The modern bathymetry of the estuary was defined from this GPS-RTK survey and a 2015 LiDAR survey from Land Information New Zealand (LINZ, 2017), and this combined bathymetric dataset was used in the model (see Section 5.3.4). Unfortunately, there are no other LiDAR surveys for the entire estuary, limiting evaluations of morphologic change to characteristics measurable in aerial imagery (e.g., channel sinuosity).

5.3.4 *Delft3D numerical modeling*

A Delft3D numerical model of Waikaraka Estuary was used to examine modern hydrodynamic patterns and the impacts of varying mangrove extent on estuary infilling. Delft3D is a numerical modeling suite commonly used to examine shallow-water hydrodynamics, sediment dynamics, and morphodynamics (Lesser et al., 2004). The central, FLOW module solves the horizontal momentum equation, continuity equation, advection-diffusion equation, and applies a turbulence closure model. Here, the FLOW module was used without additional modules (i.e., sediment transport and morphology) to efficiently examine hydrodynamic patterns.

A rectilinear 5×5 m model grid was created, oriented parallel to the axis of the estuary, with smoothed bathymetry to remove discontinuities (Figure 5.1). The model was run in a depth-averaged, 2D mode, as is common when modeling shallow, well-mixed estuaries (Deltares, 2018). Mangrove trees, stumps, and pneumatophores were simulated using the built-in vegetation model, which represents vegetation as a collection of rigid cylinders with user-defined diameter, height, and spacing (Baptist et al., 2007; Deltares, 2018). This representation incorporates the effects of

vegetation both on flow and bed roughness, and has previously been used to successfully represent mangrove forests (Bryan et al., 2017; Horstman et al., 2014, 2015). Local mangrove characteristics were used to define the vegetation parameters (Table D.S1), and the mangrove extents in 2003 and 2019 were obtained from aerial imagery (see Section 5.3.3).

The water level and velocity in the model were calibrated with 2019 bathymetry and 2019 mangrove extent, using the June 2019 *in-situ* data to calculate the Brier Skill Score (Sutherland et al., 2004). The model was forced at the boundary using corrected tidal constituents. Initial tidal constituents were obtained from T_Tide harmonic analysis (Pawlowicz et al., 2002) of a 10-year record from the nearby Omokoroa tide gauge (Bay of Plenty Regional Council, Site CQ947053). The tidal constituents were then adjusted to match the water level in the model to the data (Table D.S2 and Figure D.S1). The velocity in the model was calibrated by adjusting the bed roughness to match the observed velocities. Similar modeling studies have used a uniform Manning roughness of 0.03 (Horstman et al., 2013b, 2015; Willemsen et al., 2016). However, the best skill score was found with a Manning roughness of 0.02 in the channel thalweg and 0.04 everywhere else. Note that the same Manning roughness was used in vegetated and unvegetated areas, and the addition effect of the mangroves was supplied by the built-in vegetation model. A uniform roughness of 0.03 was trialed, and these runs did not alter the conclusions (Text D.S1, Figure D.S2).

The model with 2019 bathymetry was run with eight mangrove extents (Table 5.2). The 2003 and 2019 mangrove forest coverage patterns were accurately represented. In addition, scenarios were run with no mangroves and mangroves placed to cover extents defined by elevation contours (see Figure 5.1 for mangrove extent maps). The maximum mangrove extent was set to

mean sea level (MSL), which corresponds to the physiological depth limit for mangrove growth (Horstman et al., 2018 and references therein).

The model was also run with recreated 1940s bathymetry (Text D.S2, Figure D.S3). The local rSLR from 1940 to 2019 was ~16 cm (Simon, 2018; Swales et al., 2016), and the tidal flats have accreted ~26 cm of sediment (Stokes, 2010). The 1940s bathymetry was created by uniformly raising the bed-elevation by 16 cm, lowering the tidal-flat-elevation by 26 cm, and then smoothing the transition from the channel thalweg to the flats. The recreated 1940 bathymetry was run with maximum and zero mangrove coverage (Table 5.2).

For each scenario, the model was allowed to equilibrate for two tidal cycles then run for two weeks (a spring-neap tidal cycle). Data were stored at 1 min intervals at the same locations where instruments were deployed in the estuary. Full model outputs were saved at 1-hour intervals.

Table 5.2. Summary of the Delft3D modeling scenarios. The mangrove extent was either defined by elevation contour or from aerial imagery in a specific year. The percent of the estuary area covered by mangroves in each scenario is provided. A "Y" indicates that the mangrove extent was run with the indicated bathymetry.

Mangrove extent, defined by elevation contour or year	Percent of estuary covered by mangroves	Run with 2019 bathymetry?	Run with 1940 bathymetry?
+0 cm	76%	Y	Y
+5 cm	63%	Y	
+10 cm	51%	Y	
+15 cm	43%	Y	
+20 cm	37%	Y	
2003	23%	Y	
2019	7%	Y	
None	0%	Y	Y

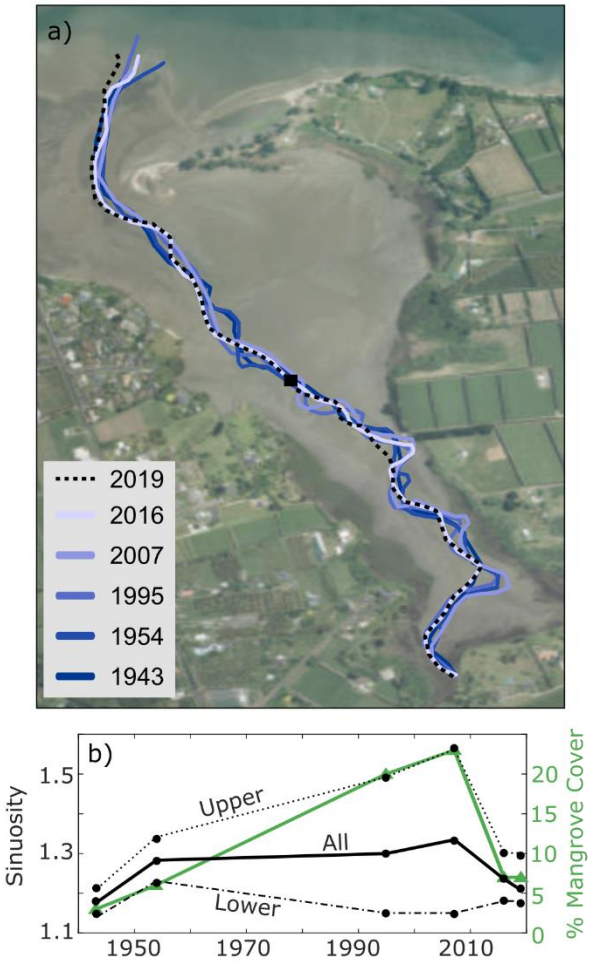

Figure 5.2. Channel sinuosity and mapping. The a) map of channel traced from aerial imagery from 1943 to 2019, and b) overall channel sinuosity (solid line, black circles) calculated from the channel trace with the percent mangrove coverage in the estuary (green triangles). The sinuosity for the Upper channel (dotted) and Lower channel (dot-dashed) are included, and the black square in a) marks the dividing location. Aerial image in map was accessed through ESRI ArcMap.

5.4 RESULTS

5.4.1 *In-situ observations of morphology and hydrodynamics*

The major features of the estuary morphology, including the mouth bar, tidal flats and number of tidal channels, did not change significantly between 1943 and 2019. Vertical changes to the bathymetry between 2015 and 2019 were within the error limits of the comparison between the

LiDAR survey and GPS-RTK measurements. The thalweg-channel sinuosity increased from 1.17 in 1943 to 1.33 in 2005, over the same time period that mangroves expanded from <1% coverage to 23% coverage (Figure 5.2). Sinuosity decreased to 1.21 in 2019, following mangrove removal. Changes in sinuosity were primarily in the upper estuary. The 2019 slope of the thalweg decreased spatially from ~2.8×10^{-3} m/m in the landward end of the estuary to ~0.5×10^{-3} m/m in the lower estuary.

The tidal prism of Waikaraka Estuary was comparable to the tidal volume of ~4.5×10^{5} m^3. The estuary drained completely at low tide, except the channel, and only Station 1 was continually submerged (Figure 5.3). The depth-averaged velocity in the channel decreased from 0.29 m/s at the mouth to 0.15 m/s at Station 4. The peak ebb velocity, ~0.7 m/s, was higher than the peak flood velocity, ~0.5 m/s, especially at Stations 1 and 2, close to the estuary mouth. Salinity varied between 26–28 over a tidal cycle (Figure 5.3a).

SSCs were comparably low at all stations. Concentrations varied with the tides, and the greatest concentrations, ~0.1 g/L, were observed during ebb and flood flows, especially at stations close to the mouth. The significant wave height was close to zero throughout most of the deployment, with the exception of a storm event on June 15th–18th. Wind blew from the northwest at 5–7 m/s and produced wave heights up to 0.1 m. The average SSC increased by 0.02 g/L over the corresponding tidal cycles.

The bed shear stress decreased dramatically up estuary from a peak of 1–2 Pa at Station 1 to <0.2 Pa at Station 4 (Figure 5.4). At stations closer to the mouth (1 & 2) the bed shear stress was consistently higher on the ebb tide (Figure 5.4e). This asymmetry decreased up estuary, with Station 1 having the largest difference between ebb and flood shear stress and Station 4 having no difference. The depth-integrated suspended-sediment flux was ebb dominant at Stations 1–3. Net

sediment export was greatest at Station 1, ~70 kg/tidal cycle, and decreased to approximately zero at Station 4 (Figure 5.4c).

The tidal duration asymmetry and velocity skew were calculated to examine Eulerian mechanisms for net sediment transport (Figure 5.5). The tidal duration asymmetry at Stations 1–3 was close to zero, indicating symmetric tidal duration. The duration asymmetry was slightly positive at Station 4, indicating shorter flood tides and flood dominance. The velocity asymmetry was negative at Stations 1–3, indicating stronger ebb tidal velocities, and close to zero at Station 4. The difference between the duration asymmetry and velocity skew was also negative at Stations 1–3, indicating that the velocity was not in quadrature with the tidal elevation. The difference at Station 4 was close to zero and was noisier due to the overall lower magnitudes. At all stations there was little spring-neap variability.

Velocity-stage diagrams (Figure 5.6) are useful for identifying peaks in velocity and turbidity related to bathymetry and tidal stage. The maximum ebb velocity at all stations occurred when the water level was close to 0 m, the elevation of the flats adjacent to the channel (Figure 5.6 a-d). The SSC peaked towards the end of the ebb tide at Stations 1–3, after the maximum ebb velocity. A lesser peak in SSC occurred during the onset of the flood tide. At Station 4 the SSC remained relatively constant over the tidal cycle.

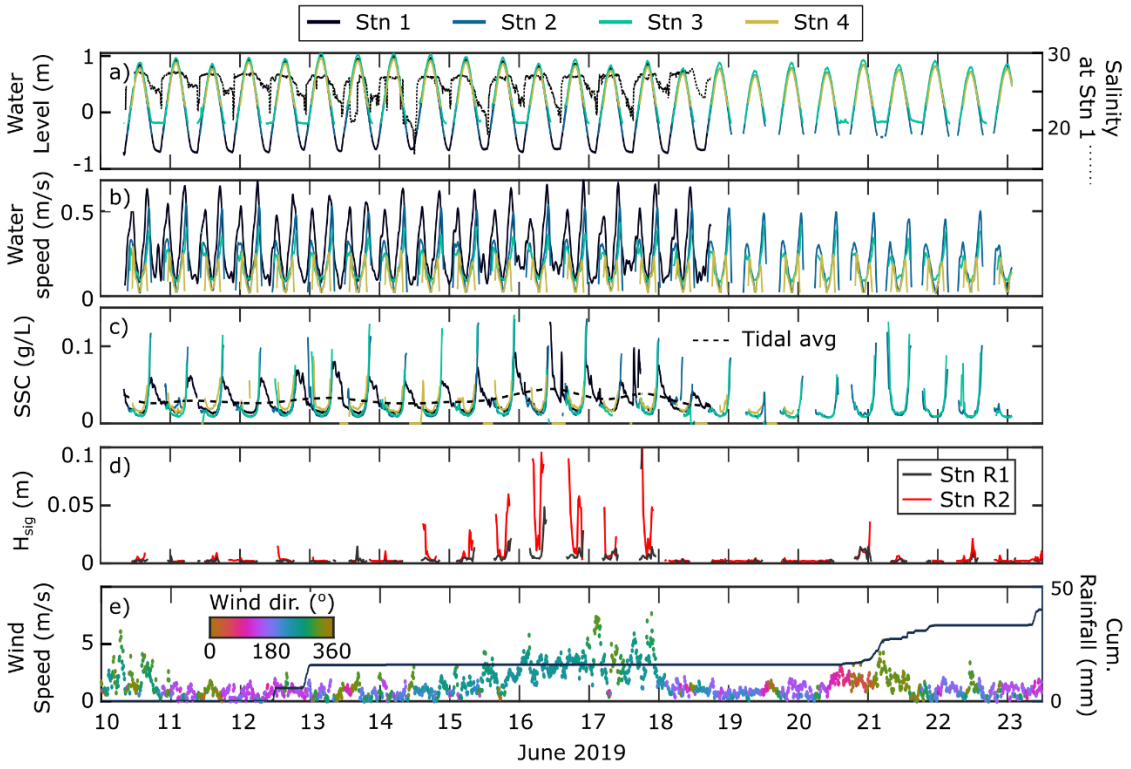

Figure 5.3. Raw instrument data. The observed a) water level and salinity, b) depth-averaged water speed, c) SSC, and d) significant wave height in Waikaraka Estuary in June 2019 (see Figure 5.1 for station locations). The e) wind speed, colored by direction, and the cumulative rainfall at Omokoroa, A-NZ (Bay of Plenty Regional Council, Site 2844).

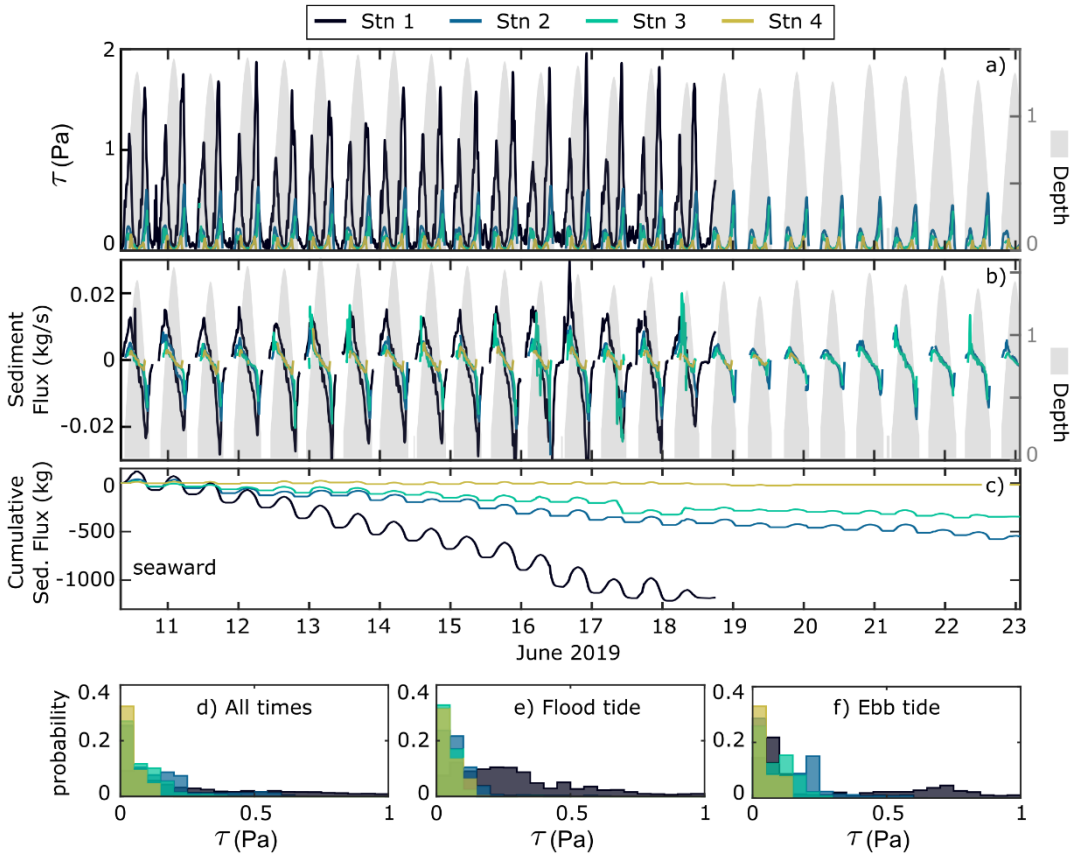

Figure 5.4. Net sediment flux in Waikaraka Estuary. The a) bed shear stress and water depth (shaded in gray), b) instantaneous sediment flux and water depth (shaded in gray), and c) cumulative sediment flux at Stations 1–4. Negative values are seaward. The histograms of bed shear stress by station are plotted for d) all times, e) flood tide, and f) ebb tide.

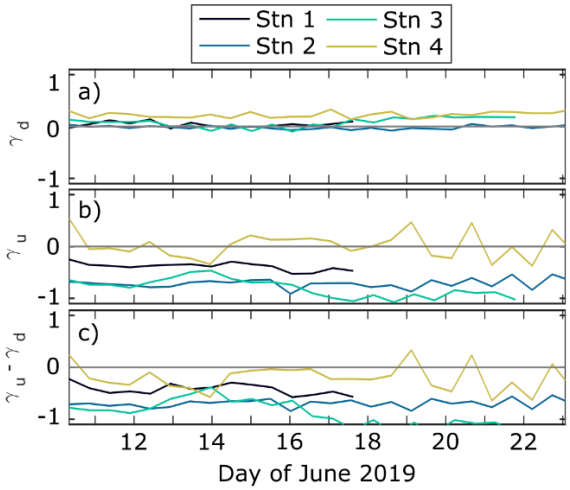

Figure 5.5. The a) tidal duration asymmetry, b) velocity skew, and c) difference between duration asymmetry and velocity skew at Stations 1–4.

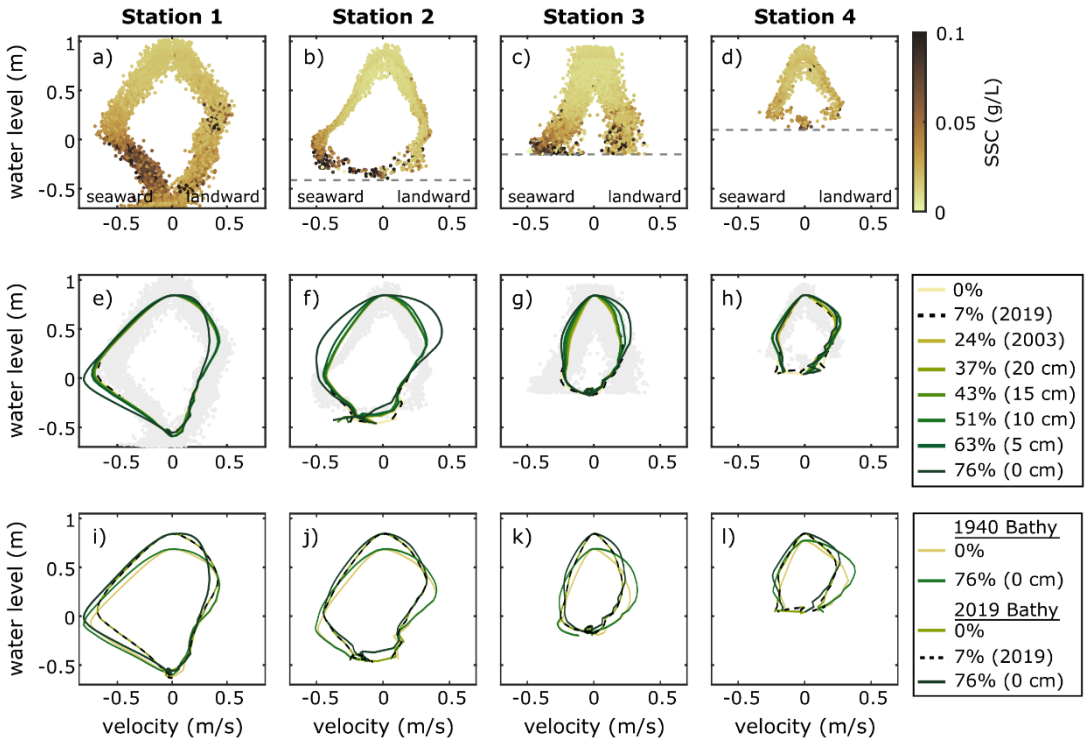

Figure 5.6. The a-d) observed, depth-averaged water velocity vs. water level (relative to MSL), colored by SSC, at Stations 1–4. Note the modest change in velocity scale at Station 1. The instrument elevation is indicated with a grey dashed line. The model results e-h) for depth-averaged water velocity vs. water level at varying mangrove extents (see Table 5.2 for details) with 2019 bathymetry. The observed data from a-d) are shown in the background with gray symbols for comparison. The model results i-l) for depth-averaged water velocity vs. water level at varying mangrove extents with 2019 and 1940 bathymetry.

5.4.2 *Numerical modeling: Flow, asymmetry, and shear stress*

Flow velocities modeled using the 2019 bathymetry and mangrove extent were consistent with instrument observations at Stations 1–4 (Figure 5.6 e-h, Table D.S2). The model captured the water level well at all stations; the model skill was lowest for the bed shear stress in the upper estuary, partly due to the overall lesser magnitudes and limited inundation period. Changing the mangrove extent while maintaining the 2019 bathymetry had little impact on the patterns of velocity in the

channel, especially at <76% coverage. The water velocity peaked during the ebb tide when the water level fell to the elevation of the adjacent tidal flats. In the model runs with increased mangrove extent, the magnitude of the peak ebb velocity increased by up to 0.1 m/s (Figure 5.6e). Water velocity before and after high tide increased by 0.15 m/s at Station 2 when mangroves were extended to the channel edge (model run with 76% mangrove coverage, +0 MSL).

Altering the bathymetry to represent conditions in the 1940s primarily changed the velocity at stations in the upper estuary (Figure 5.6i-l). The velocity pattern at Stations 1 and 2 were comparable to the modern flow, though compressed due to the lower water level, and there was still a distinctive ebb-pulse. At Stations 2–4, the peak flood velocities were greater by ~0.1 m/s with 1940 bathymetry than with 2019 bathymetry. At Stations 3 and 4 the peak flood velocity was greatest for the model runs with full mangrove coverage and 1940s bathymetry.

The duration asymmetry and velocity skew were calculated at Stations 1–4 for each of the model runs, and three representative runs are presented in Figure 5.7. For all mangrove extents, the duration asymmetry was close to zero at Stations 1 and 2 and was increasingly positive at Stations 3 and 4. The tidal wave was deformed as it progressed into the estuary, with a shorter flood than ebb tide. The velocity asymmetry was similar for 0–63% mangrove coverage: at Stations 1 and 2 it was strongly negative (ebb dominant), Station 3 was close to zero, and Station 4 was positive (flood dominant). The difference between duration asymmetry and velocity skew demonstrates that the velocity was not in quadrature with the tidal elevation, except at Station 4. These patterns were more exaggerated in the model with full mangrove coverage (76%). The velocity skew at Station 1 was strongly ebb dominant, while both Stations 3 and 4 became more flood dominant and were in quadrature with the tides.

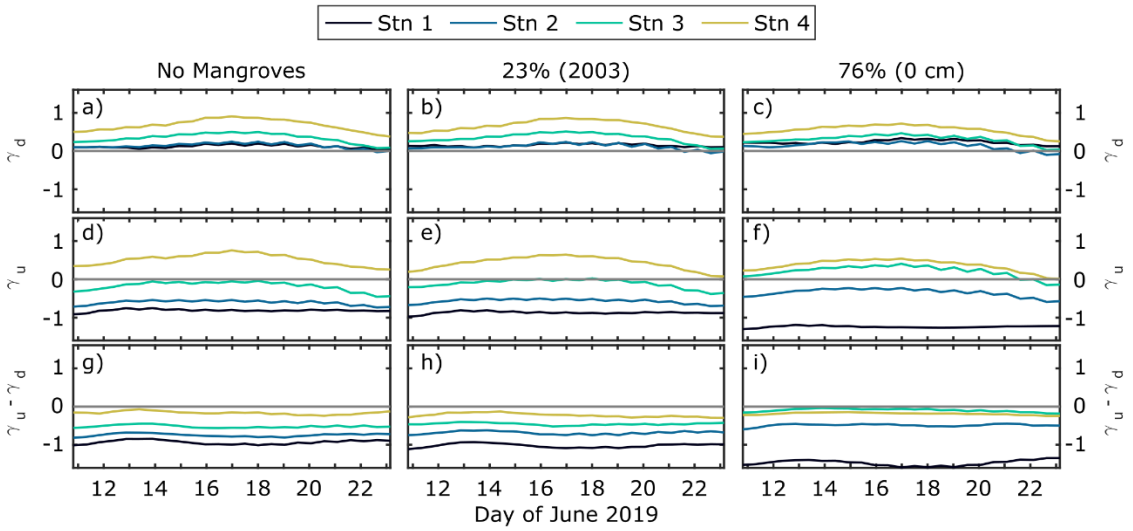

Figure 5.7. Asymmetry from model runs. The a-c) tidal duration asymmetry, d-f) velocity skew, and g-i) difference between tidal duration asymmetry and velocity skew at Stations 1–4 for model scenarios with no mangroves (left column), 2003 mangrove extent (middle column), and mangroves to 0 cm above MSL (right column), all with 2019 bathymetry.

Spatial sediment transport patterns were examined using the hourly full model outputs. The tidally averaged bed shear stress decreased into the estuary, with similar bed shear stresses observed along the channel for the model scenarios of 0–63% coverage (Figure 5.8a-g). The average shear stress only exceeded the 0.3 Pa minimum estimate of critical shear stress (Harris et al., 2016) within ~200 m of the mouth. In the lower estuary the maximum flood shear stress (0.9 Pa) was less than the maximum ebb shear stress (2.0 Pa). The ebb shear stress along the entire channel of the lower estuary consistently exceeded the greater 0.7 Pa estimate of critical shear stress (Stokes and Harris, 2015). In the upper estuary the maximum flood shear stress (0.63 Pa) was greater than the maximum ebb shear stress (0.29 Pa). Throughout the estuary, the tidal flats experienced a high-tide slack-water duration (<0.3 Pa) of 2.75 h. The water depth was 0.6–0.9 m, so particles with a settling velocity >9e-5 m/s would have sufficient time to reach the bed. Based

on estimates of settling velocity (Maggi, 2013), bioaggregates or individual particles >10 μm (fine silt) can be deposited.

At 76% mangrove coverage, the modeled patterns of shear stress along the thalweg shifted (Figure 5.8h). The maximum ebb shear stress increased at the mouth, peaking at ~2.8 Pa, and the maximum flood shear stress exceeded the maximum estimated critical shear stress throughout the lower estuary. In the upper estuary the maximum ebb and flood shear stresses were comparably low and generally did not exceed the minimum estimated critical shear stress. In addition, the slack water duration increased by ~30 mins per tidal cycle, providing marginally more time for fine sediment deposition.

The influence of mangrove extent on along-estuary sediment transport was examined by calculating the average difference in thalweg shear stress for each model run compared to the zero-mangrove model run (Figure 5.8i). The model runs for <40% coverage had no change in the maximum ebb or the tidally averaged shear stress, and the maximum flood shear stress increased by <0.05 Pa. Between 40–63% coverage, the shear stress increased by <0.05 Pa for all three parameters. At 76% coverage, the maximum ebb shear stress increased by 0.15 Pa. This increase was driven by the increase in shear stress in the lower estuary, whereas the shear stress in the upper estuary was minimally impacted by mangrove extent (Figure 5.8h).

Outside of the channel, general patterns of bed shear stress were also similar for model scenarios with 0–63% mangrove coverage, as demonstrated by the 23% coverage model results (Figure 5.9). During peak ebb and flood tides, the shear stress was greatest on the flats close to the mouth of the estuary. In the upper estuary, the shear stress was greatest at the channel edges instead of in the channel itself. The shear stress decreased on the flats away from the channel and did not exceed 0.2 Pa. When mangroves were extended to the channel edge, the shear stress increased in

the channel, while the maximum shear stress on the flat rarely exceed 0.3 Pa, even close to the channel edge (Figure 5.9c,f).

The potential for fine sediment retention was examined by calculating the slack water duration, or time that T<0.3 Pa, the minimum estimated critical shear stress, as a percent of total inundated time for each model grid cell (Figure 5.9 g-i). There were similar patterns for model scenarios with 0–63% mangrove coverage. The majority of the flats remained below the threshold for erosion when inundated, whereas regions close to the channel were mostly above the threshold. The channel was inundated continuously, but there was relatively little time over each tidal cycle when sediment in the channel bed could have been eroded. When mangroves were extended to the edge of the channel, the tidal flats were nearly always below the threshold of erosion, even close to the channel. However, the amount of time that sediment could be moved increased within the channel in the lower estuary.

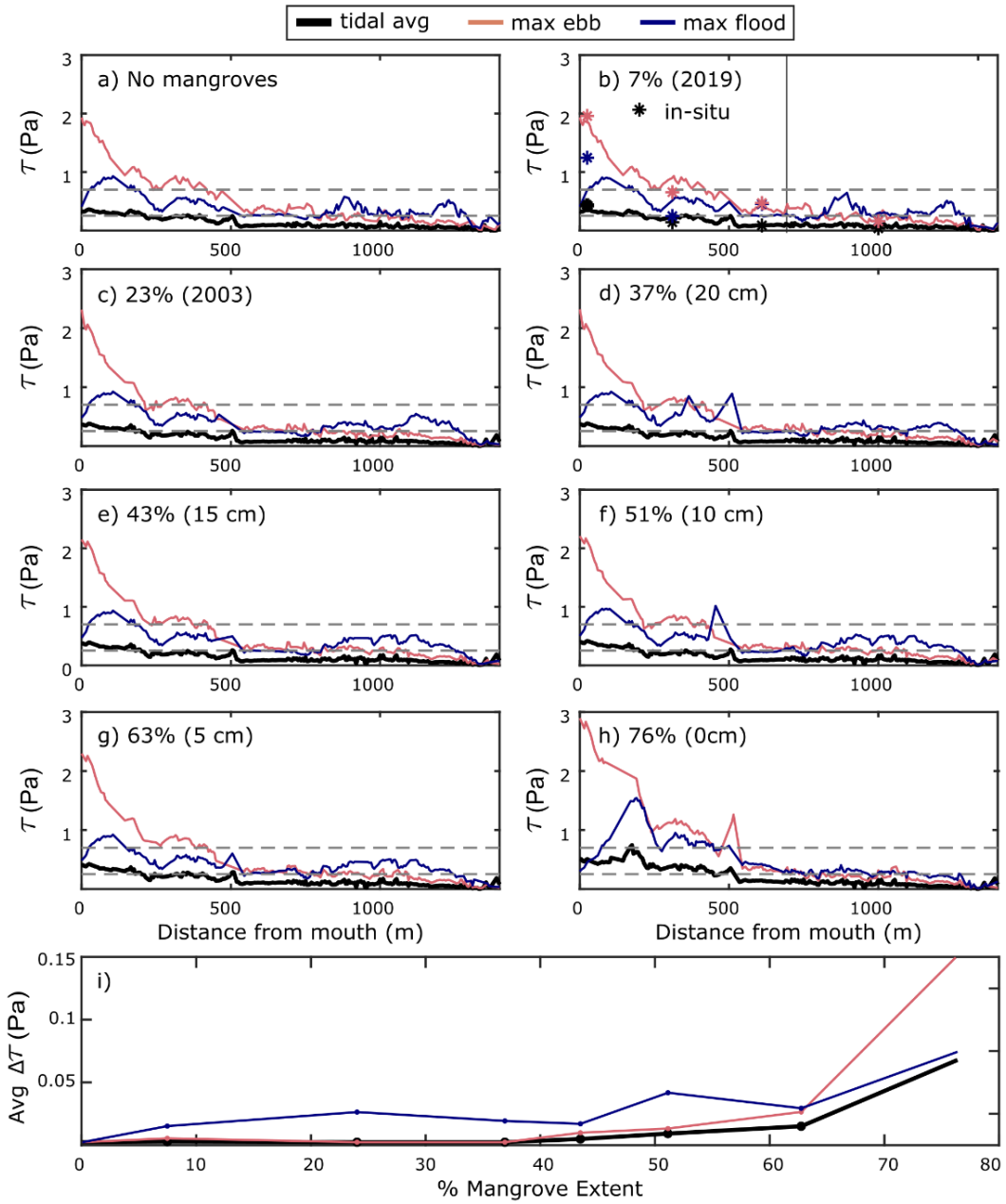

Figure 5.8. The a-h) average bed shear stress for modeled mangrove extents. The thick black line is the tidally averaged shear stress, the red line is the maximum shear stress during ebb tide, and the blue line is the maximum shear stress during flood tide. The dashed, gray lines are minimum and maximum estimates of the critical shear stress. In b), the model run corresponding to current mangrove extent, the in-situ observations are plotted as asterisks and the approximate dividing line between upper and lower estuary is indicated with a solid gray line. The i) average difference between the along-thalweg shear stress for each model run compared to the model run with no mangroves.

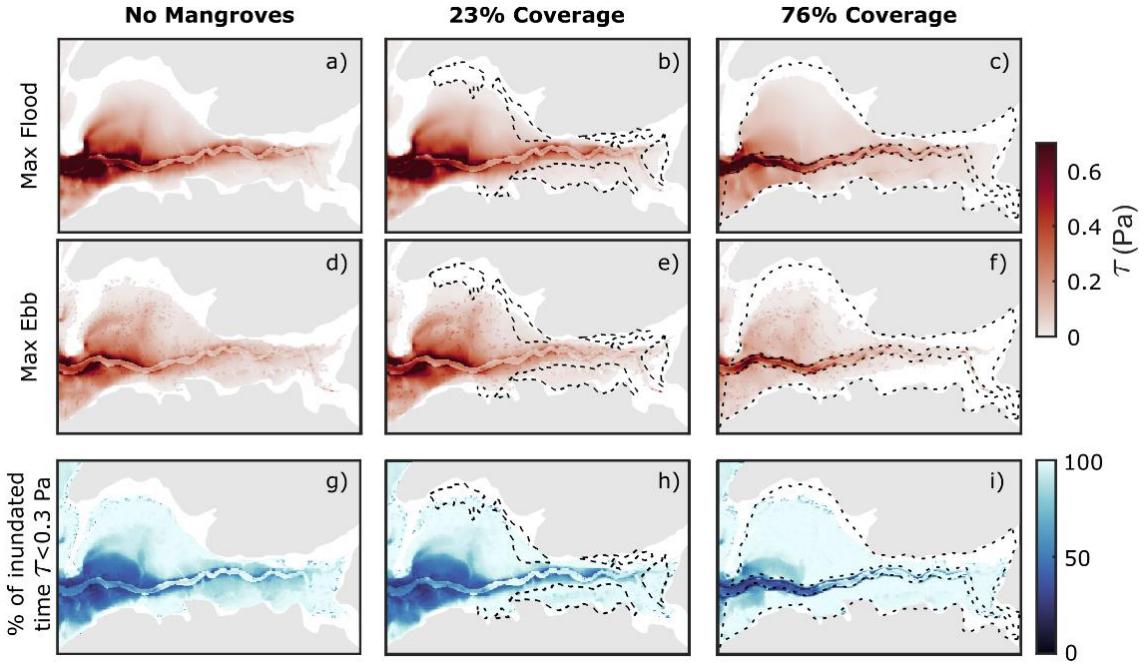

Figure 5.9. Maps of a-c) shear stress at maximum flood tide, d-f) shear stress at maximum ebb tide, and g-i) the percent of time that τ <0.3 Pa, the minimum estimate of critical shear stress, out of the total time that grid cell is inundated. The model scenarios shown are with no mangroves (left column), 2003 mangrove extent (middle column), and mangroves to 0 cm above MSL (right column). The mangrove extent is outlined with dashed black lines. The land above the +100cm MSL contour is shaded in gray.

5.5 DISCUSSION

In this study hydrodynamics, sediment transport, and estuarine morphology were assessed to determine the decadal-scale impact of mangrove removal. Field observations from the present-day were combined with numerical modelling of varying mangrove coverage and bathymetry to explore the interaction between mangroves and morphological evolution. These results are compared with other systems to identify the system parameters that are most useful for evaluating the impact of mangrove removal.

5.5.1 *Modern sediment dynamics in Waikaraka Estuary*

Waikaraka Estuary is representative of many quiescent embayments colonized by mangroves and presently appears to be close to dynamic equilibrium despite mangrove clearing in the early 2000s. However, even this relatively small and simple system has two morphologically and hydrodynamically distinct zones, the Lower and the Upper estuary, which respond differently to changes in vegetation and regional sediment supply.

The Lower estuary (extending from the mouth to the constriction point around Station 3, ~700 m into the estuary) exhibits many of the typical characteristics of a stable basin dominated by extensive tidal flats. In the channel, flow is strongly ebb dominant (Figure 5.4 and Figure 5.6) due to the ebb pulse as the water level falls to the level of the channel edge (Figure 5.5). The presence of an ebb pulse is indicative of an infilled intertidal morphology (Friedrichs, 2010); tidal channels are maintained by scouring during the pulse while deposition can still occur on the flats (Nowacki and Ogston, 2013).

During the June 2019 observations, there was net sediment export through the channel over tidal timescales (Figure 5.4). Sediment export significantly increased from Station 2 to Station 1, suggesting that much of the exported sediment is sourced from the immediately adjacent tidal flats, where the highest shear stresses were observed (Figure 5.8), rather than Minden Creek or the Upper estuary. However, this rate of sediment export would lead to a negligible <1 mm per decade of vertical erosion on the flats, assuming the observed 70 kg/tidal cycle remains constant, indicating that the estuary is close to equilibrium. As such, the local rSLR, ~2.3 mm/y, will be a more important driver of change than this measured sediment load. It is also possible that the rate of sediment export and sediment accretion observed during this austral winter represents seasonal

cycling, not a consistent annual trend, as occurs in a variety of tidal embayments (Andersen et al., 2005; Boldt et al., 2013).

On the tidal flats, there was also a high probability of fine-sediment deposition during the 2.75 h slack high-tide, and mud deposition was observed on sedimentation plates deployed on the upper tidal flats (D. Stokes, unpublished data). This depositional pattern is common in infilled systems throughout the world, which also tend to have coarser sediment in scoured channels and on lower flats and finer sediment on upper flats (Boldt et al., 2013; Friedrichs, 2011; Mai and Bartholomä, 2000). Deposited sediment is retained, suggesting that tidal interactions with bathymetry are sufficient to result in estuary infilling, even in the absence of vegetation (Figure 5.6, Figure 5.7, Figure 5.8). The historical estuary infilling is discussed in greater detail in Section 5.2.

Considering the high probability of deposition and retention, the limiting factors for sediment accumulation are accommodation space and SSC during flood tides. SSC was typically <0.05 g/L in the estuary, and accumulation appears to be just keeping pace with the current rSLR of 2.3 mm/y (Simon, 2018; Swales et al., 2016). However, changes in SSC in Tauranga Harbor or Minden Creek would have a large impact on sediment deposition rates in the Lower Estuary. The elevated accumulation rates in the early 1900s are attributed to nearby mining activities. This previous period of high deposition suggests that future episodic sediment-delivery events, such as nearby landslides (Moon et al., 2015), could also result in short-term increases in sediment deposition.

Wave activity can drive sediment transport in systems with extensive, shallow tidal flats (e.g., Hunt et al., 2015), however Waikaraka Estuary is a quiescent environment with waves typically <0.1 m (Figure 5.3). The two-week observational record did not capture a major event

with storm surge or flooding, though a minor weather event blew winds directly into the estuary during the study, representing the conditions with highest probability of wave generation. During this event, the average SSC increased at stations in the Lower estuary, yet even under these optimal conditions the sediment export only marginally increased (Figure 5.3). The largest storm events in Tauranga Harbor bring winds from the southwest, perpendicular to the axis of Waikaraka Estuary. Unlike energetic environments, such as the Firth of Thames, A-NZ (Swales et al., 2015) or the Guianas coast (Brunier et al., 2019), these types of events likely do not contribute substantially to the annual sediment budget in comparison to the persistent tidal processes. Future studies should explore the relative importance of rare and major storms compared to continuous tidal processes in protected embayments.

In contrast to the Lower estuary, the Upper estuary is characterized by a muddy bed and significant sediment retention consistent with many quiescent embayments (Friedrichs, 2011). Water velocities were slower here, and the shear stress in the channel was generally less than even the minimum estimate of critical shear stress (Figure 5.8). Weak flood dominance driven by tidal deformation was nearly balanced by the weak ebb-pulse from the flats (Figure 5.5), and there was negligible net sediment transport over tidal or spring-neap timescales (Figure 5.4). As in the Lower estuary, the tidal flats in the Upper estuary are only inundated around high tide when the bed shear stress is always below the threshold of erosion. Overall, these hydrodynamic conditions are consistent with the extensive deposits of fine sediment in the Upper estuary (Glover et al., 2020). Sediment retention in the Upper estuary is further promoted by the remaining stands of mangroves.

Overall, this simple system displays the tidal asymmetry and fine-sediment retention common in many vegetated and unvegetated, quiescent embayments. The Lower and Upper zones of the estuary are both infilled environments close to dynamic equilibrium. The observations and

numerical modeling together demonstrate that the mangrove coverage reduction from 23% to 7% in 2003 did not significantly alter sediment transport processes. Consequently, mangrove removal was not an effective method for restoring a sandy bed over the past decade, and the estuary is not conditioned to change significantly over the next decade.

5.5.2 *Which came first, the mangroves or the mud?*

The second goal of this study was to examine the role of mangroves in the morphological evolution of Waikaraka Estuary, as a representative quiescent, mesotidal environment. Comparing model results with varying bathymetry and mangrove coverage allowed us to reconstruct historical hydrodynamic regimes in the estuary and examine the relative importance of mangrove coverage.

When the bed elevation was lowered to approximate the conditions in the 1940s, the hydrodynamic patterns in the channel became more exaggerated, regardless of the mangrove coverage (Figure 5.6). The flow in the Upper estuary became more strongly flood dominant (Figure 5.6i-l), while the inundation period on the tidal flats was comparable to modern conditions. This suggests that the estuary would have efficiently imported sediment, aggrading towards the present equilibrium profile prior to mangrove colonization. Similar sediment-import mechanisms have been described in much larger estuaries. For example, numerical modeling of the ~50-km-long Darwin Harbor, Australia demonstrated that lowering the tidal-flat elevation increased flood dominance even in the absence of mangroves (Li et al., 2012). If mangroves had rapidly expanded to completely cover Waikaraka Estuary in the 1940s, the existing sediment retention patterns would have been further enhanced (Figure 5.6). With full coverage, the Upper estuary was more strongly flood dominant and shear stress was lower on the tree-covered flats. However, this enhancement would have required an improbably rapid mangrove expansion and coverage.

Overall, the 1940s-bathymetry model runs support the hypothesis that mangroves can opportunistically colonize environments produced by abiotic, tidal processes.

Similarly, model results from runs using 2019 bathymetry suggest mangroves had little impact on hydrodynamics as they expanded. Changing mangrove coverage between 0–63% coverage (to +5 cm MSL) had little impact on hydrodynamics related to either coarse or fine sediment dynamics; the peak velocity, inundation period, residence time, and bed shear stress did not change significantly (Figure 5.6). It should be recognized that the velocity and bed shear stress in the mangroves was not directly validated in the model, and therefore model results in these regions should be treated with some caution. Modeling mangroves as a uniform roughness element can lead to overestimates of bed shear stress (Horstman et al., 2018a) and mangroves may alter erodibility through the development of biofilms (Woodroffe et al., 2016). However, the velocity values were consistently low throughout the Upper estuary, regardless of mangrove coverage. Small changes to these low values are unlikely to dramatically alter sediment dynamics throughout the estuary. Furthermore, tidal asymmetry in the main channel, which would drive net sediment transport through the estuary, did not change (Figure 5.7).

The stability in hydrodynamic conditions with changing mangrove extent was unexpected, considering much of the current literature emphasizes the complex interactions between mangroves and flow (e.g. Alongi, 2002; Friess et al., 2019). However, this finding is consistent with mangrove expansion in fish ponds infilled by agricultural runoff in Hawaii (Möhlenkamp et al., 2018) and mangrove arrival post estuary infilling in the energetic Firth of Thames, A-NZ (Swales et al., 2007). In the early 1900s, sediment accumulation rate exceeded rSLR in Waikaraka Estuary, providing new intertidal habitat for mangroves. It appears that mangroves can act as

opportunists in both energetic and quiescent environments, enhancing pre-existing sedimentation processes.

In the present study, mangroves only significantly altered the along-estuary trends in hydrodynamics once they reached maximal extent at the channel margins (76% coverage). This mangrove extent is similar to the many mature mangrove forests in tropical environments drained by unvegetated tidal channels, and the model results are consistent with the velocity patterns observed in these natural systems (e.g. Aucan and Ridd, 2000; Horstman et al., 2013; McLachlan et al., 2020). In the Lower estuary, the ebb pulse in the channel was accentuated due to the enhanced friction on the flats, while the channel velocity in the Upper estuary remained low (Figure 5.6 and Figure 5.8). The average bed shear stress decreased on the tidal flats, primarily because mangroves occupied the region within 250 m of the channel where shear stress was previously high (Figure 5.9). Similar patterns of tidal asymmetry have been observed in the nearby Whitianga Estuary, A-NZ, where mangroves cover the tidal flats to the edge of a deeply-incised channel (Horstman et al., 2021). In addition, the slack water duration increased by ~30 mins per tidal cycle, providing marginally more time for fine sediment deposition. These hydrodynamic conditions promote a stable, infilled morphology: fine sediment is pumped landward and retained on forested tidal flats, while channels are maintained by ebb scouring. However, these patterns only developed once mangroves reached maximal extent, emphasizing the role of mangroves as opportunists.

Though the modeling demonstrates the minimal impact of mangroves on hydrodynamics, mangroves can also impact sediment dynamics by increasing bed stability. One manifestation of this increased stability is tidal channel sinuosity (Figure 5.2). In the Upper estuary, the channel sinuosity increased between 1940 and 2003, over the same period that mangroves expanded to

cover the Upper channel margins (Figure 5.1). Though the hydrodynamics were not significantly different in 2003 (Figure 5.6), the proximity of vegetation to the channel edge would have promoted sediment retention and stability along the channel margins, increasing sinuosity. Similar depositional feedbacks have been observed in salt marsh (Hood, 2006; Larsen, 2019) and fluvial landscapes (Lazarus and Constantine, 2013). In contrast, mangroves did not reach the channel margin in the Lower estuary and the sinuosity did not increase.

The impact of mangrove coverage on the morphology of the tidal flats is less clear because the vertical changes to bathymetry cannot be measured in aerial imagery. An average drop in surface elevation of 14 mm/y was observed in zones cleared of mangroves in 2005, immediately following mangrove removal (Stokes et al., 2009). However, elevation change was not detectable between the 2015 LiDAR and 2019 GPS survey, suggesting that this erosional trend did not continue linearly. The persistence of undecomposed, subsurface roots may provide stability to the cleared tidal flats, slowing morphologic change (Stokes et al., 2009). Overall, the changing channel sinuosity and stable tidal flats together suggest that the subsurface mangrove roots may be as important for morphology as the hydrodynamic impact of the pneumatophores and tree trunks.

5.5.3 *Predicting change following mangrove removal*

Sanctioned and unsanctioned mangrove removal is occurring throughout the world. In most tropical regions, mangroves are removed for agricultural expansion or infrastructure development (Friess et al., 2019), and there is no desire to change intertidal morphology. In A-NZ and Hawai'i, mangrove removal is often motivated by a desire to reduce fine-sediment retention in estuaries and restore bivalve habitat (Horstman et al., 2018b; Möhlenkamp et al., 2018), as it was in Waikaraka Estuary. In either case, stakeholders need to predict patterns and rates of estuarine sediment transport following removal.

The mismatch between restoration objectives and *in-situ* conditions at Waikaraka Estuary highlights the need for site-specific evaluation of tidal dynamics, wave climate, rSLR and sediment characteristics. Prior to mangrove removal, Waikaraka Estuary was at a stable, infilled state. The hydrodynamic regime was not conducive to sediment export, especially in the Upper estuary, and the bed has not become significantly coarser in the >10 years following mangrove removal. Furthermore, the estuary is still susceptible to future infilling, as sediment transported into the estuary is frequently retained and accommodation space is continually generated by local rSLR. The importance of changes to regional sediment supply has also been highlighted in tropical studies of mangrove sediment retention with species other than *Avicennia*, which have different root structures (Willemsen et al., 2016). In Mangawhai Harbor, A-NZ, a catchment change increased fine-sediment delivery to a region where mangroves had been removed, which effectively counteracted the restoration (Alfaro, 2010). Infilled environments with similar hydrodynamic conditions are also unlikely to change dramatically following mangrove removal. The conditions observed in Waikaraka Estuary are not unique but are representative of the fundamental processes that result in infilled quiescent embayments (Friedrichs, 2011)..

Coasts with less stable morphology, such as bluffs or atolls, may shift into a positive feedback regime that promotes erosion following mangrove removal or loss, as has been observed along the Guianas coast (Brunier et al., 2019) or Turneffe Atoll, Belize (Hayden and Granek, 2015). In addition, waves can strongly impact morphologic stability, and it is well known that mangroves attenuate wave and surge energy (Massel et al., 1999; Mazda et al., 2006; Montgomery et al., 2019). Mangrove removal is most often associated with dramatic change when sites are either consistently energetic or exposed to seasonally-varying energetics (Besset et al., 2019; Brunier et al., 2019; Granek and Ruttenberg, 2007; Swales et al., 2015; Winterwerp et al., 2013).

Conversely, infilled, enclosed embayments are protected from wave energy, and the quiescence is a significant contributor to stability and slow 'restoration' following mangrove clearing (Stokes et al., 2016).

Finally, roots persist long after the surface expressions of mangroves have been removed, and root decomposition has been highlighted as a critical component of successful estuary restoration (i.e. fine sediment export and soil geochemistry restoration) (Bulmer et al., 2017a; Stokes and Harris, 2015; Sweetman et al., 2010). The specific subsurface root density and rates of sediment retention vary with mangrove species and environmental conditions, including latitude (Krauss et al., 2003). Global estimates of mangrove root decomposition are 1–3.6 years (Ouyang et al., 2017), however previous studies in A-NZ have found substantially longer timescales for root decomposition (Bulmer et al., 2017a; Lundquist et al., 2014), and roots have persisted for >10 years in Waikaraka Estuary (D. Stokes, unpublished data). Furthermore, feedbacks between root decomposition, bed subsidence, and bed compaction may cause non-linear changes in sediment dynamics following mangrove removal especially in areas with high rates of rSLR (Woodroffe et al., 2016), including the development of new tidal channels (Vandenbruwaene et al., 2013).

There is a wealth of literature on the subject of mangrove ecogeomorphology, yet many management recommendations are based on generalized mangrove or estuary characteristics (Dencer-Brown et al., 2018; Horstman et al., 2018b), which may overemphasize the role of mangroves in hydrodynamics. It is important to make site specific assessments of the role of mangroves prior to planting or removal. The small-scale variability in response within Waikaraka Estuary highlights the value of multiple measurements and site-specific evaluations within an embayment. Finally, it is important to note that the considerations described here only relate to sediment dynamics. The impact of mangrove removal on other ecosystem services, such as bird or

fish habitat and carbon sequestration (Bulmer et al., 2017b; Dencer-Brown et al., 2018; Pérez et al., 2017) or recreation, should also be locally assessed.

5.6 CONCLUSION

Identifying the fundamental connections between mangroves, sediment dynamics, and morphology is key to understanding how intertidal environments will respond to changes in mangrove extent. Here, *in-situ* observations were integrated with numerical modeling to examine the response of a quiescent, mesotidal embayment to changing mangrove extent.

Overall, mangrove removal was not an effective method for restoring a sandy bed in Waikaraka Estuary because changes in mangrove extent did not significantly alter the pre-existing hydrodynamic patterns. The modern estuary was close to dynamic equilibrium prior to mangrove removal and remained in equilibrium afterwards. During typical winter conditions some fine sediment is exported from the Lower estuary by ebb-dominant flows in the tidal channel and elevated bed shear stress close to the estuary mouth. In the Upper estuary, fine sediment is trapped due to flood-dominant flows and low shear stresses. The lack of wave energy limits sediment resuspension, though a major storm event was not observed. Similar infilled, quiescent estuaries are also unlikely to change following mangrove removal.

The numerical modeling demonstrated that Waikaraka Estuary infilled over the past century due to tidal asymmetry. Quiescent tidal basins are susceptible to infilling with a regional change in sediment supply because sediment imported into the estuary has a high probability of being deposited and retained. In this environment, mangroves acted as opportunistic colonizers and stabilizers, rather than engineers of infilling. The classic, mangrove-forest hydrodynamic patterns that promote sediment import are not established until the mangrove forest has reached

an extensive and mature coverage, especially at the estuary mouth. However, the morphological evolution of Waikaraka Estuary also suggests the importance of subsurface root structures. Mangrove roots stabilize sediment, which enhanced sediment retention and channel sinuosity in the Upper estuary despite removal of aboveground vegetation. Consequently, the decay rate of roots will impact the timescale of change following mangrove removal.

This study highlights the importance of considering site-specific parameters and intra-estuary variability when assessing the impact of mangrove removal. Intertidal sediment dynamics are controlled by the complex interplay between tide and wave processes, sediment supply, existing morphology, and mangrove characteristics. Qualitative assumptions about the response of an estuary to changes in vegetation are likely to lead to unexpected or unwanted outcomes.

Chapter 6. SUMMARY

The geomorphology of the river-ocean interface is governed by interactions between fluvial, marine, and ecological feedbacks that impact the transport and deposition of sediment. The four studies presented here have provided new insights into coastal sediment dynamics and resulting morphology over tidal to century timescales at centimeter to kilometer scales. The first two chapters examined relatively natural environments while the second two chapters considered the impact of mangrove removal. Together these studies demonstrate that natural feedback processes create complex coastal landforms where human intervention often leads to unexpected results.

The first study examined variability in sediment transport and retention within the Ayeyarwady Delta, Myanmar. The tidal-to-estuarine reaches of three representative distributaries were investigated using longitudinal and tidal-transect surveys during the high-flow and low-flow monsoon seasons. The eastern Yangon distributary empties into the sheltered, macrotidal Gulf of Mottoma while the central Bogale and western Pathein distributaries are more exposed to seasonal waves.

During high flow, the upper delta retained 20–60% of the mainstem sediment load, while the lower distributaries were tidal rivers exporting sediment. Suspended-sediment concentrations (SSC) was consistent across all three distributaries (0.2–0.4 g/L). During low flow, the lower distributaries were all partially mixed estuaries with little net discharge. However, SSC increased to >1 g/L in the Yangon distributary, remained constant in the Bogale distributary, and decreased in the Pathein distributary compared to high flow. This difference was driven by offshore sediment supply; fine sediment is retained near the mouth of the Yangon and advected away from the

western distributaries. Future changes to coastal sediment delivery (i.e., mainstem damming) may cause non-uniform impacts due to these differing distributary processes. Comparison with the similar Mekong and Ganges-Brahmaputra Deltas, which are also tide-dominated, monsoon systems, demonstrated that nearshore sediment residence time is controlled by coastal orientation, the timing of discharge with respect to ocean conditions, and tidal amplification.

The second study examined sediment dynamics in Meinmahla Island, a mangrove-forested island in the Bogale distributary. Tide-dominated deltas have multiple, interconnected distributaries and are, consequently, composed of inter-related land masses and islands. Mid-channel islands play an important and poorly understood role in these systems. Field measurements of morphology, hydro- and sediment-dynamics during 2017–2019 provided insight into the fundamental processes governing the evolution of a mid-channel island. Water depth, salinity, and turbidity were monitored semi-continuously, and velocity profilers with turbidity and salinity sensors were deployed seasonally in low-connectivity (dead-end) and high-connectivity (flow-through) tidal channels of the island. The morphologic evolution was evaluated using grain size, ^{210}Pb geochronology in 1-m-long sediment cores, remote sensing, and channel surveys.

Ebb-dominant, low-connectivity channels along the island exterior consistently imported sediment year-round to the land surface. Yet, these exterior, low-connectivity channels did not provide enough sediment to maintain the observed ~0.8 cm/y accretion rate, and most of the sediment delivery occurred via interior, high-connectivity channels. Interior channels retained water masses that were physically distinct from the water in the distributary, and estuarine processes at the channel mouths imported sediment into the island. Sediment was sourced to the island from upriver in the wet season and from offshore in the dry season, as the Bogale estuary shifted seasonally within the distributary due to river discharge. The salinity and biogeochemistry

of the distributary water was likely significantly altered by interactions with groundwater in the island interior. The largest interior channels have remained remarkably stable while the island has aggraded and prograded over decadal timescales. However, a high-connectivity channel has responding to a drainage-network change by narrowing and shoaling. Overall, mid-channel islands trap sediment and associated nutrients at the river-ocean interface, and interior channel networks can evolve in response to perturbations while the island continues to aggrade and prograde.

The third study compared Meinmahla Island to a nearby, un-leveed agricultural field. The Ayeyarwady Delta, Myanmar has been extensively deforested for agriculture but has few levees/polders in comparison to similar megadeltas (e.g., Ganges-Brahmaputra and Mekong). Coastal management requires a fundamental understanding of the impacts of different styles of agricultural development. The relative resilience to subsidence of a 40-year-old agricultural field and mangrove-forest preserve were compared. At both sites, water velocity and turbidity were measured in dead-end channels, topography was mapped, and sediment cores were collected in 2018–2019. Accumulation rates were calculated from the cores using ^{210}Pb and ^{137}Cs.

There was a net landward sediment flux of 0.001–0.004 kg/m/s in both environments due to sediment trapping by dense vegetation. Accumulation rates were on the order of 0.7 cm/y in the forest. The land-surface elevations were equivalent, accounting for the slope of the delta, suggesting that the field is aggrading at the same rate as the forest. Overall, both the mangrove forest and un-leveed field appear to be keeping pace with SLR by tidally retaining sediment. Crops such as rice may provide similar sediment trapping as mangrove or salt-marsh vegetation. Consequently, un-leveed agricultural fields are not as susceptible to rapid subsidence as leveed fields, and the impacts of deforestation and levee construction on relative SLR should be considered separately. The continued absence of levees may be critical for the Ayeyarwady Delta.

The final study examined the evolution of an embayment in New Zealand as mangrove coverage changed over ~80 years. Mangroves are often considered integral engineers of morphologic evolution, yet they can also opportunistically respond to morphologic change caused by abiotic sedimentary processes. Consequently, predicting the response of individual estuarine environments to changes in mangrove extent is challenging, especially over decadal or century timescales. In Waikaraka Estuary, New Zealand the impact of mangrove extent was explored using in-situ observations and numerical modeling. Mangroves expanded in the estuary from 1940 until a removal program began in 2005 with the goal of reducing fine sediment and restoring bivalve habitat. In June 2019, water velocity, turbidity, wave height, and bed-sediment grain size were measured at multiple sites to identify how sediment dynamics in the estuary were responding to removal. The bed sediment was predominantly sandy in the lower estuary and muddy in the upper estuary. Flow in the lower estuary was ebb dominant resulting in net sediment export, while flow in the upper estuary was weakly flood dominant resulting in sediment import. Fine sediment is unlikely to be flushed out of quiescent estuaries even after mangrove removal.

A Delft3D numerical model calibrated with the in-situ data showed that tidal asymmetry, velocity skew, and peak ebb-tide shear stress were not significantly altered by varying the mangrove extent between the 2005 maximum and complete removal. Mangroves did not significantly impact flow in this system; instead, the hydrodynamics and net sediment transport were controlled by bathymetric interactions with the tide. In model runs with mangroves covering all tidal flats, the water velocity on the intertidal flats decreased while the peak ebb-tide velocity in the main channel increased, indicating that the potential for fine-sediment export may actually decrease with mangrove removal. These results emphasize the role of mangroves as opportunistic colonizers, not engineers, and the importance of considering site specific parameters when

planning mangrove removals. Qualitative assumptions about the role of mangroves in coastal morphology is likely to lead to unexpected and possibly undesirable outcomes.

These four studies provide insight into the complex sediment dynamics of the river-ocean interface and reveal common themes. First, sediment transport from source-to-sink is a non-linear pathway. In deltas, sediment is continually recycled between the distributaries, floodplains, and mid-channel islands. Furthermore, sediment delivered to the coastal ocean can be reimported to deltas or embayments. Coastal sediment residence time is consequently controlled by complex ecogeomorphic feedbacks and seasonal variability. These morphologic feedbacks and transport pathways increase the resilience of coastal ecosystems and landforms to sea-level rise. Human alteration to coastal environments should strive to maintain natural pathways for sediment transport as much as possible. Finally, sediment dynamics can vary significantly within a system, both at the scale of a 1-km-long embayment and a 250-km-wide megadelta. In-situ observations are always limited, and coastal policies must rely on generalized information about systems. Yet, policymakers should carefully consider the impact of within-system variability.

BIBLIOGRAPHY

Alexander CR, Nittrouer CA, DeMaster DJ, Park Y-A, Park S-C. 1991. Macrotidal mudflats of the southwestern Korean coast: A model for interpretation of intertidal deposits. Journal of Sedimentary Petrology **61** : 805–824.

Alfaro AC. 2010. Effects of mangrove removal on benthic communities and sediment characteristics at Mangawhai Harbour, northern New Zealand. ICES Journal of Marine Science **67** : 1087–1104.

Allison MA, Dallon Weathers H, Meselhe EA. 2017. Bottom morphology in the Song Hau distributary channel, Mekong River Delta, Vietnam. Continental Shelf Research **147** : 51–61. DOI: 10.1016/j.csr.2017.05.010 [online] Available from: http://dx.doi.org/10.1016/j.csr.2017.05.010

Allison MA, Kepple E. 2001. Modern sediment supply to the lower delta plain of the Ganges-Brahmaputra River in Bangladesh. Geo-Marine Letters **21** : 66–74. DOI: 10.1007/s003670100069

Alongi DM. 2002. Present state and future of the world's mangrove forests. Environmental Conservation **29** : 331–349. DOI: 10.1017/S0376892902000231

Alongi DM. 2008. Mangrove forests: Resilience, protection from tsunamis, and responses to global climate change. Estuarine, Coastal and Shelf Science **76** : 1–13. DOI: 10.1016/j.ecss.2007.08.024

Alongi DM. 2014. Carbon cycling and storage in mangrove forests. Annual Review of Marine Science **6** : 195–219. DOI: 10.1146/annurev-marine-010213-135020

Andersen TJ, Lund-Hansen LC, Pejrup M, Jensen KT, Mouritsen KN. 2005. Biologically induced differences in erodibility and aggregation of subtidal and intertidal sediments: A possible cause for seasonal changes in sediment deposition. Journal of Marine Systems **55** : 123–138. DOI: 10.1016/j.jmarsys.2004.09.004

Angamuthu B, Darby SE, Nicholls RJ. 2018. Impacts of natural and human drivers on the multi-decadal morphological evolution of tidally-influenced deltas. Proceedings of the Royal Society A: Mathematical, Physical and Engineering Sciences **474** DOI: 10.1098/rspa.2018.0396

Anthony EJ, Besset M, Dussouillez P, Goichot M, Loisel H. 2019. Overview of the Monsoon-influenced Ayeyarwady River delta, and delta shoreline mobility in response to changing fluvial sediment supply. Marine Geology **417** : 106038. DOI: 10.1016/j.margeo.2019.106038 [online] Available from: https://doi.org/10.1016/j.margeo.2019.106038

Anthony EJ, Brunier G, Besset M, Goichot M, Dussouillez P, Nguyen VL. 2015. Linking rapid

erosion of the Mekong River delta to human activities. Scientific Reports **5** : 1–12. DOI: 10.1038/srep14745 [online] Available from: http://dx.doi.org/10.1038/srep14745

Arias-Ortiz A, Masqué P, Garcia-Orellana J, Serrano O, Mazarrasa I, Marbá N, Lovelock CE, Lavery PS, Duarte CM. 2018. Reviews and syntheses: 210Pb-derived sediment and carbon accumulation rates in vegetated coastal ecosystems - Setting the record straight. Biogeosciences **15** : 6791–6818. DOI: 10.5194/bg-15-6791-2018

Aucan J, Ridd P V. 2000. Tidal asymmetry in creeks surrounded by saltflats and mangroves with small swamp slopes. Wetlands Ecology and Management **8** : 223–231. DOI: 10.1023/A

Auerbach LW, Goodbred Jr SL, Small C, Ahmed KR, Gilligan JM, Wilson CA, Steckler MS, Roy K, Mondal DR, Ackerly BA. 2014. Flood risk of natural and embanked landscapes on the Ganges–Brahmaputra tidal delta plain. Nature Climate Change **5** : 153–157. DOI: 10.1038/nclimate2472

Augustinus PGEF. 1995. Geomorphology and Sedimentology of Mangroves. In Developments in Sedimentology , Perillo GME (ed). Elsevier; 333–357. [online] Available from: https://www.sciencedirect.com/science/article/pii/S0070457105800329 (Accessed 7 March 2019)

Aung TT, Mochida Y, Than MM. 2013. Prediction of recovery pathways of cyclone-disturbed mangroves in the mega delta of Myanmar. Forest Ecology and Management **293** : 103–113. DOI: 10.1016/j.foreco.2012.12.034 [online] Available from: http://dx.doi.org/10.1016/j.foreco.2012.12.034

Aung TT, Than MM, Katsuhiro O, Yukira M. 2011. Assessing the status of three mangrove species restored by the local community in the cyclone-affected area of the Ayeyarwady Delta, Myanmar. Wetlands Ecology and Management **19** : 195–208. DOI: 10.1007/s11273-011-9211-9

Bain RL, Hale RP, Goodbred SL. 2019. Flow reorganization in an anthropogenically modified tidal channel network: an example from the southwestern Ganges-Brahmaputra-Meghna delta. Journal of Geophysical Research: Earth Surface **124** : 2141–2159. DOI: 10.1029/2018JF004996

Baptist MJ, Babovic V, Uthurburu JR, Keijzer M, Uittenbogaard RE, Mynett A, Verwey A. 2007. On inducing equations for vegetation resistance. Journal of Hydraulic Research **45** : 435–450. DOI: 10.1080/00221686.2007.9521778

Baronas JJ, Stevenson EI, Hackney CR, Darby SE, Bickle MJ, Hilton RG, Larkin CS, Parsons DR, Khaing AM, Tipper ET. 2020. Integrating suspended sediment flux in large alluvial river channels: Application of a synoptic Rouse-based model to the Irrawaddy and Salween rivers. Journal of Geophysical Research: Earth Surface : 1–21. DOI: 10.1029/2020jf005554

Barua DK. 1990. Suspended sediment movement in the estuary of the Ganges-Brahmaputra-Meghna river system. Marine Geology **91** : 243–253. DOI: 10.1016/0025-3227(90)90039-M

Bayliss-Smith TP, Healey R, Lailey R, Spencer T, Stoddart DR. 1979. Tidal flows in salt marsh creeks. Estuarine and Coastal Marine Science **9** : 235–255. DOI: 10.1016/0302-3524(79)90038-0

Besset M, Gratiot N, Anthony EJ, Bouchette F, Goichot M, Marchesiello P. 2019. Mangroves and shoreline erosion in the Mekong River delta, Viet Nam. Estuarine, Coastal and Shelf Science **226** : 106263. DOI: 10.1016/j.ecss.2019.106263 [online] Available from: https://doi.org/10.1016/j.ecss.2019.106263

Blair NE, Aller RC. 2012. The fate of terrestrial organic carbon in the marine environment. Annual Review of Marine Science **4** : 401–423. DOI: 10.1146/annurev-marine-120709-142717

Blankespoor B, Dasgupta S, Lange G. 2017. Mangroves as a protection from storm surges in a changing climate. Ambio **46** : 478–491. DOI: 10.1007/s13280-016-0838-x

Boldt K V, Nittrouer CA, Ogston AS. 2013. Seasonal transfer and net accumulation of fine sediment on a muddy tidal flat: Willapa Bay, Washington. Continental Shelf Research **60** : S157–S172. DOI: 10.1016/j.csr.2012.08.012 [online] Available from: http://dx.doi.org/10.1016/j.csr.2012.08.012

Bouillon S, Middelburg JJ, Dehairs F, Borges A V., Abril G, Flindt MR, Ulomi S, Kristensen E. 2007. Importance of intertidal sediment processes and porewater exchange on the water column biogeochemistry in a pristine mangrove creek (Ras Dege, Tanzania). Biogeosciences **4** : 311–322. DOI: 10.5194/bg-4-311-2007

Brakenridge GR, Kettner AJ. 2018. River and reservoir watch version 3.4, Dartmouth Flood Observatory [online] Available from: http://floodobservatory.colorado.edu/DischargeAccess.html

Brichierei-Colombi JSA. 1983. Hydrological studies of the Irrawaddy Delta. 353–364 pp.

Brown S, Nicholls RJ. 2015. Subsidence and human influences in mega deltas: The case of the Ganges-Brahmaputra-Meghna. Science of the Total Environment **527**–**528** : 362–374. DOI: 10.1016/j.scitotenv.2015.04.124 [online] Available from: http://dx.doi.org/10.1016/j.scitotenv.2015.04.124

Brunier G, Anthony EJ, Gratiot N, Gardel A. 2019. Exceptional rates and mechanisms of muddy shoreline retreat following mangrove removal. Earth Surface Processes and Landforms **44** : 1559–1571. DOI: 10.1002/esp.4593

Bryan KR, Nardin W, Mullarney JC, Fagherazzi S. 2017. The role of cross-shore tidal dynamics in controlling intertidal sediment exchange in mangroves in Cù Lao Dung, Vietnam. Continental Shelf Research **147** : 128–143. DOI: 10.1016/j.csr.2017.06.014 [online] Available from: http://dx.doi.org/10.1016/j.csr.2017.06.014

Bulmer RH, Lewis M, O'Donnell E, Lundquist CJ. 2017a. Assessing mangrove clearance methods to minimise adverse impacts and maximise the potential to achieve restoration objectives. New Zealand Journal of Marine and Freshwater Research **51** : 110–126. DOI: 10.1080/00288330.2016.1260605

Bulmer RH, Schwendenmann L, Lohrer AM, Lundquist CJ. 2017b. Sediment carbon and nutrient fluxes from cleared and intact temperate mangrove ecosystems and adjacent sandflats.

Science of the Total Environment **599**–**600** : 1874–1884. DOI: 10.1016/j.scitotenv.2017.05.139 [online] Available from: http://dx.doi.org/10.1016/j.scitotenv.2017.05.139

Burchard H, Schuttelaars HM, Ralston DK. 2018. Sediment trapping in estuaries. Annual Review of Marine Science **10** : 371–395. DOI: https://doi.org/10.1146/annurev-marine-010816-060535

Cameron C, Hutley LB, Munksgaard NC, Phan S, Aung T, Thinn T, Aye WM, Lovelock CE. 2021. Impact of an extreme monsoon on CO2 and CH4 fluxes from mangrove soils of the Ayeyarwady Delta, Myanmar. Science of the Total Environment **760** : 143422. DOI: 10.1016/j.scitotenv.2020.143422 [online] Available from: https://doi.org/10.1016/j.scitotenv.2020.143422

Capo S, Sottolichio A, Brenon I, Castaing P, Ferry L. 2006. Morphology, hydrography and sediment dynamics in a mangrove estuary: The Konkoure Estuary, Guinea. Marine Geology **230** : 199–215. DOI: 10.1016/j.margeo.2006.05.003

Chapman AD, Darby SE. 2016. Evaluating sustainable adaptation strategies for vulnerable mega-deltas using system dynamics modelling: Rice agriculture in the Mekong Delta's An Giang Province, Vietnam. Science of the Total Environment **559** : 326–338. DOI: 10.1016/j.scitotenv.2016.02.162 [online] Available from: http://dx.doi.org/10.1016/j.scitotenv.2016.02.162

Chapman AD, Darby SE, Hoàng MH, Tompkins EL, Van TPD. 2016. Adaptation and development trade-offs: fluvial sediment deposition and the sustainability of rice-cropping in An Giang Province, Mekong Delta. Climate Change **137** : 593–608. DOI: 10.1007/s10584-016-1684-3

Chen D, Li X, Saito Y, Liu JP, Duan Y, Liu S, Zhang L. 2020. Recent evolution of the Irrawaddy (Ayeyarwady) Delta and the impacts of anthropogenic activities: A review and remote sensing survey. Geomorphology **365** : 107231. DOI: 10.1016/j.geomorph.2020.107231 [online] Available from: https://doi.org/10.1016/j.geomorph.2020.107231

Chen Y, Li Y, Thompson C, Wang X, Cai T, Chang Y. 2018. Differential sediment trapping abilities of mangrove and saltmarsh vegetation in a subtropical estuary. Geomorphology **318** : 270–282. DOI: 10.1016/j.geomorph.2018.06.018 [online] Available from: http://dx.doi.org/10.1016/j.geomorph.2018.06.018

Coco G, Zhou Z, Maanen B Van, Olabarrieta M, Tinoco R, Townend I. 2013. Morphodynamics of tidal networks: Advances and challenges. Marine Geology **346** : 1–16. DOI: 10.1016/j.margeo.2013.08.005 [online] Available from: http://dx.doi.org/10.1016/j.margeo.2013.08.005

Deignan-Schmidt SR, Whitney MM, Jia Y. 2021. Influences of islands and shoals on coastal water properties, flushing time, and dispersion within western Long Island Sound. Estuaries and Coasts **44** : 991–1009. DOI: 10.1007/s12237-020-00780-7

Deltares. 2018. Delft3D-Flow User Manual . Delft-Wageningen, The Netherlands. [online]

Available from: https://www.deltares.nl

Dencer-Brown A, Alfaro A, Milne S, Perrott J. 2018. A Review on Biodiversity, Ecosystem Services, and Perceptions of New Zealand's Mangroves: Can We Make Informed Decisions about Their Removal? Resources **7** : 23. DOI: 10.3390/resources7010023

Dong TY, Nittrouer JA, McElroy B, Il'icheva E, Pavlov M, Ma H, Moodie AJ, Moreido VM. 2020. Predicting water and sediment partitioning in a delta channel network under varying discharge conditions. Water Resources Research : 1–21. DOI: 10.1029/2020wr027199

Dronkers J. 1986. Tidal asymmetry and estuarine morphology. Netherlands Journal of Sea Research **20** : 117–131. DOI: 10.1016/0077-7579(86)90036-0

Duke NC et al. 2007. A World Without Mangroves? Science **317** : 41b-42b. DOI: 10.1126/science.317.5834.41b [online] Available from: http://www.sciencemag.org/cgi/doi/10.1126/science.317.5834.41b

Edmonds DA, Paola C, Hoyal DCJD, Sheets BA. 2011. Quantitative metrics that describe river deltas and their channel networks. Journal of Geophysical Research: Earth Surface **116** : 1–15. DOI: 10.1029/2010JF001955

Eidam EF, Nittrouer CA, Ogston AS, DeMaster DJ, Liu JP, Nguyen TT, Nguyen TN. 2017. Dynamic controls on shallow clinoform geometry: Mekong Delta, Vietnam. Continental Shelf Research **147** : 165–181. DOI: 10.1016/j.csr.2017.06.001 [online] Available from: http://dx.doi.org/10.1016/j.csr.2017.06.001

Estoque RC et al. 2018. Assessing environmental impacts and change in Myanmar's mangrove ecosystem service value due to deforestation (2000–2014). Global Change Biology **24** : 5391–5410. DOI: 10.1111/gcb.14409

Fagherazzi S. 2008. Self-organization of tidal deltas. Proceedings of the National Academy of Sciences **105** : 18692–18695. DOI: 10.1073/pnas.0806668105

Fagherazzi S, Fitzgerald DM, Fulweiler RW, Hughes Z, Wiberg PL, McGlathery K, Morris JT, Tolhurts TJ, Deegan LA, Johnson DS. 2013. Ecogeomorphology of Salt Marshes. In Treatise on Geomorphology , Shroder J, Budtler DR, and Hupp CR (eds). Academic Press: San Diego, CA; 182–200. [online] Available from: http://dx.doi.org/10.1016/B978-0-12-374739-6.00329-8

Fricke AT, Nittrouer CA, Ogston AS, Nowacki DJ, Asp NE, Souza Filho PWM. 2019. Morphology and dynamics of the intertidal floodplain along the Amazon tidal river. Earth Surface Processes and Landforms **44** : 204–218. DOI: 10.1002/esp.4545

Fricke AT, Nittrouer CA, Ogston AS, Vo-Luong HP. 2017. Asymmetric progradation of a coastal mangrove forest controlled by combined fluvial and marine influence, Cù Lao Dung, Vietnam. Continental Shelf Research **147** : 78–90. DOI: 10.1016/j.csr.2017.07.012 [online] Available from: http://dx.doi.org/10.1016/j.csr.2017.07.012

Fricke AT, Ogston AS, Nittrouer CA, Glover HE, Lahr EJ, Aung C, Naing T, Vo-Luong P.

2020. Sediment delivery to deltaic land surfaces in the absence of artificial levees: Contrasting the Ayeyarwady and Mekong Deltas. Abstract MG44A-2216 pp.

Friedrichs CT. 2010. Barotropic tides in channelized estuaries. In Contemporary Issues in Estuarine Physics , Valle-Levinson A (ed). Cambridge University Press: Cambridge, UK; 27–61.

Friedrichs CT. 2011. Tidal Flat Morphodynamics: A Synthesis. In Treatise on Estuarine and Coastal Science , Wolanski E and McLusky D (eds). Elsevier Inc.; 137–170. [online] Available from: http://dx.doi.org/10.1016/B978-0-12-374711-2.00307-7

Friess DA, Rogers K, Lovelock CE, Krauss KW, Hamilton SE, Lee SY, Lucas R, Primavera J, Rajkaran A, Shi S. 2019. The state of the world's mangrove forests: Past, present, and future. Annual Review of Environment and Resources **44** : 89–115. DOI: 10.1146/annurev-environ-101718-033302

Fritz HM, Blount CD, Thwin S, Thu MK, Chan N. 2009. Cyclone Nargis storm surge in Myanmar. Nature Geoscience **2** : 448–449. DOI: 10.1038/ngeo558

Furuichi T, Win Z, Wasson RJ. 2009. Discharge and suspended sediment transport in the Ayeyarwady River, Myanmar: Centennial and decadal changes. Hydrological Processes **23** : 1631–1641. DOI: 10.1002/hyp

Furukawa K, Wolanski E. 1996. Sedimentation in mangrove forests. Mangroves and Salt Marshes **1** : 3–10.

Furukawa K, Wolanski E, Mueller H. 1997. Currents and sediment transport in mangrove forests. Estuarine, Coastal and Shelf Science **44** : 301–310.

Galloway WE. 1975. Process framework for describing the morphologic and stratigraphic evolution of deltaic depositional system. In Deltas: Models for Exploration , Broussard ML (ed). Houston Geological Society: Houston, TX; 87–98.

Gao A, Yang SL, Li G, Li P, Chen SL. 2010. Long-term morphological evolution of a tidal island as affected by natural factors and human activities, the Yangtze estuary. Journal of Coastal Research **26** : 123–131. DOI: 10.2112/08-1052.1

Gerwing TG, Davies MM, Clements J, Flores AM, Thomson HM, Nelson KR, Kushneryk K, Brouard-John EK, Harvey B, Plate E. 2020. Do you want to breach an embankment? Synthesis of the literature and practical considerations for breaching of tidally influenced causeways and dikes. Estuarine, Coastal and Shelf Science **245** : 107024. DOI: 10.1016/j.ecss.2020.107024 [online] Available from: https://doi.org/10.1016/j.ecss.2020.107024

Geyer WR, MacCready P. 2014. The estuarine circulation. Annual Review of Fluid Mechanics **46** : 175–197. DOI: 10.1146/annurev-fluid-010313-141302

Geyer WR, Woodruff JD, Traykovski P. 2001. Sediment transport and trapping in the Hudson River Estuary. Estuaries **24** : 670–679. DOI: 10.2307/1352875

Giddings SN, Monismith SG, Fong DA, Stacey MT. 2013. Using depth-normalized coordinates to examine mass transport residual circulation in estuaries with large tidal amplitude relative to the mean depth. Journal of Physical Oceanography **44** : 128–148. DOI: 10.1175/jpo-d-12-0201.1

Giosan L et al. 2018. On the Holocene evolution of the Ayeyawady megadelta. Earth Surface Dynamics **6** : 451–466. DOI: 10.5194/esurf-6-451-2018

Giri C, Ochieng E, Tieszen LL, Zhu Z, Singh A, Loveland T, Masek J, Duke N. 2011. Status and distribution of mangrove forests of the world using earth observation satellite data. Global Ecology and Biogeography **20** : 154–159. DOI: 10.1111/j.1466-8238.2010.00584.x

Gleeson J, Santos IR, Maher DT, Golsby-smith L. 2013. Groundwater–surface water exchange in a mangrove tidal creek: Evidence from natural geochemical tracers and implications for nutrient budgets. Marine Chemistry **156** : 27–37.

Glover HE, Ogston AS, Fricke AT, Nittrouer CA, Aung C, Naing T, Kyu Kyu K, Htike H. 2021. Connecting sediment retention to distributary-channel hydrodynamics and sediment dynamics in a tide-dominated delta: the Ayeyarwady Delta, Myanmar. Journal of Geophysical Research: Earth Surface **126** : 1–19. DOI: 10.1029/2020JF005882

Glover HE, Stokes DJ, Ogston AS, Bryan KR, Pilditch CA. 2020. Impacts of Mangrove Removal on Hydrodynamics and Sediment Transport over Decadal Timescales in a Quiescent, Mesotidal, New Zealand Estuary: In-situ Observations and Numerical Modeling. Abstract EP052-0018 pp.

Gomes VJC, Asp NE, Siegle E, McLachlan RL, Ogston AS, Silva AMM, Nittrouer CA, Souza DF. 2020. Connection between macrotidal estuaries along the southeastern Amazon coast and its role in coastal progradation. Estuarine, Coastal and Shelf Science **240** : 106794. DOI: 10.1016/j.ecss.2020.106794 [online] Available from: https://doi.org/10.1016/j.ecss.2020.106794

Goodbred SL, Kuehl SA. 1998. Floodplain processes in the Bengal Basin and the storage of Ganges–Brahmaputra river sediment: an accretion study using 137-Cs and 210-Pb geochronology. Sedimentary Geology **121** : 239–258. DOI: 10.1016/S0037-0738(98)00082-7

Goodbred SL, Kuehl SA. 1999. Holocene and modern sediment budgets for the Ganges-Brahmaputra river system: Evidence for highstand dispersal to flood-plain, shelf, and deep-sea depocenters. Geology **27** : 559–562. DOI: 10.1130/0091-7613(1999)027<0559:HAMSBF>2.3.CO;2

Goodbred SL, Saito Y. 2012. Tide-Dominated Deltas. In Principles of Tidal Sedimentology , . Springer Netherlands: Dordrecht; 129–149.

Gordon R. 1885. The Irawadi River. Proceedings of the Royal Geographical Society and Monthly Record of Geography : 292–331.

Granek EF, Ruttenberg BI. 2007. Protective capacity of mangroves during tropical storms: A case study from “Wilma” and “Gamma” in Belize. Marine Ecology Progress Series **343** : 101–105. DOI: 10.3354/meps07141

Grill G et al. 2019. Mapping the world's free-flowing rivers. Nature **569** : 215–221. DOI: 10.1038/s41586-019-1111-9

Gugliotta M, Saito Y. 2019. Matching trends in channel width, sinuosity, and depth along the fluvial to marine transition zone of tide-dominated river deltas: The need for a revision of depositional and hydraulic models. Earth-Science Reviews **191** : 93–113. DOI: 10.1016/j.earscirev.2019.02.002 [online] Available from: https://doi.org/10.1016/j.earscirev.2019.02.002

Guo B, Ahmadian R, Evans P, Falconer RA. 2020. Studying the wake of an island in a macro-tidal estuary. Water (Switzerland) **12** : 1225–1243. DOI: 10.3390/W12051225

Guo L, Wang ZB, Townend I, He Q. 2019. Quantification of Tidal Asymmetry and Its Nonstationary Variations. Journal of Geophysical Research: Oceans **124** : 773–787. DOI: 10.1029/2018JC014372

Hale RP, Wilson CA, Bomer EJ, Reed D, Orford JD. 2019. Seasonal variability of forces controlling sedimentation in the Sundarbans National Forest, Bangladesh. Frontiers in Earth Science **7** : 1–13. DOI: 10.3389/feart.2019.00211

Harris RJ, Pilditch CA, Greenfield BL, Moon V, Kröncke I. 2016. The Influence of Benthic Macrofauna on the Erodibility of Intertidal Sediments with Varying mud Content in Three New Zealand Estuaries. Estuaries and Coasts **39** : 815–828. DOI: 10.1007/s12237-015-0036-2

Hayashi S, Kamoshita A, Yamagishi J. 2006. Effect of Planting Density on Grain Yield and Water Productivity of Rice (Oryza sativa L.) Grown in Flooded and Non-flooded Fields in Japan. Plant Production Science **9** : 298–311. DOI: 10.1626/pps.9.298

Hayden HL, Granek EF. 2015. Coastal sediment elevation change following anthropogenic mangrove clearing. Estuarine, Coastal and Shelf Science **165** : 70–74. DOI: 10.1016/j.ecss.2015.09.004 [online] Available from: http://dx.doi.org/10.1016/j.ecss.2015.09.004

Hedley PJ, Bird MI, Robinson RAJ. 2010. Evolution of the Irrawaddy delta region since 1850. Geographical Journal **176** : 138–149. DOI: 10.1111/j.1475-4959.2009.00346.x

Hiatt M, Addink EA, Kleinhans MG. 2021. Connectivity and directionality in estuarine channel networks. Earth Surface Processes and Landforms : 1–18. DOI: 10.1002/esp.5286

Hiatt M, Castañeda-Moya E, Twilley R, Hodges BR, Passalacqua P. 2018. Channel-island connectivity affects water exposure time distributions in a coastal river delta. Water Resources Research **54** : 2212–2232. DOI: 10.1002/2017WR021289

Hiatt M, Passalacqua P. 2015. Hydrological connectivity in river deltas: The first-order importance of channel-island exchange. Water Resources Research **51** : 2264–2282. DOI: doi:10.1002/2014WR016149

Hirano A. 2021. Effects of climate change on spatiotemporal patterns of tropical cyclone tracks and their implications for coastal agriculture in Myanmar. Paddy and Water Environment DOI:

10.1007/s10333-021-00842-x [online] Available from: https://doi.org/10.1007/s10333-021-00842-x

Hoitink AJF, Jay DA. 2016. Tidal river dynamics: Implications for deltas. Reviews of Geophysics **54** : 240–272. DOI: 10.1002/2015RG000507

Hood WG. 2006. A conceptual model of depositional, rather than erosional, tidal channel development in the rapidly prograding Skagit River Delta (Washington, USA). Earth Surface Processes and Landforms **31** : 1824–1838. DOI: 10.1002/esp [online] Available from: http://doi.wiley.com/10.1002/esp.1730

Hood WG. 2007. Scaling tidal channel geometry with marsh island area: A tool for habitat restoration, linked to channel formation process. Water Resources Research **43** : 1–15. DOI: 10.1029/2006WR005083

Hood WG. 2016. Parallel scaling of tidal channel length and surface area with marsh area for 1st through Kth-ranked channels and their tributaries: Application for tidal marsh restoration. Ecological Engineering **95** : 54–63. DOI: 10.1016/j.ecoleng.2016.06.059 [online] Available from: http://dx.doi.org/10.1016/j.ecoleng.2016.06.059

Hope H. 2002. Sediment dynamics of Waikaraka Estuary, a small, semi- enclosed estuarine system in the upper reaches of a developed harbour, University of Waikato

Horstman EM, Bryan KR, Mullarney JC. 2021. Drag variations, tidal asymmetry and tidal range changes in a mangrove creek system. Earth Surface Processes and Landforms **46** : 1828–1846. DOI: 10.1002/esp.5124

Horstman EM, Bryan KR, Mullarney JC, Pilditch CA, Eager CA. 2018a. Are flow-vegetation interactions well represented by mimics? A case study of mangrove pneumatophores. Advances in Water Resources **111** : 360–371. DOI: 10.1016/j.advwatres.2017.11.018 [online] Available from: https://doi.org/10.1016/j.advwatres.2017.11.018

Horstman EM, Dohmen-Janssen CM, Bouma TJ, Hulscher SJMH. 2015. Tidal-scale flow routing and sedimentation in mangrove forests: Combining field data and numerical modelling. Geomorphology **228** : 244–262. DOI: 10.1016/j.geomorph.2014.08.011 [online] Available from: http://dx.doi.org/10.1016/j.geomorph.2014.08.011

Horstman EM, Dohmen-Janssen CM, Hulscher SJMH. 2013a. Flow routing in mangrove forests: A field study in Trang province, Thailand. Continental Shelf Research **71** : 52–67. DOI: 10.1016/j.csr.2013.10.002

Horstman EM, Dohmen-Janssen CM, Hulscher SJMH. 2013b. Modeling Tidal Dynamics in a Mangrove Creek Catchment in Delft3d. In Extended abstracts of Coastal Dynamics 2013 SHOM , Bonneton P and Garlan T (eds). 833–844.

Horstman EM, Dohmen-Janssen CM, Narra PMF, van den Berg NJF, Siemerink M, Hulscher SJMH. 2014. Wave attenuation in mangroves: A quantitative approach to field observations. Coastal Engineering **94** : 47–62. DOI: 10.1016/j.coastaleng.2014.08.005 [online] Available

from: http://dx.doi.org/10.1016/j.coastaleng.2014.08.005

Horstman EM, Lundquist CJ, Bryan KR, Bulmer RH, Mullarney JC, Stokes DJ. 2018b. The dynamics of expanding mangroves in New Zealand. In Threats to Mangrove Forests , Makowski C and Finkl C (eds). Coastal Research Library; 23–51.

Hunt S, Bryan KR, Mullarney JC. 2015. The influence of wind and waves on the existence of stable intertidal morphology in meso-tidal estuaries. Geomorphology **228** : 158–174. DOI: 10.1016/j.geomorph.2014.09.001 [online] Available from: http://dx.doi.org/10.1016/j.geomorph.2014.09.001

Hunt S, Bryan KR, Mullarney JC, Pritchard M. 2016. Observations of asymmetry in contrasting wave- and tidally-dominated environments within a mesotidal basin: implications for estuarine morphological evolution. Earth Surface Processes and Landforms **41** : 2207–2222. DOI: 10.1002/esp.3985

Ketelsen T, Taylor L, Mai Ky Vinh, Hunter R, Johnston R, Liu S, Tint K, Charles KMMG and M. 2017. State of Knowledge: River Health in the Ayeyarwady . Vientiane, Lao PDR [online] Available from: https://hdl.handle.net/10568/82968

Knapp KR, Diamond HJ, Kossin JP, Kruk MC, Schreck CJ. 2018. International Best Track Archive for Climate Stewardship (IBTrACS) Project, Version 4. NOAA National Centers for Environmental Information DOI: 10.1175/2009BAMS2755.1 [online] Available from: https://www.ncdc.noaa.gov/ibtracs/index.php?name=browse (Accessed 26 August 2021)

Koppenaal EC, Esselink P, van Duin WE, Bakker JP. 2021. Temporal and spatial accretion patterns and the impact of livestock grazing in a restored coastal salt marsh. Estuaries and Coasts **45** : 510–522. DOI: 10.1007/s12237-021-00963-w [online] Available from: https://doi.org/10.1007/s12237-021-00963-w

Krauss KW, Allen JA, Cahoon DR. 2003. Differential rates of vertical accretion and elevation change among aerial root types in Micronesian mangrove forests. Estuarine, Coastal and Shelf Science **56** : 251–259. DOI: 10.1016/S0272-7714(02)00184-1

Kravtsova VI, Mikhailov VN, Kidyaeva VM. 2009. Hydrological regime, morphological features and natural territorial complexes of the Irrawaddy River Delta (Myanmar). Water Resources **36** : 243–260. DOI: 10.1134/s0097807809030014

Kuehl SA, Williams J, Liu JP, Harris C, Aung DW, Tarpley D, Goodwyn M, Aye YY. 2019. Sediment dispersal and accumulation off the Ayeyarwady delta – Tectonic and oceanographic controls. Marine Geology **417** : 106000. DOI: 10.1016/j.margeo.2019.106000 [online] Available from: https://doi.org/10.1016/j.margeo.2019.106000

Larsen LG. 2019. Multiscale flow-vegetation-sediment feedbacks in low-gradient landscapes. Geomorphology **334** : 165–193. DOI: 10.1016/j.geomorph.2019.03.009 [online] Available from: https://doi.org/10.1016/j.geomorph.2019.03.009

Lazarus ED, Constantine JA. 2013. Generic theory for channel sinuosity. Proceedings of the

National Academy of Sciences of the United States of America **110** : 8447–8452. DOI: 10.1073/pnas.1214074110

Leimgruber P, Kelly DS, Steininger MK, Brunner J, Müller T, Songer M. 2005. Forest cover change patterns in Myanmar (Burma) 1990–2000. Environmental Conservation **32** : 356. DOI: 10.1017/S0376892905002493 [online] Available from: http://www.journals.cambridge.org/abstract_S0376892905002493

Lerczak JA, Geyer WR, Chant RJ. 2007. Mechanisms driving the time-dependent salt flux in a partially stratified estuary. Journal of Physical Oceanography **36** : 2296–2311. DOI: 10.1175/jpo2959.1

Lesser GR, Roelvink JA, Kester JATM Van, Stelling GS. 2004. Development and validation of a three-dimensional morphological model. Coastal Engineering **51** : 883–915. DOI: 10.1016/j.coastaleng.2004.07.014

Li L, Wang XH, Williams D, Sidhu H, Song D. 2012. Numerical study of the effects of mangrove areas and tidal flats on tides: A case study of Darwin Harbour, Australia. Journal of Geophysical Research **117** : 1–12. DOI: 10.1029/2011JC007494

Liang M, Van Dyk C, Passalacqua P. 2016. Quantifying the patterns and dynamics of river deltas under conditions of steady forcing and relative sea level rise. Journal of Geophysical Research: Earth Surface **121** : 465–496. DOI: 10.1002/2015JF003653

LINZ. 2017. Bay of Plenty - Tauranga and Coast LiDAR 1m DEM (2015). Land Information New Zealand [online] Available from: https://data.linz.govt.nz/ (Accessed 20 September 2006)

Liu JP, Kuehl SA, Pierce AC, Williams J, Blair NE, Harris C, Aung DW, Aye YY. 2020. Fate of Ayeyarwady and Thanlwin Rivers sediments in the Andaman Sea and Bay of Bengal. Marine Geology **423** : 106137. DOI: 10.1016/j.margeo.2020.106137 [online] Available from: https://doi.org/10.1016/j.margeo.2020.106137

Lovelock CE, Sorrell BK, Hancock N, Hua Q, Swales A. 2010. Mangrove Forest and Soil Development on a Rapidly Accreting Shore in New Zealand. Ecosystems **13** : 437–451. DOI: 10.1007/s10021-010-9329-2

Lundquist CJ, Hailes SF, Carter KR, Burgess T. 2014. Ecological Status of Mangrove Removal Sites in the Auckland Region

Lynch JC, Meriwether JR, McKee BA, Vera-Herrera F, Twilley RR. 1989. Recent accretion in mangrove ecosystems based on 137Cs and 210Pb. Estuaries **12** : 284–299. DOI: 10.2307/1351907 [online] Available from: http://link.springer.com/10.2307/1351907

Van Maanen B, Coco G, Bryan KR. 2015. On the ecogeomorphological feedbacks that control tidal channel network evolution in a sandy mangrove setting. Proceedings of the Royal Society A: Mathematical, Physical and Engineering Sciences **471** : 1–24. DOI: 10.1098/rspa.2015.0115

MacCready P, Banas NS. 2012. Residual Circulation, Mixing, and Dispersion . Elsevier Inc.

[online] Available from: http://dx.doi.org/10.1016/B978-0-12-374711-2.00205-9

Mai S, Bartholomä A. 2000. The missing mud flats of the Wadden Sea: a reconstruction of sediments and accommodation space lost in the wake of land reclamation. In Proceedings in marine science: Muddy coast dynamics and resource management , Liebezeit G, Delafontaine MT, and Flemming BW (eds). Elsevier: New York, NY; 294. [online] Available from: http://hdl.handle.net/2027/mdp.39015049555314

Massel SR, Furukawa K, Brinkman RM. 1999. Surface wave propagation in mangrove forests. Fluid Dynamics Research **24** : 219–249.

Mazda Y, Kanazawa N, Wolanski E. 1995. Tidal asymmetry in mangrove creeks. Hydrobiologia **295** : 51–58. DOI: 10.1007/BF00029110

Mazda Y, Magi M, Ikeda Y, Kurokawa T, Asano T. 2006. Wave reduction in a mangrove forest dominated by Sonneratia sp. Wetlands Ecology and Management **14** : 365–378. DOI: 10.1007/s11273-005-5388-0

Mazda Y, Wolanski E, King B, Sase A, Ohtsuka D, Magi M. 1997. Drag force due to vegetation in mangrove swamps. Mangroves and Salt marshes **1** : 193–199. DOI: 10.1023/A:1009949411068

McDougall TJ, Barker PM. 2011. Getting started with TEOS-10 and the Gibbs Seawater (GSW) Oceanographic Toolbox

McLachlan RL, Ogston AS, Allison MA. 2017. Implications of tidally-varying bed stress and intermittent estuarine stratification on fine-sediment dynamics through the Mekong's tidal river to estuarine reach. Continental Shelf Research **147** : 27–37. DOI: 10.1016/j.csr.2017.07.014 [online] Available from: http://dx.doi.org/10.1016/j.csr.2017.07.014

McLachlan RL, Ogston AS, Asp NE, Fricke AT, Nittrouer CA, Gomes VJC. 2020a. Impacts of tidal-channel connectivity on transport asymmetry and sediment exchange with mangrove forests. Estuarine, Coastal and Shelf Science **233** : 106524. DOI: 10.1016/j.ecss.2019.106524 [online] Available from: https://doi.org/10.1016/j.ecss.2019.106524

McLachlan RL, Ogston AS, Asp NE, Fricke AT, Nittrouer CA, Schettini CAF. 2020b. Morphological evolution of a macrotidal back-barrier environment: The Amazon Coast. Sedimentology **67** : 3492–3512. DOI: 10.1111/sed.12752

Meselhe E, Sadid K, Khadka A. 2021. Sediment distribution, retention and morphodynamic analysis of a river-dominated deltaic system. Water **13** : 1341. DOI: 10.3390/w13101341

Miller M, McCave I, Komar P. 1977. Threshold of sediment motion under unidirectional currents. Sedimentology **24** : 507–527.

Milliman JD, Farnsworth K. 2011. River discharge to the coastal ocean: A global synthesis . Cambridge University Press.: Cambridge

Milliman JD, Huang-ting S, Zuo-sheng Y, H. Meade RH. 1985. Transport and deposition of river sediment in the Changjiang estuary and adjacent continental shelf. Continental Shelf Research **4** : 37–45. DOI: 10.1016/0278-4343(85)90020-2

Möhlenkamp P, Beebe CK, McManus MA, Kawelo AH, Kotubetey K, Lopez-Guzman M, Nelson CE, Alegado RA. 2018. Ku Hou Kuapa: Cultural restoration improves water budget and water quality dynamics in He'eia Fishpond. Sustainability (Switzerland) **11** DOI: 10.3390/su11010161

Montgomery JM, Bryan KR, Mullarney JC, Horstman EM. 2019. Attenuation of Storm Surges by Coastal Mangroves. Geophysical Research Letters **46** : 2680–2689. DOI: 10.1029/2018GL081636

Moon VG, de Lange WP, Garae CP, Morz T, Jorat ME, Kreiter S. 2015. Monitoring the landslide at Bramley Drive, Tauranga, NZ. Proceedings of the twelfth Australia New Zealand Conference on Geomechanics

Mueller DS. 2016. QRev—Software for computation and quality assurance of acoustic doppler current profiler moving-boat streamflow measurements . Reston, VA [online] Available from: http://pubs.er.usgs.gov/publication/ofr20161052

Mullarney JC, Henderson SM, Reyns JAH, Norris BK, Bryan KR. 2017. Spatially varying drag within a wave-exposed mangrove forest and on the adjacent tidal flat. Continental Shelf Research **147** : 102–113. DOI: 10.1016/j.csr.2017.06.019 [online] Available from: http://dx.doi.org/10.1016/j.csr.2017.06.019

Nguyen AD, Savenije HHG, Pham DN, Tang DT. 2008. Using salt intrusion measurements to determine the freshwater discharge distribution over the branches of a multi-channel estuary: The Mekong Delta case. Estuarine, Coastal and Shelf Science **77** : 433–445. DOI: 10.1016/j.ecss.2007.10.010

Nidzieko NJ, Ralston DK. 2012. Tidal asymmetry and velocity skew over tidal flats and shallow channels within a macrotidal river delta. Journal of Geophysical Research: Oceans **117** : 1–17. DOI: 10.1029/2011JC007384

Nienhuis JH, Ashton AD, Edmonds DA, Hoitink AJF, Kettner AJ, Rowland JC, Törnqvist TE. 2020. Global-scale human impact on delta morphology has led to net land area gain. Nature **577** : 514–518. DOI: 10.1038/s41586-019-1905-9 [online] Available from: http://dx.doi.org/10.1038/s41586-019-1905-9

Nienhuis JH, Hoitink AJF, Törnqvist TE. 2018. Future change to tide-influenced deltas. Geophysical Research Letters **45** : 3499–3507. DOI: 10.1029/2018GL077638

Nittrouer CA, DeMaster DJ. 1996. The Amazon shelf setting: Tropical, energetic, and influenced by a large river. Continental Shelf Research **16** : 553–573. DOI: 10.1016/0278-4343(95)00069-0

Nittrouer CA, DeMaster DJ, McKee BA, Cutshall NH, Larsen IL. 1984. The effect of sediment mixing on Pb-210 accumulation rates for the Washington continental shelf. Marine Geology **54** :

201–221. DOI: 10.1016/0025-3227(84)90038-0

Nittrouer CA, Kuehl SA, Sternberg RW, Figueiredo AG, Faria LEC. 1995. An introduction to the geological significance of sediment transport and accumulation on the Amazon continental shelf. Marine Geology **125** : 177–192. DOI: 10.1016/0025-3227(95)00075-A

Nittrouer CA, Sternberg RW, Carpenter R, Bennett JT. 1979. The use of Pb-210 geochronology as a sedimentological tool: Application to the Washington continental shelf. Marine Geology **31** : 297–316. DOI: 10.1016/0025-3227(79)90039-2

Norris BK, Mullarney JC, Bryan KR, Henderson SM. 2017. The effect of pneumatophore density on turbulence: A field study in a Sonneratia-dominated mangrove forest, Vietnam. Continental Shelf Research **147** : 114–127. DOI: 10.1016/j.csr.2017.06.002

Nowacki DJ, Ogston AS. 2013. Water and sediment transport of channel-flat systems in a mesotidal mudflat: Willapa Bay, Washington. Continental Shelf Research **60** : S111–S124. DOI: 10.1016/j.csr.2012.07.019 [online] Available from: http://dx.doi.org/10.1016/j.csr.2012.07.019

Nowacki DJ, Ogston AS, Nittrouer CA, Fricke AT, Asp NE, Souza Filho PWM. 2019. Seasonal, tidal, and geomorphic controls on sediment export to Amazon River tidal floodplains. Earth Surface Processes and Landforms **44** : 1846–1859. DOI: 10.1002/esp.4616

Nowacki DJ, Ogston AS, Nittrouer CA, Fricke AT, Tri VPD. 2015. Sediment dynamics in the lower Mekong River: Transition from tidal river to estuary. Journal of Geophysical Research: Oceans : 6363–6383. DOI: 10.1002/2014JC010320

Ogston AS, Allison MA, Mullarney JC, Nittrouer CA. 2017. Sediment- and hydro-dynamics of the Mekong Delta: From tidal river to continental shelf. Continental Shelf Research **147** : 1–6. DOI: 10.1016/j.csr.2017.08.022

Ogston AS, Sternberg RW, Nittrouer CA, Martin DP, Goñi MA, Crockett JS. 2008. Sediment delivery from the Fly River tidally dominated delta to the nearshore marine environment and the impact of El Niño. Journal of Geophysical Research **113** : 1–18. DOI: 10.1029/2006JF000669

Omori K, Sakai T, Miyamoto J, Itou A, Oo AN, Hirano A. 2020. Assessment of paddy fields' damage caused by Cyclone Nargis using MODIS time-series images (2004–2013). Paddy and Water Environment **19** : 271–281. DOI: 10.1007/s10333-020-00829-0 [online] Available from: https://doi.org/10.1007/s10333-020-00829-0

Orescanin MM, Elgar S, Raubenheimer B. 2016. Changes in bay circulation in an evolving multiple inlet system. Continental Shelf Research **124** : 13–22. DOI: 10.1016/j.csr.2016.05.005 [online] Available from: http://dx.doi.org/10.1016/j.csr.2016.05.005

Ortals C, Cordero O, Valle-Levinson A, Angelini C. 2021. Flows, transport, and effective drag in intertidal salt marsh creeks. Journal of Geophysical Research: Oceans **126** : 1–18. DOI: 10.1029/2021JC017357

Ouyang X, Lee SY, Connolly RM. 2017. The role of root decomposition in global mangrove and

saltmarsh carbon budgets. Earth-Science Reviews **166** : 53–63. DOI: 10.1016/j.earscirev.2017.01.004 [online] Available from: http://dx.doi.org/10.1016/j.earscirev.2017.01.004

Pacheco A, Ferreira Ó, Williams JJ, Garel E, Vila-Concejo A, Dias JA. 2010. Hydrodynamics and equilibrium of a multiple-inlet system. Marine Geology **274** : 32–42. DOI: 10.1016/j.margeo.2010.03.003 [online] Available from: http://dx.doi.org/10.1016/j.margeo.2010.03.003

Palinkas CM. 2009. The Timing of Floods and Storms as a Controlling Mechanism for Shelf Deposit Morphology. Journal of Coastal Research **255** : 1122–1129. DOI: 10.2112/08-1041.1

Passalacqua P. 2017. The Delta Connectome: A network-based framework for studying connectivity in river deltas. Geomorphology **277** : 50–62. DOI: 10.1016/j.geomorph.2016.04.001 [online] Available from: http://dx.doi.org/10.1016/j.geomorph.2016.04.001

Passalacqua P, Lanzoni S, Paola C, Rinaldo A. 2013. Geomorphic signatures of deltaic processes and vegetation: The Ganges-Brahmaputra-Jamuna case study. Journal of Geophysical Research: Earth Surface **118** : 1838–1849. DOI: 10.1002/jgrf.20128

Pawlowicz R, Beardsley B, Lentz S. 2002. Classical tidal harmonic analysis including error estimates in MATLAB using T_TIDE. Computers and Geosciences **28** : 929–937.

Pérez A, Machado W, Gutierrez D, Stokes D, Sanders L, Smoak JM, Santos I, Sanders CJ. 2017. Changes in organic carbon accumulation driven by mangrove expansion and deforestation in a New Zealand estuary. Estuarine, Coastal and Shelf Science **192** : 108–116. DOI: 10.1016/j.ecss.2017.05.009

Pethick JS. 1980. Velocity surges and asymmetry in tidal channels. Estuarine and Coastal Marine Science **11** : 331–345. DOI: 10.1016/S0302-3524(80)80087-9

Posamentier HW, Jervey MT, Vail PR. 1988. Eustatic controls on clastic deposition I—Conceptual framework . Society of Economic Paleontologists and Mineralogists

Postma H. 1967. Sediment transport and sedimentation in the estuarine environment. Estuaries **83** : 158–179.

Pritchard M, Green M. 2017. Trapping and episodic flushing of suspended sediment from a tidal river. Continental Shelf Research **143** : 286–294. DOI: 10.1016/j.csr.2016.07.007 [online] Available from: http://dx.doi.org/10.1016/j.csr.2016.07.007

Ralston DK, Geyer WR. 2017. Sediment transport time scales and trapping efficiency in a tidal river. Journal of Geophysical Research: Earth Surface **122** : 2042–2063. DOI: 10.1002/2017JF004337

Ramaswamy V, Rao PS, Rao KH, Thwin S, Rao NS, Raiker V. 2004. Tidal influence on suspended sediment distribution and dispersal in the northern Andaman Sea and Gulf of Martaban. Marine Geology **208** : 33–42. DOI: 10.1016/j.margeo.2004.04.019

Ridd P V, Sam R. 1996. Profiling groundwater salt concentrations in mangrove swamps and tropical salt flats. Estuarine, Coastal and Shelf Science **43** : 627–635.

Robinson RAJ, Bird MI, Oo NW, Hoey TB, Aye MM, Higgitt DL, X. X. L, Swe A, Tun T, Win SL. 2007. The Irrawaddy River sediment flux to the Indian Ocean: The original nineteenth-century data revisited. The Journal of Geology **115** : 629–640. DOI: 10.1086/521607 [online] Available from: http://www.journals.uchicago.edu/doi/10.1086/521607

Rodolfo KS. 1969. Bathymetry and marine geology of the Andaman Basin, and tectonic implications for southeast asia. Bulletin of the Geological Society of America **80** : 1203–1230. DOI: 10.1130/0016-7606(1969)80[1203:BAMGOT]2.0.CO;2

Rogers KG, Goodbred SL, Mondal DR. 2013. Monsoon sedimentation on the "abandoned" tide-influenced Ganges-Brahmaputra delta plain. Estuarine, Coastal and Shelf Science **131** : 297–309. DOI: 10.1016/j.ecss.2013.07.014 [online] Available from: http://dx.doi.org/10.1016/j.ecss.2013.07.014

Rogers KG, Overeem I. 2017. Doomed to drown? Sediment dynamics in the human-controlled floodplains of the active Bengal Delta. University Libraries Open Access Fund Supported Publications **83** : 1–15.

Romans BW, Castelltort S, Covault JA, Fildani A, Walsh JP. 2016. Environmental signal propagation in sedimentary systems across timescales. Earth-Science Reviews **153** : 7–29. DOI: 10.1016/j.earscirev.2015.07.012 [online] Available from: http://dx.doi.org/10.1016/j.earscirev.2015.07.012

Roskoden RR, Bryan KR, Schreiber I, Kopf A. 2020. Rapid transition of sediment consolidation across an expanding mangrove fringe in the Firth of Thames New Zealand. Geo-Marine Letters **40** : 295–308. DOI: 10.1007/s00367-019-00589-9

de Ruiter PJ, Mullarney JC, Bryan KR, Winter C. 2019. The links between entrance geometry, hypsometry and hydrodynamics in shallow tidally dominated basins. Earth Surface Processes and Landforms **44** : 1957–1972. DOI: 10.1002/esp.4622

Sakai T, Omori K, Oo AN, Ma SS, Zaw YN. 2021. Decadal changes in the rice-cropping system in the Ayeyarwady Delta using a large archive of satellite imagery from 1981 to 2020. Paddy and Water Environment **19** : 295–306. DOI: 10.1007/s10333-021-00857-4 [online] Available from: https://doi.org/10.1007/s10333-021-00857-4

Santen P Van, Augustinus PGEF, Janssen-stelder BM, Quartel S, Tri NH. 2007. Sedimentation in an estuarine mangrove system. Journal of Asian Earth Sciences **29** : 566–575. DOI: 10.1016/j.jseaes.2006.05.011

Schlager W. 1993. Accommodation and supply-a dual control on stratigraphic sequences. Sedimentary Geology **86** : 111–136. DOI: 10.1016/0037-0738(93)90136-S

Simon JA. 2018. Storm Surges in Tauranga Harbour, University of Waikato

Sternberg RW. 1968. Friction factors in tidal channels with differing bed roughness. Marine Geology **6** : 243–260. DOI: https://doi.org/10.1016/0025-3227(68)90033-9

Stokes DJ. 2010. The physical and ecological impacts of mangrove expansion and mangrove removal: Tauranga Harbour, New Zealand, University of Waikato

Stokes DJ, Harris RJ. 2015. Sediment properties and surface erodibility following a large-scale mangrove (Avicennia marina) removal. Continental Shelf Research **107** : 1–10. DOI: 10.1016/j.csr.2015.07.011 [online] Available from: http://dx.doi.org/10.1016/j.csr.2015.07.011

Stokes DJ, Healy TR, Cooke PJ. 2009. Surface elevation changes and sediment characteristics of intertidal surfaces undergoing mangrove expansion and mangrove removal, Waikaraka Estuary, Tauranga Harbour, New Zealand. International Journal of Ecology and Development **12** : 88–106.

Styles R, Snedden GA, Smith SJ, Bryant DB, Boyd BM, Gailani JZ, Couvillion B, Race E. 2021. Seasonal controls on sediment delivery and hydrodynamics in a vegetated tidally influenced interdistributary island. Journal of Geophysical Research: Oceans **126** : 1–16. DOI: 10.1029/2020JC016146

Sullivan JC, Torres R, Garrett A. 2019. Intertidal creeks and overmarsh circulation in a small salt marsh basin. Journal of Geophysical Research: Earth Surface **124** : 447–463. DOI: 10.1029/2018JF004861

Susilo A, Ridd P V., Thomas S. 2005. Comparison between tidally driven groundwater flow and flushing of animal burrows in tropical mangrove swamps. Wetlands Ecology and Management **13** : 377–388. DOI: 10.1007/s11273-004-0164-0

Sutherland J, Peet AH, Soulsby RL. 2004. Evaluating the performance of morphological models. Coastal Engineering **51** : 917–939. DOI: 10.1016/j.coastaleng.2004.07.015

Swales A, Bentley SJ, Lovelock CE. 2015. Mangrove-forest evolution in a sediment-rich estuarine system: Opportunists or agents of geomorphic change? Earth Surface Processes and Landforms **40** : 1672–1687. DOI: 10.1002/esp.3759

Swales A, Bentley SJ, Lovelock CE, Bell RG. 2007. Sediment processes and mangrove-habitat expansion on a rapidly-prograding muddy coast, New Zealand. Coastal Sediments ’07 : 1–14.

Swales A, Denys P, Pickett VI, Lovelock CE. 2016. Evaluating deep subsidence in a rapidly-accreting mangrove forest using GPS monitoring of surface-elevation benchmarks and sedimentary records. Marine Geology **380** : 205–218. DOI: 10.1016/j.margeo.2016.04.015 [online] Available from: http://dx.doi.org/10.1016/j.margeo.2016.04.015

Sweetman AK, Middelburg JJ, Berle AM, Bernardino AF, Schander C, Demopoulos AWJ, Smith CR. 2010. Impacts of exotic mangrove forests and mangrove deforestation on carbon remineralization and ecosystem functioning in marine sediments. Biogeosciences **7** : 2129–2145. DOI: 10.5194/bg-7-2129-2010

Syvitski JPM et al. 2009. Sinking deltas due to human activities. Nature Geoscience **2** : 681–686. DOI: 10.1038/ngeo629 [online] Available from: http://www.nature.com/doifinder/10.1038/ngeo629

Syvitski JPM, Saito Y. 2007. Morphodynamics of deltas under the influence of humans. Global and Planetary Change **57** : 261–282. DOI: 10.1016/j.gloplacha.2006.12.001

Tamura T, Saito Y, Lap Nguyen V, Oanh Ta TK, Bateman MD, Matsumoto D, Yamashita S. 2012. Origin and evolution of interdistributary delta plains; insights from Mekong River Delta. Geology **40** : 303–306. DOI: 10.1130/G32717.1

Tejedor A, Longjas A, Caldwell R, Edmonds DA, Zaliapin I, Foufoula-Georgiou E. 2016. Quantifying the signature of sediment composition on the topologic and dynamic complexity of river delta channel networks and inferences toward delta classification. Geophysical Research Letters **43** : 1–8. DOI: 10.1002/2016GL068210.Received

Tejedor A, Longjas A, Zaliapin I, Foufoula-Georgiou E. 2015a. Delta channel networks: 1. A graph-theoretic approach for studying connectivity and steady state transport on deltaic surfaces. Water Resources Research **51** : 3998–4018. DOI: 10.1111/j.1752-1688.1969.tb04897.x

Tejedor A, Longjas A, Zaliapin I, Foufoula-Georgiou E. 2015b. Delta channel networks: 2. Metrics of topologic and dynamic complexity for delta comparison, physical inference, and vulnerability assessment. Water Resources Research **51** : 4019–4045. DOI: 10.1111/j.1752-1688.1969.tb04897.x

Temmerman S, Bouma TJ, Govers G, Wang ZB, De Vries MB, Herman PMJ. 2005. Impact of vegetation on flow routing and sedimentation patterns: Three-dimensional modeling for a tidal marsh. Journal of Geophysical Research: Earth Surface **110** : 1–18. DOI: 10.1029/2005JF000301

Thant AA, Teutscherova N, Vazquez E, Kalousova M, Phyo A, Singh RK, Lojka B. 2020. On-farm rice diversity and farmers' preferences for varietal attributes in Ayeyarwady Delta, Myanmar. Journal of Crop Improvement **34** : 549–570. DOI: 10.1080/15427528.2020.1746457

Torres R, Styles R. 2007. Effects of topographic structure on salt marsh currents. Journal of Geophysical Research: Earth Surface **112** : 1–14. DOI: 10.1029/2006JF000508

Uncles RJ, Stephens JA, Smith RE. 2002. The dependence of estuarine turbidity on tidal intrusion length, tidal range and residence time. Continental Shelf Research **22** : 1835–1856. DOI: 10.1016/S0278-4343(02)00041-9

Vandenbruwaene W, Bouma TJ, Meire P, Temmerman S. 2013. Bio-geomorphic effects on tidal channel evolution: Impact of vegetation establishment and tidal prism change. Earth Surface Processes and Landforms **38** : 122–132. DOI: 10.1002/esp.3265

Vigny C, Socquet A, Rangin C, Chamot-Rooke N, Pubellier M, Bouin MN, Bertrand G, Becker M. 2003. Present-day crustal deformation around Sagaing fault, Myanmar. Journal of Geophysical Research **108** : 2533–2534. DOI: 10.1029/2002jb001999

Walsh JP, Nittrouer CA. 2009. Understanding fine-grained river-sediment dispersal on continental margins. Marine Geology **263** : 34–45. DOI: 10.1016/j.margeo.2009.03.016 [online] Available from: http://dx.doi.org/10.1016/j.margeo.2009.03.016

Webb EL, Jachowski NRA, Phelps J, Friess DA, Than MM, Ziegler AD. 2014. Deforestation in the Ayeyarwady Delta and the conservation implications of an internationally-engaged Myanmar. Global Environmental Change **24** : 321–333. DOI: 10.1016/j.gloenvcha.2013.10.007 [online] Available from: http://dx.doi.org/10.1016/j.gloenvcha.2013.10.007

Wheatcroft RA. 2000. Oceanic flood sedimentation: a new perspective. Continental Shelf Research **20** : 2059–2066. [online] Available from: http://www.sciencedirect.com/science/article/pii/S0278434300000625 (Accessed 7 November 2013)

Willemsen PWJM, Horstman EM, Borsje BW, Friess DA, Dohmen-Janssen CM. 2016. Sensitivity of the sediment trapping capacity of an estuarine mangrove forest. Geomorphology **273** : 189–201. DOI: 10.1016/j.geomorph.2016.07.038 [online] Available from: http://dx.doi.org/10.1016/j.geomorph.2016.07.038

Wilson CA, Goodbred SL. 2015. Construction and maintenance of the Ganges-Brahmaputra-Meghna Delta: Linking process, morphology, and stratigraphy. Annual Review of Marine Science **7** : 67–88. DOI: 10.1146/annurev-marine-010213-135032 [online] Available from: http://www.annualreviews.org/doi/10.1146/annurev-marine-010213-135032

Win S, Towprayoon S, Amnat C. 2019. Adaptation of mangrove trees to different salinity areas in the Ayeyarwaddy Delta Coastal Zone, Myanmar. Estuarine, Coastal and Shelf Science **228** : 1–8. DOI: 10.1016/j.ecss.2019.106389

Winterwerp JC, Erftemeijer PLA, Suryadiputra N, Van Eijk P, Zhang L. 2013. Defining eco-morphodynamic requirements for rehabilitating eroding mangrove-mud coasts. Wetlands **33** : 515–526. DOI: 10.1007/s13157-013-0409-x

Wohl EE. 2020. Rivers in the Landscape . 2nd ed. JohnWiley & Sons Ltd [online] Available from: https://lccn.loc.gov/2019032035

Wolanski E, Jones M, Bunt JS. 1980. Hydrodynamics of a tidal creek-mangrove swamp system. Aust. J. Mar. Freshwater Res. **31** : 431–450. DOI: 10.1071/MF9800431

Wolanski E, Mazda Y, King B, Gay S. 1990. Dyanmics, flushing and trapping in Hinchinbrook Channel, a giant mangrove swamp, Australia. Estuarine, Coastal and Shelf Science **31** : 555–579.

Woodroffe CD. 1992. Mangrove Sediments and Geomorphology. In Coastal and Estuarine Studies , Robertson AI and Alongi DM (eds). 7–41.

Woodroffe CD, Rogers K, McKee KL, Lovelock CE, Mendelssohn IA, Saintilan N. 2016. Mangrove sedimentation and response to relative sea-level rise. Annual Review of Marine Science **8** : 243–266. DOI: 10.1146/annurev-marine-122414-034025 [online] Available from: http://www.annualreviews.org/doi/10.1146/annurev-marine-122414-034025

Xiao Y, Wu Z, Cai H, Tang H. 2018. Suspended sediment dynamics in a well-mixed estuary: The role of high suspended sediment concentration (SSC) from the adjacent sea area. Estuarine, Coastal and Shelf Science **209** : 191–204. DOI: 10.1016/j.ecss.2018.05.018 [online] Available from: https://doi.org/10.1016/j.ecss.2018.05.018

Young BM, Harvey LE. 1996. A Spatial Analysis of the Relationship Between Mangrove (Avicennia marina var. australasica) Physiognomy and Sediment Accretion in the Hauraki Plains , New Zealand. Estuarine, Coastal and Shelf Science **42** : 231–246.

Zheng H, Cheng T, Zhou M, Li D, Yao X, Tian Y, Cao W, Zhu Y. 2019. Improved estimation of rice aboveground biomass combining textural and spectral analysis of UAV imagery. Precision Agriculture **20** : 611–629. DOI: 10.1007/s11119-018-9600-7

APPENDIX A: CHAPTER 2 SUPPORTING INFORMATION

Previously published at: https://doi.org/10.1029/2020JF005882

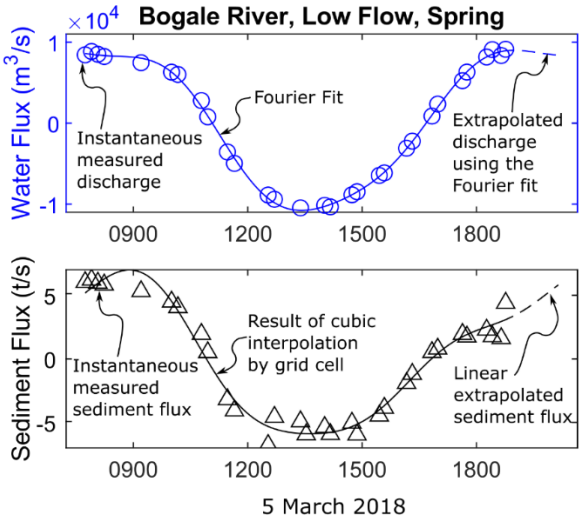

Figure A.S1. Annotated example calculation of discharge. For the incomplete low-flow surveys, water discharge was calculated using a Fourier curve fit to the data points. Error was estimated by calculating the RMSE of the fit. Sediment flux was not well represented by a Fourier series, missing data were filled by cubic interpolation of velocity and SSC for each grid cell.

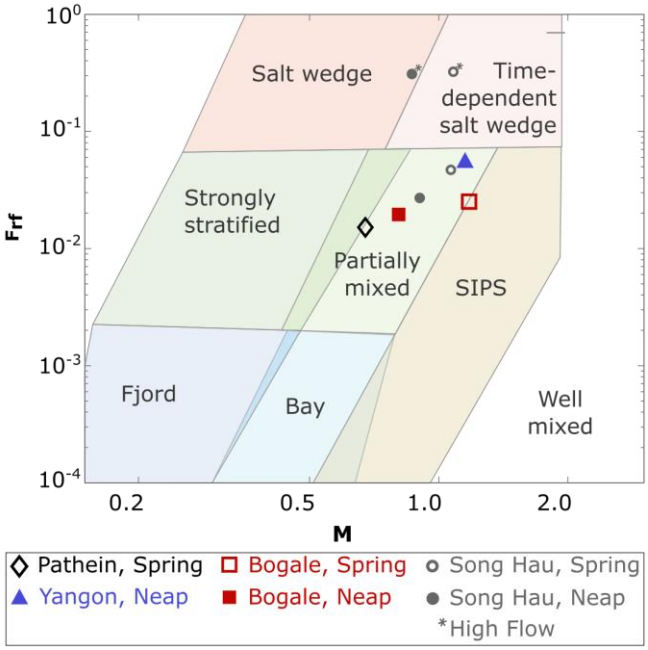

Figure A.S2. Estuarine parameter space adapted from Geyer and MacCready (2014) with the low-flow Ayeyarwady distributaries. Spring tides are shown with hollow symbols and neap tides with filled symbols; the Yangon is in blue triangles, the Bogale is in red squares, and the Pathein is in black diamonds. The Dinh An channel of the Song Hau distributary of the Mekong River is depicted with gray circles, with asterisks marking high-flow data (from McLachlan et al., 2017).

Table A.S1. Box-model calculations of sediment retained in the upper delta during the high-flow season. Sediment retention was estimated based on the input to each distributary at its bifurcation and the residual sediment export at the sampling sites (Figure 2.1). During high flow we can assume that the sediment partitioning between distributaries is roughly equal to the water partitioning because SSC was consistent across distributaries (Table 2.1). The fraction of water partitioned to each distributary was multiplied by the minimum, best, and maximum estimated sediment discharge values at Pyay (Baronas et al., 2020) to estimate the sediment partitioned to each distributary at its bifurcation. The percent retention was then estimated based on the ratio of this sediment flux at the bifurcation to the sediment flux at the transect locations.

	Avg September Water Discharge, m3/s	Fraction of total water discharge in each distributary	September Sediment Discharge, Mt/d			Fraction of sediment partitioned to distributary at bifurcation based on water			Fraction of sediment retained in the upper delta		
			Min	Best	Max	Min	Best	Max	Min	Best	Max
Pyay**	25880		1.82	2.33	2.99						
Yangon	7830	0.30	0.29	0.29	0.29	0.55	0.70	0.90	0.52	0.40	0.32
Pathein	6400	0.25	0.13	0.13	0.13	0.45	0.58	0.74	0.29	0.22	0.18
Bogale (Spring)	1200	0.05	0.06	0.06	0.06	0.08	0.11	0.14	0.74	0.58	0.45
Bogale (Neap)	1960	0.08	0.04	0.04	0.04	0.14	0.18	0.23	0.28	0.22	0.17

**Values from Baronas, et al. (2020)

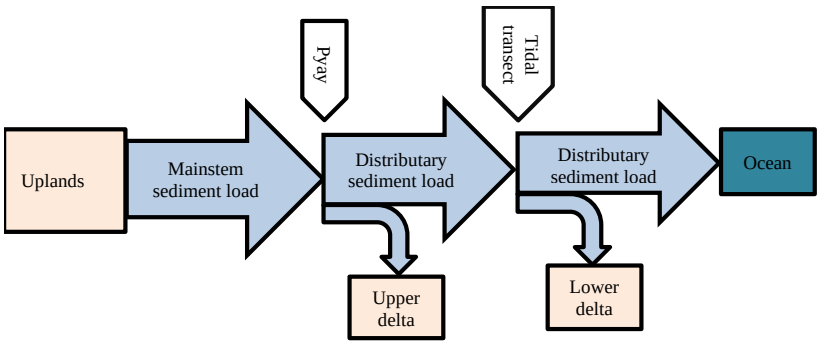

Figure A.S3. Schematic of the box-model of sediment retention in the upper delta during the high flow season. Sediment retention was estimated based on the sediment input to each distributary, measured at Pyay, and the residual sediment export, measured at the sampling sites.

APPENDIX B: CHAPTER 3 SUPPORTING INFORMATION

Table B.S1. The horizontal and vertical tidal asymmetry were calculated following the methods of Nidzieko and Ralston (2012) and Guo et al. (2019). All three metrics can be calculated using the normalized sample skewness of the property, $\gamma(n)$:

$$\gamma(n) = \frac{\mu_3}{{\mu_2}^{3/2}} = \frac{1}{N-1}\sum_{i=1}^{N}(n_i)^3 \Big/ \left(\frac{1}{N-1}\sum_{i=1}^{N}(n_i)^2\right)^{3/2}$$

where μ_3 is the third moment about zero, μ_2 is the second moment about zero, and N is the total number of observations. The duration asymmetry (γ_d) is calculated from the sign of the water level change rate ($n=dh/dt$ in Eqn. 5), the velocity skew (γ_u) is calculated from the depth-averaged velocity ($n=u$ in Eqn. 5), and the slack-water duration asymmetry is calculated from the water acceleration ($n=du/dt$ in Eqn. 5). For the HC and LC channels the average duration asymmetry, velocity skew, and slack-water asymmetry were calculated from the Aquadopp data. This average may not represent the full, spring-neap range of values.

Deployment		Average duration asymmetry	Average velocity asymmetry	Average slack-water asymmetry
HC	Sep 2017	0.38	-0.55	-0.04
	Mar 2018	0.34	-0.36	0.37
	Sep 2019	0.56	-0.71	0.16
LC	Sep 2017	0.25	-0.39	-
	Mar 2018	0.31	-0.07	-
	Sep 2019	0.33	0.37	-

Table B.S2. Predicted and measured channel-mouth widening for tidal-prism accommodation, based on calculations and reported delta constants in Nienhuis, et al. (2018). The channel slope was assumed to be 0.00005 and the proportionality coefficient, k, was 1.1e-4 m^{-1}.

Distributary	Measured width upstream (km)	Channel depth (m)	Tidal amp. (m)	Measured mouth width (km)	Predicted width at mouth (km),
Pathein	1	15	2.5	6	6.5
Bogale	1	15	3	8**	8
Yangon	0.7	20	5.5	8	9

**This width includes Meinmahla Island.

APPENDIX C: CHAPTER 4 SUPPORTING INFORMATION

Text C.S1. ^{137}Cs isotope was primarily released during atomic testing, starting in 1953. The accumulation rate can be calculated as (Lynch et al., 1989; Nittrouer et al., 1984):

$$S = {(z_p - z_{sml})}/{(t_0 - t_i)}$$

where z_p is the maximum depth of observed ^{137}Cs, z_{sml} is the base of the surface mixed layer, t_0 is the year of collection (2019), and t_i is the date of introduction (1953). For the agricultural field, the surface mixed layer was taken to be 15 cm, the depth of plowing (Goodbred and Kuehl, 1998; Hayashi et al., 2006). However, ^{137}Cs can also diffuse downcore in intertidal environments (Alexander et al., 1991), artificially increasing the maximum depth and apparent accumulation rate. The rate calculated from ^{137}Cs is used cautiously.

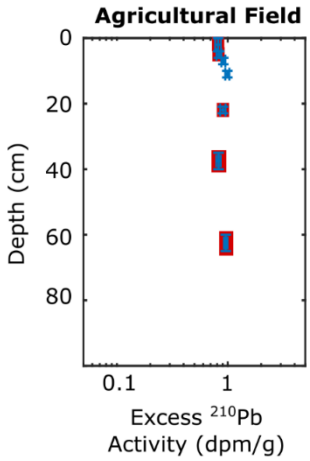

Figure C.S1. Profile of excess ^{210}Pb and ^{137}Cs from a core collected in the agricultural field. Depths where ^{137}Cs was present are highlighted in red. The activity of ^{137}Cs was consistently close to the threshold of detection.

APPENDIX D: CHAPTER 5 SUPPORTING INFORMATION

Previously published at: https://doi.org/10.1002/esp.5317

Table D.S1. Mangrove characteristics used in the vegetation model for the Delft3D models. Characteristics are based on vegetation surveys conducted in Waikaraka Estuary in June 2019 (Stokes et al., in prep).

Vegetation Type	Height (m)	Stem Diameter (m)	Stems per plant	Plants per m^2	C_d coefficient
Tree trunk	1.1	0.033	1	1.5	1
Pneumatophore	0.14	0.01	1	18	1
Tree stump	0.1	0.033	1	1.5	1

Table D.S2. The Brier Skill Score and model performance rating from Sutherland et al., (2004). The Brier Skill Score is calculated from the mean-squared error of the model versus the in-situ data:

$$BSS = 1 - \frac{\langle (Y - X)^2 \rangle}{\langle (X - \langle X \rangle)^2 \rangle}$$

where Y is the model data (water level, velocity, or bed shear stress), X is the in-situ observational data, and <> denotes averaging (Sutherland et al., 2004). With this metric, 1 is a perfect score and any score >0.5 is considered excellent. The bad performance of the bed shear stress at Station 4 is likely due to the overall low shear stresses. The same relative error is large compared to the absolute magnitude.

Station	Depth	Velocity	Bed shear stress
1	**0.98**	**0.62**	**0.76**
2	**0.95**	**0.66**	**0.64**
3	**0.95**	**0.23**	**0.37**
4	**0.82**	**0.33**	**-2.98**

>0.5	Excellent
0.2-0.5	Good
0.1-0.2	Fair
0-0.1	Poor
<0	Bad

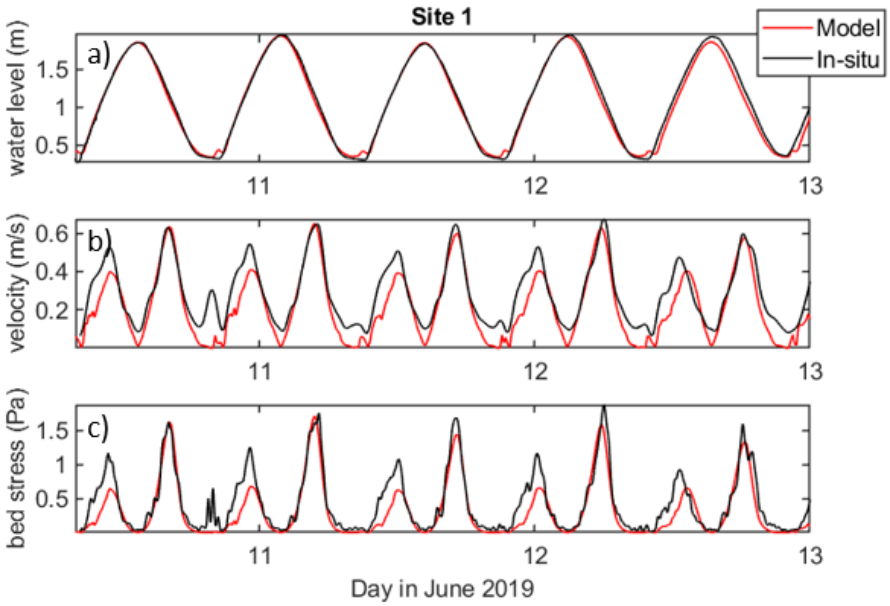

Figure D.S1. Example from Station 1 of model fit to in-situ observation of a) water level, b) velocity, and c) bed shear stress.

Text D.S1. The Manning roughness was adjusted to calibrate the velocity in the model. Typical roughness values for a shallow, unvegetated sandy/muddy creek and flat are 0.02–0.04, and the rigid vegetation model adds additional roughness to these values (Deltares, 2018). The best model performance was obtained by using a roughness of 0.02 in the channel thalweg and 0.04 everywhere else. This relatively high roughness is consistent with the seagrass meadows, shell hash, and burrows observed on the flats. The impact of using a non-uniform roughness was tested by also running the model with a uniform Manning roughness of 0.03. The model performance decreased slightly (Figure D.S2); however, the velocity patterns, tidal asymmetry and along-thalweg shear stress did not change significantly, and the results of the study did not change.

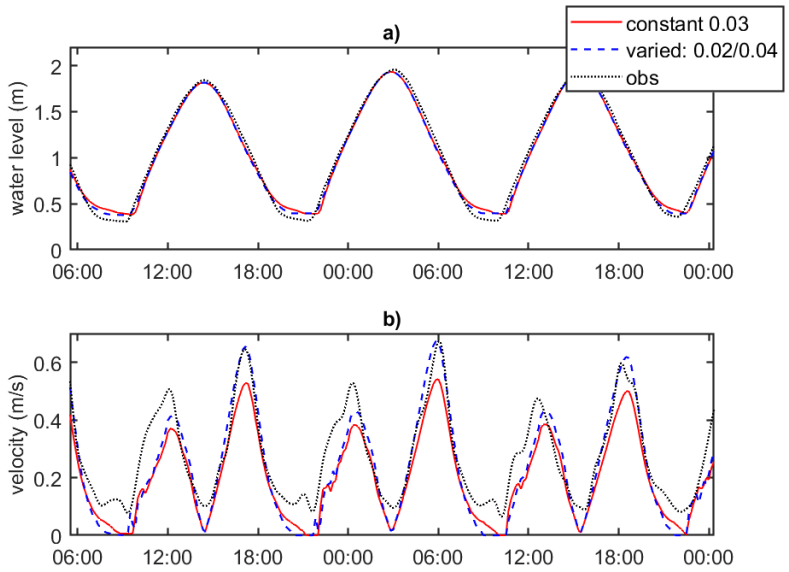

Figure D.S2. Example from Station 1 of model fit with constant Manning roughness of 0.03 and variable Manning roughness to in-situ observation of a) water level and b) velocity.

Text D.S2. The 1940 model bathymetry was artificially recreated from the 2019 bathymetry (Figure D.S3) and published rates of relative sea level rise (rSLR). The estimated rSLR was 1.7 mm/y from 1940–1974 and 2.3 mm/y from 1974–2019 (Simon, 2018; Swales et al., 2016), so the sea level was a total of ~26 cm lower in 1940. The accumulation rate on the flats was ~10 mm/y from 1940–1950 and 2.3 mm/y from 1950–2019 (Stokes, 2010), so the flats were ~16 cm lower. The bathymetry was made by first adding 26 cm to all depths to account for rSLR. Then the flats were lowered by 16 cm. The channel edges were smoothed to remove any sharp breaks in bathymetry. Sediment compaction was not directly quantified, however, adjusting the accumulation rate by +/- 0.1 mm/y did not significantly alter the results.

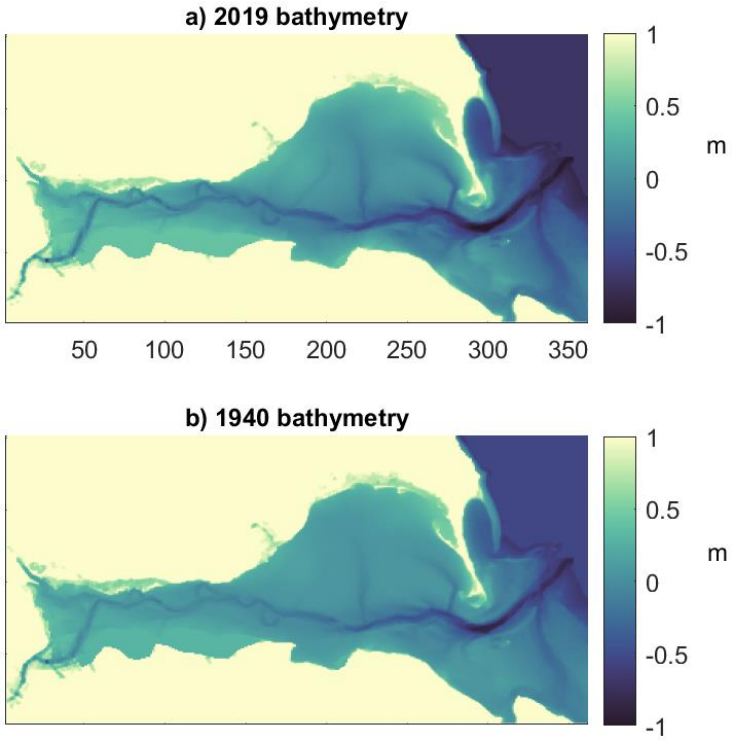

Figure D.S3. Maps of the model bathymetry for a) 2019 and b) 1940.

VITA

Hannah got her Bachelor of Arts in Earth and Oceanographic Science from Bowdoin College in 2013. Following graduation, she interned at the Maine Geological Survey and then worked as an oceanographic field engineer at the UW Applied Physics Lab. She returned to graduate school in 2016 to develop new skills in coastal sediment dynamics. Next, she plans to continue working in coastal geomorphology as a faculty research associate at Oregon State University.